

University of Windsor

## Scholarship at UWindor

---

Electronic Theses and Dissertations

Theses, Dissertations, and Major Papers

---

Fall 2021

# Wake Characteristics of Wall-Mounted Finite Solid and Foam-Covered Cylinders

Subhadip Das  
*University of Windsor*

Follow this and additional works at: <https://scholar.uwindsor.ca/etd>



Part of the [Civil Engineering Commons](#), and the [Hydraulic Engineering Commons](#)

---

### Recommended Citation

Das, Subhadip, "Wake Characteristics of Wall-Mounted Finite Solid and Foam-Covered Cylinders" (2021). *Electronic Theses and Dissertations*. 8639.  
<https://scholar.uwindsor.ca/etd/8639>

This online database contains the full-text of PhD dissertations and Masters' theses of University of Windsor students from 1954 forward. These documents are made available for personal study and research purposes only, in accordance with the Canadian Copyright Act and the Creative Commons license—CC BY-NC-ND (Attribution, Non-Commercial, No Derivative Works). Under this license, works must always be attributed to the copyright holder (original author), cannot be used for any commercial purposes, and may not be altered. Any other use would require the permission of the copyright holder. Students may inquire about withdrawing their dissertation and/or thesis from this database. For additional inquiries, please contact the repository administrator via email ([scholarship@uwindsor.ca](mailto:scholarship@uwindsor.ca)) or by telephone at 519-253-3000ext. 3208.

**Wake characteristics of wall-mounted finite solid and foam-covered cylinders**

By

**Subhadip Das**

A Dissertation  
Submitted to the Faculty of Graduate Studies  
through the Department of Civil and Environmental Engineering  
in Partial Fulfillment of the Requirements for  
the Degree of Doctor of Philosophy  
at the University of Windsor

Windsor, Ontario, Canada

2021

© 2021 Subhadip Das

# Wake characteristics of wall-mounted finite solid and foam-covered cylinders

By

**Subhadip Das**

APPROVED BY:

---

M. H. Garcia, External Examiner  
University of Illinois at Urbana-Champaign

---

V. Roussinova  
Department of Mechanical, Automotive and Materials Engineering

---

T. Bolisetti  
Department of Civil and Environmental Engineering

---

R. Carriveau  
Department of Civil and Environmental Engineering

---

R. Balachandar, Co-Advisor  
Department of Civil and Environmental Engineering

---

R. M. Barron, Co-Advisor  
Department of Mechanical, Automotive and Materials Engineering

June 15, 2021

## DECLARATION OF CO-AUTHORSHIP / PREVIOUS PUBLICATION

### I. Co-Authorship

I hereby declare that this thesis incorporates material that is result of joint research undertaken in collaboration with Dr. Ram Balachandar and Dr. Ronald M. Barron. The collaboration is covered in Chapters 2, 3 and 4 which have the following other co-authors: Dr. V. Roussinova, Dr. S. Abishek. In all cases the key ideas, primary contributions, experimental and computational designs, data analysis, interpretation, and writing were performed by myself. The contribution of co-authors in the associated journal and conference publications were primarily through the provision of guidance, discussions on technical issues and editing of the manuscripts.

I am aware of the University of Windsor Senate Policy on Authorship and I certify that I have properly acknowledged the contribution of other researchers to my thesis, and have obtained written permission from each of the co-author(s) to include the above material(s) in my thesis.

I certify that, with the above qualification, this thesis, and the research to which it refers, is the product of my own work.

### II. Previous Publications

This thesis includes original papers that have been previously published/submitted to journals for publication, as follows:

Thesis Chapter	Publication title/full citation	Publication status*
<i>Chapter [2]</i>	<b>Das, S.</b> , Balachandar, R. & Barron, R. Analysis of fully developed state in open channel flow using uniform momentum zones. <i>Journal of Fluid Mechanics</i> .	<i>Under review</i>
<i>Chapter [2]</i>	<b>Das, S.</b> , Balachandar, R., Barron, R. & Roussinova, V. (2020). An assessment of momentum zones in fully developed open channel flow. <i>FEDSM 2020, Virtual conference</i> .	<i>Published</i>
<i>Chapter [3]</i>	<b>Das, S.</b> , Balachandar, R. & Barron, R. Effect of free surface perturbation on the characteristics of fully developed smooth open channel flow. <i>Journal of Hydraulic Research</i> .	<i>Under review</i>

<i>Chapter [3]</i>	<b>Das, S.</b> , Balachandar, R., Barron, R. & Roussinova, V. (2020). Effect of free surface perturbation on mean and turbulence characteristics in a smooth open channel flow. <i>Riverflow 2020, Virtual conference.</i>	<i>Published</i>
<i>Chapter [4]</i>	<b>Das, S.</b> , Abishek, S., Balachandar, R. & Barron, R. Quantification of the wake of a wall-mounted foam-covered circular cylinder.	<i>To be submitted</i>

I certify that I have obtained a written permission from the copyright owner(s) to include the above published material(s) in my thesis. I certify that the above material describes work completed during my registration as a graduate student at the University of Windsor.

### III. General

I declare that, to the best of my knowledge, my thesis does not infringe upon anyone's copyright nor violate any proprietary rights and that any ideas, techniques, quotations, or any other material from the work of other people included in my thesis, published or otherwise, are fully acknowledged in accordance with the standard referencing practices. Furthermore, to the extent that I have included copyrighted material that surpasses the bounds of fair dealing within the meaning of the Canada Copyright Act, I certify that I have obtained a written permission from the copyright owner(s) to include such material(s) in my thesis.

I declare that this is a true copy of my thesis, including any final revisions, as approved by my thesis committee and the Graduate Studies office, and that this thesis has not been submitted for a higher degree to any other University or Institution.

## ABSTRACT

The wake characteristics of a wall-mounted finite foam-covered cylinder are explored by comparing the flow properties with the wake of a solid cylinder. The velocity data are acquired experimentally using planar particle image velocimetry (PIV) and numerically by large eddy simulation at Reynolds number of  $3.5 \times 10^4$  based on the flow depth and  $1.3 \times 10^4$  based on the cylinder diameter. The wake characteristics may vary significantly if the approach flow properties change and also depend on the relative height of the boundary layer thickness with respect to the cylinder height. Therefore, it is a necessity to achieve a fully developed approach flow to maintain the consistency and universality of the dataset. The fully developed flow is achieved numerically by recycling of flow variables from outlet to inlet, but it is not straightforward to achieve the fully developed flow experimentally. Therefore, experimental studies on the effects of the tripping intensity and the free surface perturbations are carried out for proper conditioning of the approach flow and to achieve a fully developed state in the open channel flume.

Two flow depths at a similar Reynolds number are used for the study of tripping and the intensity of tripping is gradually increased until the flow reaches the fully developed state. The boundary layer thickness is determined based on the wall-normal distribution of Reynolds stresses and higher-order moments and this is found to be more consistent than the classical definition which suggests a wall-normal position of 99% of maximum velocity. The fully developed flow is ensured by the self-similarity and comparing the experimental data with the literature. The flow properties of the fully developed state are characterized by using uniform momentum zone analysis. Compared to the momentum zones of developing flow, the fully developed flow shows a vertical variability in the quadrant events and higher shear contribution from the sweep events in the outer boundary layer which is caused by the existence of the free surface.

In the study of free surface perturbation, the effects of three different floaters are observed at a far downstream measuring station and compared with the fully developed flow. A dip in the mean velocity is noticed adjacent to the free surface and it gets larger with an increase in perturbation. It is also seen that the Reynolds shear stress becomes negative near the free surface and the dominant quadrant events shift from ejections and sweeps to inward and outward interactions due to the inverted shear layer developed from the floaters. The extent of turbulence penetration towards the bed is deeper with the increment in the level of perturbation. These floater boards are commonly used in open channel flow experiments to minimize the free surface fluctuations. However, they are found to have an unintended influence on the flow characteristics and therefore are not used in the study of the wake.

The wakes of the solid and foam-covered cylinders are developed computationally and experimentally under a fully developed approach flow. The PIV data are used to validate the computational model which is further used to reveal three-dimensionality in the flow characteristics. The iso-surface of  $\lambda_2$  is used to depict the instantaneous vortical structures such as horseshoe vortex, arch vortex, tip vortex etc. These vortical structures are prominent for the solid cylinder but broken. In case of foam-covered cylinders, the formation of the flow structure is highly influenced by the inner solid cylinder, top plate and the foam covering. Especially, the foam structure interrupts the formation of any large flow structures and suppresses the oscillating behaviour of the wake. Consequently, Reynolds stress generation in the near-wake region of the foam-covered cylinder is found to be much less and no dominant frequency is identified in the FFT

analysis. Finally, spectral proper orthogonal decomposition (SPOD) modes are used to visualize the coherent structures around the body. In case of a solid cylinder, the tip vortices move downward and reattaches with the bottom wall within a short distance. However, this downstream reattachment length for the foam-covered cylinder is significantly higher since the flow through the porous foam structures lifts up the tip vortices. A difference in the reattachment pattern can also be seen on the top face of the cylinder, which occurs in a straight line for the solid cylinder but in a curved line for the foam-covered cylinder. The SPOD modes on the mid-horizontal plane depicts an asymmetric generation of side vortices due to the asymmetry in the foam structure.

## DEDICATION

To my beloved brother in heaven.



## ACKNOWLEDGEMENTS

I would like to express my profound gratitude to my co-supervisors Dr. Ram Balachandar and Dr. Ronald Barron for their exemplary guidance, constant support and encouragement. They have given me freedom to shape my research work and helped me grow academically as well as personally.

I want to extend my gratitude to the members of my doctoral committee, Dr. Vesselina Roussinova, Dr. Tirupati Bolisetti, Dr. Rupp Carriveau for providing insights and new perspective to my research. I am also thankful to Dr. Marcelo H. Garcia for taking time to review my thesis and for serving as my external examiner.

I want to thank Matthew St. Luis for continuous help and support during the experiments.

I would also like to acknowledge the mental support and technical input of each of the members of my research group, especially Nimesh Virani, Sachin Sharma, Damanpreet Singh, Dr. Abishek Sridhar, Dr. Vimaldoss Jesudhas, Dr. Kohei Fukuda, Dr. Priscilla Williams, Dr. Maziar Mosavati, Dr. E. E. Ekow, Dr. Sourayon Chanda.

I am also very much grateful to Dr. Shivam Tripathi, Dr. Rajesh Srivastava and Dr. Arun K. Saha who inspired me in developing interest in research work.

I also appreciate the help and support of my friends Kriti Chakraborty, Monalisa Ghosh, Rinky Bhadra, Tumpa Shaw, Srinjoy Roy, Panchajanya Sanyal, Soham Chatterjee, Sayantan Chakraborty, Shubhabrata Sarkar, Suman Roy, Surya Gupta, Jayasree Biswas, Suman Mullick, Debanjan Ghosh, Soumendu Bagchi, Avijit Karmakar, Harshit Singh, Vihan Patel, Kalapi Kapadia, Saharsh Bawankar, Ishan Patel, Sumit Patel, Vivek Joshi, Sai Krishna.

Finally, I want to thank my mother Sukla Das and my family members for patiently waiting for me and helping me survive through thick and thin.

In the end, I want to thank my father Late Tapan Das and my brother Late Mainak Das for always being there for me since childhood and making me myself.

## TABLE OF CONTENTS

DECLARATION OF CO-AUTHORSHIP / PREVIOUS PUBLICATION .....	iii
ABSTRACT .....	v
DEDICATION .....	vii
ACKNOWLEDGEMENTS .....	viii
LIST OF TABLES .....	xii
LIST OF FIGURES .....	xiii
LIST OF ABBREVIATIONS/SYMBOLS .....	xviii
CHAPTER 1 INTRODUCTION .....	1
1.1. Background .....	1
1.2. Motivations and objectives .....	2
1.3. Thesis organization .....	2
References .....	3
CHAPTER 2 ANALYSIS OF FULLY DEVELOPED STATE IN OPEN CHANNEL FLOW USING UNIFORM MOMENTUM ZONES .....	4
2.1. Introduction .....	4
2.2. Experiment setup and test conditions .....	7
2.3. Shear velocity .....	10
2.4. Mean velocity .....	12
2.5. Reynolds stresses and higher-order moments .....	15
2.6. Uniform momentum zones .....	20
2.6.1. <i>Detection of turbulent/non-turbulent interface</i> .....	21
2.6.2. <i>Detection of uniform momentum zones</i> .....	23
2.6.3. <i>Characterization of fully developed flow</i> .....	25
2.6.4. <i>Quadrant events</i> .....	27
2.6.5. <i>Large-scale fluid motions</i> .....	27
2.7. Summary and conclusions .....	33

References.....	34
CHAPTER 3 EFFECT OF FREE SURFACE PERTURBATION ON THE CHARACTERISTICS OF FULLY DEVELOPED SMOOTH OPEN CHANNEL FLOW .....	39
3.1. Introduction.....	39
3.2. Experimental setup.....	41
3.3. Results and discussions.....	43
3.3.1. Mean velocity distribution .....	43
3.3.2. Reynolds stresses .....	45
3.3.3. Higher-order moments .....	46
3.3.4. Quadrant analysis.....	49
3.4. Summary and conclusions .....	54
References.....	54
CHAPTER 4 QUANTIFICATION OF THE WAKE OF A WALL-MOUNTED FOAM- COVERED CIRCULAR CYLINDER .....	57
4.1. Introduction.....	57
4.1.1. Motivation .....	57
4.1.2. Literature review.....	58
4.2. Methodology .....	60
4.2.1. Geometry of the solid and foam-covered cylinders.....	60
4.2.2. Experimental methodology .....	61
4.2.3. Computational methodology .....	63
4.3. Validation.....	66
4.3.1. Validation of the approach flow.....	66
4.3.2. Flow around cylinders .....	67
4.4. Flow structures around the cylinder.....	72
4.5. Wake characteristics .....	73
4.5.1. Vertical planes .....	74
4.5.2. Horizontal planes.....	76
4.5.3. Cross-stream planes.....	77
4.5.4. Velocity deficit.....	78
4.6. Frequency analysis .....	80

4.7. Spectral proper orthogonal decomposition .....	82
4.7.1. <i>SPOD on vertical plane</i> .....	83
4.7.2. <i>SPOD on horizontal plane</i> .....	84
4.8. Summary and conclusion .....	86
References.....	87
 CHAPTER 5 CONCLUSIONS AND RECOMMENDATIONS .....	 91
APPENDICES .....	94
Appendix A. Dependence of UMZ analysis on threshold kinetic energy deficit and streamwise extent of FOV .....	94
Appendix B. Dependence of UMZ analysis on the bin size .....	94
 VITA AUCTORIS .....	 94

## LIST OF TABLES

Table 1.1. Thesis organization .....	3
Table 2.1. Details of the test conditions, trip characteristics and flow parameters .....	9
Table 2.2. Shear velocities for different test cases .....	12
Table 2.3. Boundary layer thickness .....	14
Table 2.4. The details of the previous studies used to check the self-similarity of the fully developed state (OCF: Open channel flow, CF: Channel flow, TBL: Turbulent boundary layer) .....	19
Table 3.1. Test conditions .....	41
Table 3.2. Shear velocity ( $U_\tau$ ) and wake strength parameter ( $\Pi$ ) for all test cases .....	44

## LIST OF FIGURES

Figure 2.1. Schematic of the recirculating flume and test set up .....	8
Figure 2.2. Deviation in the mean and turbulence quantities with increase in sample size .....	10
Figure 2.3. Streamwise variation of (a) the ratio of wall-shear velocity and maximum velocity ( $U_\tau/U_\infty$ ) and (b) shape factor for the fully developed states .....	12
Figure 2.4. Mean streamwise velocity profiles at $H = 0.135$ m normalized by inner scaling, compared with the log-law profile. Velocity profiles for tests T1, T1&T2, and T1&T3 are shifted vertically by a constant value to enhance visualization .....	13
Figure 2.5. Collapse onto Krogstad's velocity defect law (VDL) for different trip conditions at $H = 0.135$ m with the normalization of y coordinate by (a) $\delta$ and (b) $\delta'$ . The profiles of T1, T1&T2, and T1&T3 are shifted by a constant value .....	15
Figure 2.6. Distribution of normalized streamwise, bed-normal and shear stresses: (a,b,c) $H = 0.135$ m and (d, e, f) $H = 0.170$ m .....	17
Figure 2.7. Distribution of normalized third-order and fourth-order moments: (a,b,c,d) $H = 0.135$ m and (e,f,g,h) $H = 0.170$ m .....	18
Figure 2.8. Comparison of fully developed profiles with previous studies: (a) Mean streamwise velocity, (b,c,d) Reynolds stresses, (e,f,g,h) Third and fourth-order moments .....	20
Figure 2.9. Normalized mean TNTI location ( $Y_{TNTI}$ ) for all test cases at $H = 0.170$ m and the distribution of $Y_{TNTI} + 3\sigma$ for the fully developed state T1&T3 (inset) corresponding to the value of $K_{th}$ between 0.3 to 5.0 .....	22
Figure 2.10. (a) PDF of streamwise velocities below TNTI for a single instance. The inverted triangles '▼' indicates the modal velocities and the dashed lines differentiate the UMZs. The continuous blue line represents the curve fitted over the probability data in order to find the modal velocities. (b) corresponding contour plot of the UMZs. The average bed-normal position (i.e., the adjacent upper contour level) and the thickness of momentum zones is presented by $Y_{UMZ} _{R_i}$ and $t_{UMZ} _{R_i}$ where $i$ is the rank of the corresponding momentum zone .....	23
Figure 2.11. (a) PDF of $N_{UMZ}$ corresponding to bin size $0.5U_\tau$ ; (b) Bed-normal distribution of $Y_{UMZ} _{i,j}$ and $Y_{MV} _{i,j}$ (shown by '●' and '▲', respectively) for the fully developed flow (test case T1&T3 at $H = 0.170$ m). The subscripts $i$ and $j$ indicate the value of $N_{UMZ}$ and rank, respectively .....	25
Figure 2.12. Conditional averaging of the data corresponding to a specific value of $N_{UMZ}$ based on their rank ( $R_i$ ) of (a) modal velocities ( $U_{MV} _{R_i}$ ), (b) bed-normal position of the mean contour level of UMZs ( $Y_{UMZ} _{R_i}$ ) and (c) the corresponding thickness of UMZs ( $t_{UMZ} _{R_i}$ ). Same markers are used for the same rank and same colors for a given $N_{UMZ}$ . The markers represent the centered values and the bars show the distribution around it based on the magnitude of 25 <sup>th</sup> and 75 <sup>th</sup> percentile. The	

distributions for  $N_{UMZ} = 3$  are presented for (d)  $U_{MV}|_{R_1}$ , (e)  $Y_{UMZ}|_{R_1}$  and (f)  $t_{UMZ}|_{R_1}$ . The magnitudes of 25<sup>th</sup> and 75<sup>th</sup> percentiles are shown by the dashed lines ..... 26

Figure 2.13. (a) PDF of  $N_{UMZ}$  corresponding to bin size  $0.5U_\tau$  for the developing flow (T0 at  $H = 0.170$  m) and the fully developed flow (T1&T3 at  $H = 0.170$  m). Conditional averaging of ratio of shear stress contribution from Q2 and Q4 events based on the value of  $N_{UMZ}$  for (b) the fully developed flow (T1&T3 at  $H = 0.170$  m) and (c) the developing flow (T0 at  $H = 0.170$  m)..... 28

Figure 2.14. Conditional averaging of normalized streamwise and wall-normal velocity deficit based on the value of  $N_{UMZ}$  for (a,b) the fully developed flow (T1&T3 at  $H = 0.170$  m) and (c,d) the developing (T0 at  $H = 0.170$  m)..... 29

Figure 2.15. Bed-normal distribution of normalized total shear stress contribution by large-scale Q2 and Q4 events ( $-\overline{u'v'}_{Q2+Q4}|_{E_1+E_2}$ ) in the logarithmic layer for the fully developed flow (T1&T3 at  $H = 0.170$  m) and the developing flow (T0 at  $H = 0.170$  m). ..... 30

Figure 2.16. Conditional averaging of shear stress contribution based on the large-scale Q2 ( $E_1$ ) and Q4 ( $E_2$ ) events in the logarithmic layer for (a,b) the fully developed flow (T1&T3 at  $H = 0.170$  m) and (c,d) the developing flow (T0 at  $H = 0.170$  m). The subscript  $Q_i$  indicates the contribution in ejection and sweep events for  $i = 2$  and  $4$ , respectively ..... 32

Figure 2.17. (a) Ratio of total shear stress contribution by T1&T3 and T0 (to Q2 or Q4 events). (b) Ratio of total shear stress contribution to Q2 and Q4 events (for T0 and T1&T3). The instances which belong to either  $E_1$  or  $E_2$  are considered here to estimate shear stress contributions ..... 33

Figure 3.1. Distributions for test case F1M at three different  $x/\mathcal{L}$  locations: (a) streamwise velocity, (b) streamwise Reynolds normal stress, (c) Reynolds shear stress, (d) third-order moments of streamwise velocity fluctuations (in the form of skewness). The dashed-lines represent the double-averaged (DA) profiles ..... 43

Figure 3.2. Normalized streamwise velocity profiles: (a) outer scaling, (b) inner scaling; (F0: no float, F1: shorter float, F2: longer float, F1M: shorter float with mesh)..... 45

Figure 3.3. Distribution of Reynolds stresses, normalized by local mean velocity, (a) streamwise component, (b) bed-normal component, (c) shear stress component ..... 46

Figure 3.4. Third-order and fourth-order moments of velocity fluctuations in the form of (a,b) skewness factor, (c,d) flatness factor ..... 48

Figure 3.5. Probability density function of streamwise velocity fluctuations at four depths:  $y/H = 0.95, 0.8, 0.6, 0.4$  in test cases (a) F0, (b) F1, (c) F2, (d) F1M..... 48

Figure 3.6 Joint probability density function,  $P(u',v')$  in test cases F0 (first column), F1 (second column), F2 (third column) and F1M (fourth column) at  $y/H =$  (a) 0.95, (b) 0.8, (c) 0.6, (d) 0.4.  $P(u',v')$  is normalized in such a way that the maximum probability density is unity ..... 50

Figure 3.7. Probability of occurrence of the quadrant events in test (a) F0, (b) F1, (c) F2, (d) F1M. ( $\circ$  Q1,  $\Delta$  Q2,  $\diamond$  Q3,  $\square$  Q4) ..... 51

Figure 3.8. Reynolds shear stress contribution from (a) Q1, (b) Q2, (c) Q3, (d) Q4 at each test condition .....	52
Figure 3.9. Ratio of shear stress contribution from (a) Q2 and Q4 ( $R_{Q2/Q4}$ ), (b) Q2+Q4 and Q1+Q3 ( $R_{Q2+Q4/Q1+Q3}$ ). (c) Shear stress component of Reynolds stress anisotropy tensor ( $-b_{12}$ ).....	53
Figure 4.1. Schematic diagram of important flow features of a flow around a surface mounted low aspect ratio circular cylinder. (Adapted from Pattenden <i>et al.</i> 2005, Krajnović 2011 and Sumner 2013) .....	59
Figure 4.2. Geometry of the foam-covered cylinder: (a) front view, (b) cross-sectional view with a 90° cut-out. $d$ and $d_i$ : outer and inner diameter of the cylinder, 0.05m and 0.022m, respectively, $d_f$ : thickness of a single strut of the foam structure, 3 mm, $b$ : thickness of the base and the top plate, 5 mm, $h$ : height of the cylinder, 0.0436 m. (c) polydispersity index and the distribution in the number of pores per cell in the foam. [1]: Montminy <i>et al.</i> (2004), [2]: White and Vlack (1970), [3]: Jaganathan <i>et al.</i> (2008) .....	61
Figure 4.3. (a) Experimental setup. CF: solid cylinder or foam-covered cylinder, CP: central pump, FS: flow straighteners, FDF: fully developed flow, PIV: particle image velocimeter, ST-1,2: upstream and downstream settling tanks, TG: tail gate, TR: inflow tripping. (b) top view of the cylinder showing the measurement planes. The dashed line represents the inner cylinder .....	62
Figure 4.4. (a) Top and front view of the simulation domain, (b) mesh around the foam structures. ....	64
Figure 4.5. (a) The ratio of cell size and Taylor micro-scale ( $\Delta/\lambda$ ) at three different bed-normal positions ( $y/h = 0.2, 0.5, 0.8$ ) for flow around the foam-covered cylinder. The symbols are darker with the increment in the magnitude of $y/h$ . The position of the cylinder is shown by the dashed lines. (b) Energy spectra of normalized turbulent kinetic energy ( $k/U_o^2$ ) for flow around the solid (denoted as CFD-C) and foam-covered (denoted as CFD-F) cylinder .....	66
Figure 4.6. (a) Mean streamwise velocity profiles normalized by inner scaling ( $U^+ = U/U_o$ , $y^+ = yU_o/\nu$ ), compared with the theoretical log-law profile, (b,c) normalized Reynolds stresses ( $\overline{u'^2}/U_o^2$ , $\overline{v'^2}/U_o^2$ , $-\overline{u'v'}/U_o^2$ ) .....	67
Figure 4.7. Comparison of the experimental and the numerical data: streamwise variation in (a,b) the normalized time-averaged velocities and (c,d,e) Reynolds stresses at mid-height of the cylinder ( $y/h = 0.5$ ).....	68
Figure 4.8. Comparison of experimental and numerical data for wall-normal distribution of dimensionless time-averaged streamwise velocity ( $U/U_o$ ) and Reynolds stresses ( $\overline{u'^2}/U_o^2$ , $\overline{v'^2}/U_o^2$ , $-\overline{u'v'}/U_o^2$ ) at (a-d) $x/d = 0.75$ , $z/d = 0$ ; (e-h) $x/d = 2.5$ , $z/d = 0$ ; and (i-l) $x/d = 1.5$ , $z/d = 0.5$ .....	70
Figure 4.9. (a) The distribution of coefficient of pressure ( $C_p$ ) at the mid-height of the cylinder ( $y/h = 0.5$ ) plotted against the azimuthal angle, (b) mean value of coefficient of drag ( $C_D$ ) plotted against the cylinder aspect ratio .....	71
Figure 4.10. Visualization of coherent flow structures in an instantaneous flow field by using iso-surfaces of $\lambda_2 h^2/U_o^2 = -20$ representing coherent structures around the (a,c) solid cylinder and (b,d) foam-covered cylinder, colored by magnitude of instantaneous velocity. The vortical structures can	



be referred as, 1: horseshoe vortex, 2: arch vortex, 3: tip vortex, 4: trailing vortex, 5: free end arch vortex .....	72
Figure 4.11. $U/U_o = 0$ iso-surface of the time-averaged streamwise velocity, illustrating the reverse flow region in the wake of the (a) solid and (b) foam-covered cylinder .....	73
Figure 4.12. Contours of time-averaged streamwise velocity ( $U/U_o$ ) and streamlines on two representative $x$ - $y$ planes ( $z/d = 0$ and $-0.5$ ) for (a,c) solid cylinder, (b,d) foam-covered cylinder. The blue contour line represents the zero mean streamwise velocity ( $U/U_o = 0$ ) .....	74
Figure 4.13. Contours of streamwise component of Reynolds normal stress ( $\overline{u'^2}/U_o^2$ ) at two representative $x$ - $y$ planes ( $z/d = 0$ and $0.5$ ) for (a,c) solid cylinder, (b,d) foam-covered cylinder. The horseshoe vortex is shown by '1' .....	75
Figure 4.14. Contours of time-averaged streamwise velocity ( $U/U_o$ ) superimposed by the streamlines at two representative $x$ - $z$ planes ( $y/h = 0.5$ and $1.01$ ) for (a,c) solid cylinder, (b,d) foam-covered cylinder. The area inside the blue contour line ( $U/U_o = 0$ ) represents the reverse flow region .....	77
Figure 4.15. Contours of time-averaged streamwise velocity ( $U/U_o$ ) superimposed by the streamlines at three representative $z$ - $y$ planes ( $x/d = 0.75, 1.5$ and $2.5$ ) for (a,b,c) solid cylinder, (d,e,f) foam-covered cylinder. The area inside the blue contour line ( $U/U_o = 0$ ) represents the reverse flow region. The vortical structures are identified as; 1: horseshoe vortex, 3: tip vortex, 6: base vortex .....	77
Figure 4.16. Streamwise velocity deficit ( $U_{def}$ ) on central vertical plane ( $z/d = 0$ ) at different bed-normal positions for (a) solid cylinder, and (b) foam-covered cylinder. The blue '+' sign indicates the maximum velocity deficit and the red '+' sign corresponds to $U_{def} = 0.2$ . (c) comparison of dimensionless length scales of the wake ( $L_1/d$ and $L_2/d$ ) for solid and foam-covered cylinder plotted against the data of Nicolai <i>et al.</i> (2020) for solid cylinder with aspect ratio 1 .....	79
Figure 4.17. Temporal history of the coefficient and energy spectra of (a,c) drag ( $C_D$ ), and (b,d) sway ( $C_S$ ). The dominant frequencies are shown by the dashed lines .....	79
Figure 4.18. Contour of the energy spectra along a transverse line ( $-1.5 \leq z/d \leq 1.5$ ) at mid-cylinder depth ( $y/h = 0.5$ ) and a vertical line ( $0 \leq y/h \leq 1.5$ ) at central horizontal plane ( $z/d = 0$ ) for (a,c) solid cylinder, and (b,d) foam-covered cylinder. Both lines are located at $x/d = 1.5$ .....	81
Figure 4.19. SPOD mode energy spectra on central vertical plane ( $z/d = 0$ ) for (a) solid cylinder, and (b) foam-covered cylinder .....	83
Figure 4.20. First two SPOD modes at $St = 0.14, 0.33, 0.56$ for (a-f) solid cylinder, (g-l) foam-covered cylinder .....	84
Figure 4.21. SPOD mode energy spectra on mid-horizontal plane ( $y/h = 0$ ) for (a) solid cylinder, and (b) foam-covered cylinder .....	85
Figure 4.22. First two SPOD modes at $St = 0.14, 0.33, 0.56$ for (a-f) solid cylinders, and (g-l) foam-covered cylinder .....	86

Figure A.1. Variation of  $\bar{N}_{peaks}$  with the change in (a) threshold kinetic energy deficit ( $K_{th}$ ) and (b) length of FOV ( $\mathcal{L}^+$ )..... 94

Figure A.2. PDF of  $N_{UMZ}$  corresponding to bin size (a)  $0.25U_\tau$  and (d)  $0.75U_\tau$  for the fully developed flow (T1&T3 at  $H = 0.170$  m) and the developing (T0 at  $H = 0.170$  m). Corresponding bed-normal distribution of  $R_{Q2/Q4}$  for bin size  $0.25U_\tau$  and  $0.75U_\tau$  for (b,e) the fully developed flow (T1&T3 at  $H = 0.170$  m) and (c,f) the developing (T0 at  $H = 0.170$  m)..... 95

## LIST OF ABBREVIATIONS/SYMBOLS

$b$	Width of the flume
$b_{ij}$	Reynolds stress anisotropy tensor
$C_D, C_S, C_P$	Coefficient of drag, sway and pressure
$d$	Outer diameter of the cylinder
$d_i$	Diameter of the inner cylinder
$d_f$	Diameter of a strut of the foam structure
$Fr$	Froude number
$F_u, F_v$	Flatness of velocity components
$h$	Height of the cylinder
$h/d$	Aspect ratio of the cylinder
$H$	Flow depth
$k$	Turbulent kinetic energy
$K$	Kinetic energy deficit
$L_1, L_2$	Length scales of the wake
$N_{UMZ}$	Number of momentum zones
$\bar{N}_{peaks}$	Average number of peaks
$P$	Probability density
$PIV$	Particle image velocimetry
$Re$	Reynolds number
$R_i$	Rank of a momentum zone
$R_{Q2/Q4}$	Ratio of shear stress contribution from Q2 and Q4
$R_{Q2+Q4/Q1+Q3}$	Ratio of combined shear stress contribution from Q2+Q4 and Q1+Q3
$St$	Strouhal number
$St_p$	Particle stokes number
$S_u, S_v$	Skewness of velocity components
$t_p$	Thickness of top and bottom plate of foam-covered cylinder
$t_{UMZ}$	Thickness of a momentum zone
$TNTI$	Turbulent/non-turbulent interface
$UMZ$	Uniform momentum zone
$U, V$	Time-averaged streamwise and wall-normal velocity
$U_{def}, V_{def}$	Velocity deficit of streamwise and wall-normal velocity component
$U_{MV}$	Modal velocity of a momentum zone

$U_o$	Depth-averaged inlet velocity
$U_\infty$	Free stream velocity or Maximum inlet velocity
$U_\tau$	Wall-shear velocity
$u', v'$	Velocity fluctuation of the streamwise and wall-normal velocity component
$u'_{\text{rms}}, v'_{\text{rms}}$	Root-mean-square of the velocity fluctuations
$x, y, z$	Coordinated in streamwise, wall-normal and transverse direction
$Y_{TNTI}$	Mean wall-normal position of TNTI
$Y_{UMZ}$	Mean wall-normal position of UMZs
$Y_{MV}$	Mean wall-normal position corresponding to modal velocity
$\delta$	Boundary layer thickness
$\delta^*$	Displacement thickness
$\kappa$	von Karman constant
$\nu$	Kinematic viscosity of fluid
$\Pi$	Wake parameter
$\rho$	Density of fluid
$\sigma$	Standard deviation
$\theta$	Momentum thickness
$\theta_s$	Azimuthal angle of the cylinder
$\bar{\theta}_s$	Average angle of separation
$\varepsilon$	Dissipation rate
$\Delta$	Resolution of grid
$\eta$	Kolmogorov length scale
$\lambda$	Taylor microscale

# CHAPTER 1

## INTRODUCTION

This thesis focuses on the flow field around wall-mounted bluff bodies, which is of practical relevance in hydraulic engineering practice. The wake characteristics of a wall-mounted fully-submerged solid circular cylinder and a foam-covered circular cylinder (height/diameter,  $h/d = 0.9$ ) are studied in the present research. The characteristics are evaluated under fully-developed approach flow conditions. To this end, the role of near-bed trips and the free surface perturbations are initially studied for proper conditioning of the approach flow. The wake flows that are generated behind the cylinders are then quantified using experimental and computational tools. Finally, the wake characteristics of the two cylinders are compared based on the mean and turbulent parameters, frequency response and the formation of coherent structures.

### 1.1. Background

The flow around a wall-mounted circular cylinder has been of interest to researchers for several decades due to their wide range of industrial applications and practical relevance. The examples include fluid flow around buildings, wind turbines, chimneys, bridge piers, oil platforms, trees, aquatic vegetations, etc. Compared to infinitely long cylinders, a finite wall-mounted cylinder is more relevant to many practical applications and a detailed understanding of such a flow field can be very useful in improving engineering design and retaining structural integrity in civil engineering applications.

The flow around finite surface-mounted circular cylinders creates a highly three-dimensional flow field and the flow characteristics are mostly guided by two geometric length scales, the height and diameter of the cylinder, the ratio of which is known as the cylinder aspect ratio. The present study is carried out with low aspect ratio cylinders, the flow around which can be very complex and consists of several well-defined coherent structures such as a horseshoe vortex, arch vortex, tip vortex, etc. With the introduction of foam, the flow characteristics can be significantly altered. Abdi *et al.* (2014, 2017) studied the wake of an infinite foam-covered cylinder and reported an asymmetric and longer wake region compared to the solid cylinder. A lower drag was found by Bhattacharyya *et al.* (2011) when a foam-coating was used on a solid cylinder. However, these studies are mostly concentrated on the performance of the foam in specific applications such as in heat exchange, drag reduction, etc. The details of the wake turbulence characteristics are not well understood, which has motivated the current comparative study of the wakes of the solid and foam-covered cylinders.

For a consistent comparison between the two cylinder wakes, the approach flow is maintained the same and is fully developed. The computational procedure for developing a fully developed flow is well-established and can be done by recycling of flow parameters from outlet to inlet. But it is not very straightforward in open channel flow experiments and requires fine adjustment of tripping and minimization of free surface perturbation. Initially, experiments were carried out using a basic trip and a light Styrofoam floater board placed at the inlet. With this condition, the flow at the measuring station was found to be developing in nature and a dip in the wall-normal distribution of mean streamwise velocity was noticed adjacent to the free surface. Therefore, a detailed study

on the effects of the trip and the floater was carried out to experimentally achieve a fully developed approach flow. The tripping intensity was gradually increased until the flow in the test section reaches the fully developed state. The floater board is found to have an adverse effect and may cause a deviation from the fully developed state although they are apparently used in open channel flow experiments to suppress the free surface waves. Therefore, the final experiments are carried out without any floater. With these considerations, a fully developed approach flow is generated in the flume and the experimental results are used for validating the inflow profile of the numerical simulation.

## 1.2. Motivations and objectives

The vortical structures around a cylinder can create a complicated flow field which may cause higher wind-load, flow induced vibrations, extreme scouring etc. In many engineering applications, passive flow controls such as splitter plates, cavitation, surface roughness are used since they are simple and less costly. Recently, researchers have started using a foam-coating as a medium of passive flow control. A porous coating can be used to reduce flow induced vibration (Bruneau *et al.* 2006, Bhattacharyya *et al.*, 2011), drag force (Bhattacharyya *et al.*, 2011, Klaussman and Ruck 2017) and aerodynamic noise (Sueki *et al.* 2010, Liu *et al.* 2014) and to increase the efficiency of heat transfer (Abdi *et al.* 2014, 2017). A proper implementation of the foam can be explored by investigating the flow characteristics around the foam structure, which is the main purpose of the present study.

The objectives of the thesis are as follows:

1. To achieve a fully developed approach flow both experimentally and numerically to maintain the consistency and universality of the wake study.
2. To characterize the fully developed flow using uniform momentum zones and identify the differences with a developing flow.
3. To study and minimize the effects of free surface perturbation in the test section caused by the floater.
4. To study the wake characteristics of a finite fully-submerged foam-covered circular cylinder through a comparative study with wake properties of a solid cylinder.

## 1.3. Thesis organization

The whole thesis is divided into four chapters. [Chapter 2](#) is devoted to the experimental study of fully developed approach flow which is achieved by varying the inflow tripping. The fully developed state is compared with the developing flow using momentum zone and quadrant analysis. [Chapter 3](#) describes the impact of free surface perturbations. The free surface perturbations are generated artificially by smooth and rough floater boards which are widely used in open channel flow experiments for conditioning inflow. [Chapter 4](#) is dedicated to the experimental and computational study on the wake characteristics of a solid and a foam-covered cylinder. The wakes of two cylinders are compared based on the mean and turbulent flow properties, frequency response and the formation of coherent flow structures. Chapters 2, 3 and 4 are presented independently and contains the relevant review of literature and methodology

corresponding to the specific research. **Chapter 5** summarizes the thesis with concluding remarks and discusses the scope for possible future work.

Table 1.1. Thesis organization

Chapter	Title
1	Introduction
2	Analysis of fully developed state in open channel flow using uniform momentum zones
3	Effect of free surface perturbation on the characteristics of fully developed smooth open channel flow
4	Quantification of the wake of a wall-mounted foam-covered circular cylinder
5	Conclusions and recommendations

## References

- Abdi, I. A., Khashehchi, M. & Hooman, K. 2017 Investigation of coherence behind a single foamed tube. *Fluid Mech. Res. Int. J.*, **1** (2), 45-54.
- Abdi, I. A., Khashehchi, M. & Modirshanechi, M. 2014 A Comparative analysis on the velocity profile and vortex shedding of heated foamed cylinders. *19<sup>th</sup> Australasian Fluid Mechanics Conference*, December 8-11, Australasian Fluid Mechanics Society, Australia.
- Bruneau, C. H. & Mortazavi, I. 2006 Control of vortex shedding around a pipe section using a porous sheath. *Int. J. Offshore Polar Eng.*, **16** (02).
- Bhattacharyya, S. & Singh, A. K. 2011 Reduction in drag and vortex shedding frequency through porous sheath around a circular cylinder. *Int. J. Numer. Methods Fluids*, **65** (6), 683-698.
- Klausmann, K. & Ruck, B. 2017 Drag reduction of circular cylinders by porous coating on the leeward side. *J. Fluid Mech.*, **813**, 382-411.
- Liu, H., Wei, J. & Qu, Z. 2014 The interaction of porous material coating with the near wake of bluff body. *J. Fluids Eng.* **136** (2), 021302.
- Sueki, T., Takaishi, T., Ikeda, M. & Arai, N. 2010 Application of porous material to reduce aerodynamic sound from bluff bodies. *Fluid Dyn. Res.* **42** (1), 015004.

## CHAPTER 2

### ANALYSIS OF FULLY DEVELOPED STATE IN OPEN CHANNEL FLOW USING UNIFORM MOMENTUM ZONES

A fully developed approach flow is necessary in fluid-structure interaction studies to maintain commonality among datasets obtained from different open channel facilities. Two-component planar PIV is used to study the characteristics of fully developed smooth open channel flow at constant Reynolds number of  $3.5 \times 10^4$ . The near-bed boundary layer is tripped to achieve a fully developed state and compared with the under or over-tripped cases. The Reynolds stresses and higher-order moments are used as indicators to establish the fully developed state. Flow properties are explored by identifying uniform momentum zones (UMZs) using probability density function of streamwise velocities. The instances are grouped based on the number of UMZs ( $N_{UMZ}$ ) and conditional averaging of flow variables of each group is used to correlate quadrant events with  $N_{UMZ}$ . Large-scale ejections are found in the logarithmic layer when  $N_{UMZ}$  is higher whereas a lower number indicates existence of large-scale sweeping motions. In the outer boundary layer, the fully developed state shows large-scale ejections for lower  $N_{UMZ}$  and large-scale sweeps for higher  $N_{UMZ}$ . Pointwise quadrant analysis shows similar vertical variability for the ratio of shear contribution to ejections and sweeps due to the free-surface constraint. The large-scale and pointwise quadrant events are correlated to depict variability in inner flow properties between developing and fully developed flow which cannot be recognized in the mean flow characteristics. The sweep events have much higher shear generation in the outer flow in fully developed state whereas shear stress contribution from ejection is lower than that in developing flow.

**Keywords:** turbulent boundary layers, boundary layer structure.

#### 2.1. Introduction

Turbulent boundary layers (TBLs) have been the focus of pioneering research since the nineteenth century. The technological advances in experimental measurement tools and techniques have played a major role in providing a deeper understanding of TBL flow. Viscous pipe flow experiments by Reynolds (1883), mixing length theory of Prandtl (1925), statistical description of turbulence by Taylor (1937) and turbulence anisotropy by Kolmogorov (1991) are some of the milestones that have contributed to our understanding. Some key aspects of open channel flows have been borrowed from classical TBLs due to the strong resemblance of the flow physics (Keulegan 1938, Roussinova *et al.* 2008). Similar to a classical TBL, the boundary layer in open channel flow is divided into four distinct regions: viscous sublayer, buffer layer, logarithmic layer and outer layer. Taken together, the first three layers up to and including the logarithmic layer are called the inner layer. The flow properties in the boundary layer are dominated by viscous effects and scaled by wall shear velocity  $U_\tau$  and kinematic viscosity  $\nu$ , whereas the outer flow is related to the free stream velocity  $U_\infty$  and flow depth  $H$ . Therefore, in boundary layer studies,  $U_\tau$  is widely used by researchers as a normalizing scale to the flow variables. However, in experimental fluid dynamics, it is generally challenging to accurately determine the velocity gradient in the viscous sublayer at moderate to high Reynolds number and therefore  $U_\tau$  is difficult to estimate directly



from the wall shear stress  $\tau_w$ . Consequently, several alternative methods have been proposed. A classical way of determining  $U_\tau$  was suggested by Clauser (1956) which involves fitting the experimental data for velocity  $U$  to the ‘log-law’, given by

$$\frac{U}{U_\tau} = \frac{1}{\kappa} \ln \left( \frac{y U_\tau}{\nu} \right) + B \quad (2.1)$$

where  $y$  is distance from the wall and, for a smooth wall TBL, the von Kármán constant  $\kappa$  varies in the range 0.39 and 0.42 and  $B$  is a constant between 5.0 and 5.5 (Hinze 1959; Steffler *et al.* 1985; Nezu & Rodi 1986; Kirkgöz & Ardiçlioğlu 1997; Balachandar & Ramachandran 1999; Balachandar *et al.* 2001; Roussinova *et al.* 2008; Sarkar 2016; Heidari *et al.* 2017; Miguntanna *et al.* 2020). However, the log-law is incapable of predicting the outer layer velocity distribution. To address this, Coles (1956) proposed a wake function  $w$  and modified the log-law to express the ‘mean velocity deficit’ as

$$\frac{U_\infty - U}{U_\tau} = -\frac{1}{\kappa} \ln \left[ \frac{y}{\delta} \right] + \frac{2\Pi}{\kappa} \left[ w \left( \frac{y}{\delta} \right) \right] \quad (2.2)$$

where  $\delta$  is the boundary layer thickness and  $\Pi$  is the wake parameter that represents the deviation of mean velocity from the log-law at  $y = \delta$ .

There is no consensus among researchers over the value of  $\Pi$  in open channel flow. Balachandar & Patel (2005) and Kirkgöz & Ardiçlioğlu (1997) reported a  $\Pi$  value of 0.4 and 0.1, respectively, whereas Cardoso *et al.* (1989) and Roussinova *et al.* (2008) suggested a value of -0.3. Hoffmann & Mohammadi (1991) observed that the wake parameter decreased with increasing inflow turbulence. Interestingly, the above experimental results show disagreement at the moderate and low Reynolds numbers typical of open channel flow. Many researchers have proposed and introduced different methodology to mitigate this inconsistency. Chauhan *et al.* (2009) in their comprehensive study showed Reynolds number dependency of  $\Pi$  in TBLs and proposed a modified defect law, referred to as the ‘velocity composite law’. Djenidi *et al.* (2019) suggested a new approach for determining  $U_\tau$  based on data fitting over the defect velocity profile. Monkewitz *et al.* (2007) and Chauhan *et al.* (2007) reported about a state of equilibrium in zero-pressure gradient (ZPG) turbulent boundary layers where  $\Pi$  becomes invariant. Although the ‘velocity defect law’ is widely accepted in wall-bounded flows, researchers are yet to agree on a common wake function and a specific range of values for  $\Pi$ . There are several instances when a different value of  $\Pi$  is reported for a similar range of Reynolds number. This uncertainty is related to the sensitivity of  $\Pi$  and  $\delta$  over a range of variables including, for example, the channel aspect ratio, shallowness of the flow, method of estimation and the nature of the approach flow. The value of  $\Pi$  and  $\delta$  may vary significantly with a small change in approach flow keeping the other parameters nominally constant. The approach flow in the measurement section is governed by two parameters, flow development length and the nature of tripping. These two parameters can be finely adjusted to stimulate a well-behaved turbulent boundary layer. Erm & Joubert (1991) varied the type of tripping using wire, distributed grit and cylindrical pins to match  $\Pi$  with Coles’ wake parameter. Marusic *et al.* (2015) showed that the flow characteristics at the same Reynolds number may differ if the tripping pattern and the flow development length are varied. Therefore, Reynolds number matching is a mandatory but not a sufficient criterion to compare two turbulent boundary layer flows.

Tripping is also widely used in open channel flumes to quicken the change of an initially laminar boundary layer to a turbulent state, and to make the flow fully developed within a shorter flow development length. An open channel flow is called fully developed if there is no streamwise variation of the flow variables. This is only possible when the boundary layer thickness is constant along the streamwise span of the flume, otherwise wall-normal distributions of the flow variables will vary between different streamwise positions based on the corresponding boundary layer thickness. The primary way of generating a fully developed open channel flow is by allowing the flow to develop gradually from the inlet section of a flume until the boundary layer thickness is equivalent to the flow depth. Since this procedure requires a very long flow development length, in most laboratory flumes a fully developed state cannot be generated without inflow tripping. But tripping does not necessarily ensure a fully developed state in open channel flow as it can only reduce the requirement of the flow development length to a certain extent. The size and the roughness height of the trip can be optimally adjusted to ensure a fully developed flow in the measurement section, provided an adequate flow development length corresponding to the flow depth and Reynolds number is available. With a lower level of tripping (referred to here as an under-tripped case) the flow can still be in a developing state in the test section. On the other hand, if the intensity of perturbations generated from the trip is very high (i.e., over-tripped case), the boundary layer thickness may grow rapidly but it takes a longer distance to dissipate the additional energy before reaching to a well-behaved canonical state. Therefore, if the other hydraulic parameters are held constant, there should be one suitable trip condition (a narrow range of roughness heights of the trip) for which the boundary thickness will be equal to the flow depth and retain the canonical behaviour. This flow state can be called a fully developed flow.

To identify if the flow has become fully developed, a criterion must be set to determine the boundary layer thickness. The conventional way is to find the bed-normal coordinate at which streamwise velocity is  $0.99U_\infty$ . Since the free stream region is not theoretically present in fully developed open channel flow,  $U_\infty$  is commonly taken as the maximum velocity near the free surface. Therefore, this definition of boundary layer thickness in open channel flows is highly influenced by secondary currents, free surface perturbations and confinement of the upward momentum transfer, thus causing disparity among the experimental studies. The evidence of this discrepancy is very prominent from the discussion of the wake function. Therefore, it is perhaps technically more suitable to quantify the boundary layer thickness using the wall-normal distribution of Reynolds stresses and higher-order moments which can directly be correlated with the intricate flow characteristics such as depth-wise variation of turbulence generation, intermittency, ejection and sweep events (Andreopoulos *et al.* 1984; Gad-el Hak & Bandyopadhyay 1994; Balachandar & Patel 2005; Balachandar & Bhuiyan 2007). The boundary layer thickness can be more precisely defined as the wall-normal position above which Reynolds stresses and higher-order moments becomes nominally constant and this definition is consistent with previous studies (Flack *et al.* 2005; Roussinova *et al.* 2008). Using this approach will enable us to consistently define a fully developed state in open channel flow.

Since the development of laser anemometry and non-intrusive probes, extensive research in assessing the characteristics of open channel flows commenced in the early 1980s. The wall-bounded flow in an open channel is found to differ from that of a classical TBL due to the existence of the free surface which behaves like a weak wall and can significantly influence the inner flow (Nezu, 2005). These dissimilarities can be seen prominently in temporal flow characteristics if the

boundary layer thickness is very close to the free surface such as that in the fully developed state. As mentioned earlier, an adequate tripping and an accurate estimate of boundary thickness can be used to generate a fully developed state based on the time-averaged characteristics of open channel flows. Once the depth-wise variation of time-averaged variables are consistent with the flow physics of a fully developed flow, the temporal aspects can be explored accurately.

The deviation in temporal flow characteristics of a fully developed open channel flow from that of a classical TBL is mostly caused by the vertical confinement due to the free surface. As momentum transfer near the free surface is restricted in the vertical direction, it has to be transferred through the surrounding fluid to the other directions. A momentum zone analysis will be useful to gain insights into these attributes of the flow field. Momentum zone analysis has been previously carried out in ZPG turbulent boundary layers (Adrian *et al.* 2000; de Silva *et al.* 2014, 2017; Eisma *et al.* 2015; Laskari *et al.* 2018) and in pipe flows (Chen *et al.* 2020), which has enhanced our understandings of large-scale motions. Meinhart & Adrian (1995) observed layers of uniform momentum in turbulent boundary layers. Each of the momentum zones corresponds to a ‘modal velocity’ and can be identified by the local peaks in the probability density function of streamwise velocity (Adrian *et al.* 2000). Chauhan *et al.* (2014b) proposed a method to differentiate between the rotational and irrotational regions, and the interface between these regions is commonly known as the turbulent/non-turbulent interface (TNTI). Uniform momentum zones lie inside the TNTI and Eisma *et al.* (2015) pointed out co-existence of these momentum zones in the region between the bed and the TNTI. de Silva *et al.* (2016) correlated the momentum zones with the flow Reynolds number. The number of zones increases log-linearly with the increase of Reynolds number and the thickness of these zones increases away from the bottom wall. Laskari *et al.* (2018) extended the analysis to time evolution of the momentum zones. They observed large-scale quadrant 2 (Q2,  $u' < 0, v' > 0$ ) events when the number of momentum zones is large and quadrant 4 (Q4,  $u' > 0, v' < 0$ ) events with a smaller number of momentum zones. The Q2 and Q4 events correspond to ejections and sweeps, respectively (Lu & Willmarth 1973) and thus create a temporal coherence of large-scale fluid motions associated with the momentum zones.

In fluid-structure interaction studies, maintaining a fully developed condition for the flow approaching the structure is an important consideration to achieve repeatability of the flow behaviour among different experimental facilities. If the approach flow is in a developing state, the vertical distribution of the mean and turbulence quantities will vary in the streamwise direction and be different from setup to setup. Therefore, the primary focus of the present research is to stimulate a fully developed open channel flow accurately and efficiently varying the inflow tripping. The bed-normal distributions of mean velocity, Reynolds stresses and higher order moments of the test cases corresponding to different trips are compared in this context. The self-similarity of the fully developed flow is also validated using velocity data of the previous literatures. The second objective of this paper is to investigate the effect of free surface on the temporal aspects of a fully developed flow using uniform momentum zone analysis. The variation in quadrant events between the developing and fully developed case is identified using conditional averaging of the instantaneous flow variables corresponding to different number of momentum zones.

## 2.2. Experiment setup and test conditions

The experiments were carried out in a recirculating open channel flume at the Hydraulic Engineering Research Laboratory at the University of Windsor. A schematic diagram of the flume

is presented in [figure.2.1](#). The flume has a rectangular cross-section with a length of 16 m, a width (b) of 1.2 m and a depth of 0.8 m. The sides and bottom walls are made of transparent glass to provide optical access to the flow. The upstream settling tank ensures reduction of inflow perturbations and honeycomb flow straighteners are also used to manage the turbulence level. The tailgate at the downstream end of the flume controls the water depth. The pump was operated at a constant frequency of 20 Hz to maintain a Reynolds number ( $Re_H$ ) of 39 000 based on flow depth  $H$  and free stream velocity  $U_\infty$ . Since a clear free stream region is not present in a fully developed open channel flow,  $U_\infty$  is commonly taken as the maximum velocity near the free surface. The approach flow was studied using two aspect ratios,  $b/H = 9$  ( $H = 0.135$  m) and  $7$  ( $H = 0.170$  m). These aspect ratios are high enough ( $> 5$ ) to minimize the effect of secondary flows (Nakagawa & Nezu 1977; Nezu & Rodi 1986; Yang *et al.* 2004; Bonakdari *et al.* 2008; Mahananda *et al.* 2019). If the aspect ratio is high enough, a section of the flow in the central region of the channel can be considered to be nominally two-dimensional (Nasif *et al.* 2020). In this case there is no measurable spanwise variation in mean streamwise velocity profile over the mid 80% of the flume width and the ratio of mean spanwise velocity to mean streamwise velocity is less than  $\pm 0.005$ . Over a streamwise length of 5 m, the change in water depth is approximately 0.5 mm, corresponding to a pressure gradient parameter ( $\beta$ ) of -1.3 in the low aspect ratio tests and -2.1 in the higher aspect ratio tests. These values indicate that the flow is mildly accelerating (Peruzzi *et al.* 2020). However, as suggested by Kironoto & Graf (1995); Song & Chiew (2001); Pu *et al.* (2018), the effect of non-uniformity can be considered as negligible for the present values of  $\beta$ .

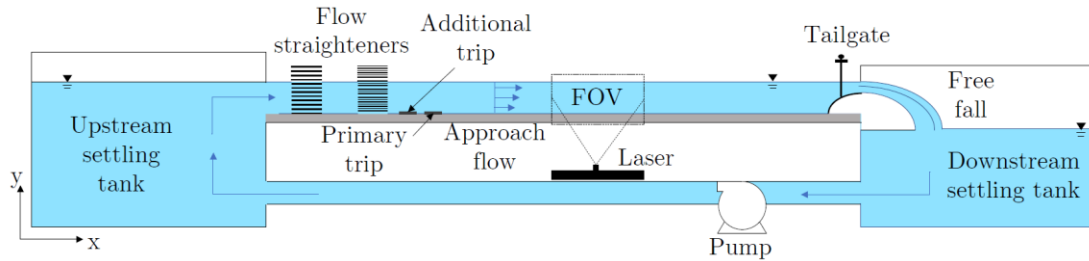


Figure 2.1. Schematic of the recirculating flume and test set up

The tests were conducted on a smooth bed with and without trips to generate the desired flow conditions. A primary trip (T1) made of a patch of coarse grain sand particles ( $k_s = 2.5$  mm, width = 5 mm) was glued to the bed between the flow straightener and the test section, spanning the width of the flume. The trip was located 2 m downstream of the flow straightener. The PIV field-of-view (FOV) was set at 2.5 m downstream of the trip. An evaluation of the results indicated that this trip was not sufficient to generate a fully developed flow at the measuring section. An additional trip (denoted as T2 or T3) was used at a distance of 1 m upstream of the primary trip and the roughness height and width of this trip were varied to generate fully developed flow at the two flow depths ( $H = 0.135$  and  $0.170$  m). Details of the trips and test setups are provided in [table 2.1](#). The flow parameters are shown only for the fully developed case at two depths of 0.135 and 0.170 m. The free stream velocities (maximum velocities) are approximately 0.29 and 0.23 m/s at these two depths, which corresponds to a constant value of  $Re_H = 39\,000$ . Reynolds numbers ( $Re_\theta$ ) based on the momentum thickness ( $\theta$ ) are 4205 and 3818, respectively. The experiments are carried out at a

low Froude number ( $Fr \approx 0.2$ ) and the shape factors of the mean velocity profiles ( $\delta^*/\theta$ ) are approximately 1.3, where  $\delta^*$  is the displacement thickness.

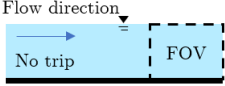

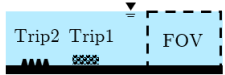
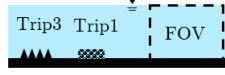
Inflow conditions	Test names	Test conditions																													
 <p>Flow direction No trip      FOV</p>	T0: No trip is used, similar to flat plate boundary layer	<b>Trip and flow details:</b>																													
 <p>Trip1      FOV</p>	T1: Trip1; Primary trip	<table border="1"> <thead> <tr> <th>Trips</th> <th>Distances from FOV (m)</th> <th colspan="4">Trip details (mm)</th> </tr> </thead> <tbody> <tr> <td>T1</td> <td>2.5</td> <td><math>k_s = 2.5</math></td> <td colspan="3">width= 50</td> </tr> <tr> <td>T2</td> <td>4.0</td> <td><math>k_s = 5</math></td> <td colspan="3">width= 50</td> </tr> <tr> <td>T3</td> <td>4.0</td> <td><math>k_s = 10</math></td> <td colspan="3">width= 100</td> </tr> </tbody> </table>						Trips	Distances from FOV (m)	Trip details (mm)				T1	2.5	$k_s = 2.5$	width= 50			T2	4.0	$k_s = 5$	width= 50			T3	4.0	$k_s = 10$	width= 100		
Trips	Distances from FOV (m)	Trip details (mm)																													
T1	2.5	$k_s = 2.5$	width= 50																												
T2	4.0	$k_s = 5$	width= 50																												
T3	4.0	$k_s = 10$	width= 100																												
 <p>Trip2 Trip1      FOV</p>	T1&T2: An additional trip T2 with T1 to make 0.135 m depth flow fully developed	Flow depths (m)	$U_\infty$ (m/s)	$Re_H$	$Re_\theta$	$Fr$	Shape factors																								
		0.135	0.29	39 000	4205	0.25	1.32																								
 <p>Trip3 Trip1      FOV</p>	T1&T3: An additional trip T3 with T1 to make 0.170 m depth flow fully developed	0.170	0.23	39 000	3818	0.18	1.29																								
		* $Re_\theta$ and shape factors presented here are for fully developed condition.																													

Table 2.1. Details of the test conditions, trip characteristics and flow parameters

Velocity measurements were carried out at the vertical mid-plane ( $x$ - $y$  plane, where  $x$  and  $y$  are the streamwise and bed-normal directions, respectively) of the flume using a two-component planar PIV system consisting of dual pulse Nd:YAG lasers of 532 nm wavelength and 50 mJ/pulse with a maximum output of 800 mJ. Each laser pulse duration is 4 ns and the time interval between two pulses was set to be 2.3 ms. The laser emitter box was placed underneath the flume to illuminate the flow orthogonally from the bottom. Two cylindrical lenses with focal lengths of -15 mm and -25 mm were attached at the laser outlet to stretch the beam into a vertical laser sheet of 1 mm thickness. A spherical lens (focal length of 1000 mm) was mounted at the top of the cylindrical lenses, to maintain equal intensity at the edges of the laser sheet. A PowerViewPlus 8 MP CCD camera was installed on one side of the flume and aligned orthogonally with the laser sheet. Nikon AF NIKKOR 50mm f/1.8D lens was used to acquire the images of resolution 3320 pixels  $\times$  2496 pixels. The camera was operated in dual capture mode synchronized with the laser pulse repeat frequency of 2.9 Hz. Before starting the experiment, the flume water was circulated through a sand filter ( $\sim 20 \mu\text{m}$ ) for several days to remove unwanted particles from the tap water. The flow was then seeded with 10  $\mu\text{m}$  spherical silver-coated hollow glass spheres with an effective density of 1100 kg/m<sup>3</sup>. The ability of the particles to faithfully follow the flow was assessed from the particle's Stokes number ( $St_p$ ) which was determined by the ratio of particle response time to turbulence time scale (Longmire & Eaton 1992).  $St_p$  was found to be  $5.31 \times 10^{-5}$  which satisfies the criterion proposed by Clift *et al.* (1978):  $St_p \ll [2(\rho_p/\rho)+1]/9 = 0.36$ . Four thousand image pairs were taken for each test condition and processed using PIVlab (Thielicke & Stamhuis 2014). After background subtraction, the images were pre-processed using the Contrast-Limited Adaptive Histogram Equalization (CLAHE) technique (Pizer *et al.* 1987). Intensity capping (Shavit *et al.* 2007) and Wiener denoise filtering (Wiener 1964) were used to minimize the error. The particle illuminations between image pairs were correlated by a Fast Fourier Transform window deformation algorithm

where the interrogation window of  $64 \times 64$  pixels is reduced to  $16 \times 16$  pixels with a spatial overlap of 50%. The data were then post-processed in PIVlab using standard deviation and median filters with a predefined threshold value to remove and replace bad vectors. Less than 5% of vectors were identified as bad and replaced by interpolated vectors. MATLAB codes were developed to calculate mean and turbulence quantities, as well as for the momentum zones and quadrant analysis.

Uncertainty in PIV measurements can be caused by several parameters, such as background noise, the relative velocity between particles and flow, unpaired particle images, calibration errors, optical system misalignment, inaccuracy of data processing algorithm, etc. Details of the uncertainty analysis are provided in the literature (Forliti *et al.* 2000; Singha 2009; Roussinova 2009; Sciacchitano *et al.* 2015). In the present study, the total uncertainty (at the 95% confidence interval) in the velocity measurement was calculated to be  $\pm 0.0055$  m/s ( $\approx 2\%$  of  $U_\infty$ ). Further investigation was carried out to quantify the error in the higher-order statistics. The whole data set was divided into five sets consisting of randomly chosen 500, 1000, 2000, 3000 and 4000 distinct samples. The uncertainties in mean and turbulence parameters were estimated for each sample. As shown in figure 2.2, the deviations between two corresponding sample sizes tend to reach a converged value with the increase of sample size. For example, the mean deviation of Reynolds shear stress value between 500 and 1000 image pairs is 7%, while it is reduced to 2% between 3000 and 4000 image pairs. This ensures that the experimental data are within a reasonable range of variation and 4000 instances are sufficient to study the higher-order statistics for this type of flow field. The uncertainty in each of the variables compares favourably with that reported in the literature (Flack *et al.* 2005; Singha 2009).

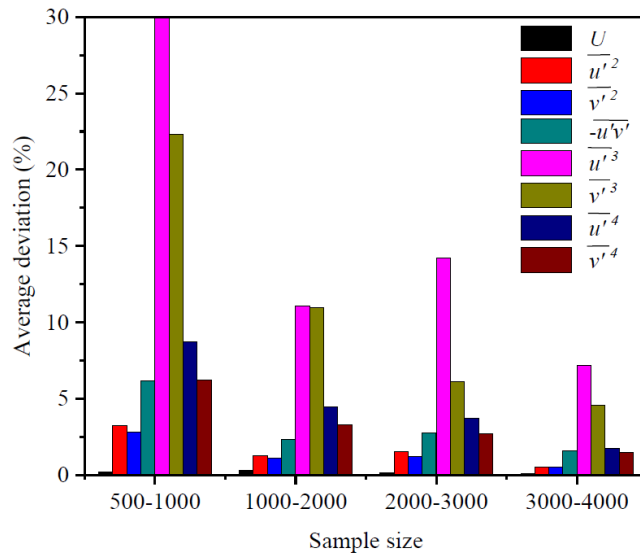


Figure 2.2. Deviation in the mean and turbulence quantities with increase in sample size

### 2.3. Shear velocity

An accurate estimation of shear velocity is necessary for the inner scaling of the mean and turbulence parameters. In this paper, the value of  $U_\tau$  is estimated by a modified Clauser chart method that optimizes the double-averaged mean streamwise velocity profile ( $U$ ) against the log-law by an iterative curve fitting algorithm. The double-averaging technique involves both time and

space averaging of the velocity data over the whole FOV (Nikora *et al.* 2007; Cameron *et al.* 2008; Sarkar & Dey 2010; Mignot *et al.* 2011). Initially, the time averaging is done over 4000 instances at each data point. The time-averaged data is then spatially averaged in the streamwise direction, i.e., the mean data points corresponding to a constant bed-normal position are averaged over the FOV. Thus, the whole FOV is collapsed into one double-averaged profile. In general, spatial averaging is not valid in the developing flow because the velocity profiles are varying in the streamwise direction. To check its validity, streamwise variation of time-averaged velocity and the turbulence quantities at three different vertical locations along the depth ( $y/H = 0.2, 0.5, 0.8$ ) were monitored. The deviation over the 250 mm long FOV is negligible. Double-averaging is used here as more data will provide better statistics of higher-order turbulence characteristics.

In the present study,  $U_\tau$  is determined by optimizing the functions  $f_1$  and  $f_2$  defined in equations 2.3 and 2.4. The optimization is carried out using the double-averaged mean streamwise velocity data in the range of the logarithmic layer:  $30 \leq y^+ \leq 0.2Re_\tau$  (where  $Re_\tau = U_\tau H/\nu$ ) (Balachandar & Patel 2005). Initially,  $U_\tau$  is calculated from the total shear stress method:  $U_\tau^2 = (\nu \partial U / \partial y - \overline{u'v'})_{y=0}$ . This equation assumes a linear distribution of Reynolds shear stress throughout the depth and the value of  $U_\tau$  is estimated by extrapolating the linear region of shear stress profile to the bed (Flack *et al.* 2005; Roussinova *et al.* 2008). However, this value is only used as an initial guess since the uncertainty of this method is high. The value of  $\kappa$  and  $B$  are taken as 0.41 and 5, and not varied. In the beginning, the function  $f_1$  (equation 2.3) is optimized by a linear least square fit in the form of  $y - mx = 0$ , forcing the intercept to be zero. The slope of this line is  $U_\tau/\kappa$ . In the next step, function  $f_2$  (equation 2.4) is optimized in a similar way to determine  $U_\tau$ . If both of the optimization processes provide a similar value, the output is taken as the final value of  $U_\tau$ . Otherwise, if the difference between the two  $U_\tau$  values is higher than a prescribed threshold value,  $y_o$  is adjusted until a good match is achieved. The  $y_o$  is introduced as a small correction to the  $y$  coordinate ( $y_i$ ) of the processed data as the location of the true  $y = 0$  coordinate depends on the accuracy in masking the PIV images. This correction also helps to avoid the log-law mismatch near the transition region. The final  $y$  coordinates are modified with corresponding  $y_o$  values as  $y = y_i + y_o$ .

$$f_1(U_\tau) = \frac{dU}{dy} - \frac{U_\tau}{\kappa} \frac{1}{(y_i + y_o)} \quad (2.3)$$

$$f_2(U_\tau) = U - \frac{U_\tau}{\kappa} \ln \left[ \frac{(y_i + y_o)}{\nu} \right] - U_\tau B \quad (2.4)$$

The values of  $U_\tau$  for different test conditions are presented in table 2.2. The deviations among them are calculated with a reference  $U_\tau$  value at each depth, i.e., the test case T1&T2 at  $H = 0.135$  m and T1&T3 at  $H = 0.170$  m. These two cases are fully developed conditions and will be discussed in detail in the following sections.  $U_\tau$  values for other test cases are compared with the values in corresponding fully developed states and show a variation of up to 5%. Similarly,  $U_\tau$  values for the two fully developed states are calculated for the time-averaged velocity profiles at each streamwise location and these values of  $U_\tau$  (normalized by  $U_\infty$ ) are presented in figure 2.3(a). The distribution of  $U_\tau/U_\infty$  is similar in both tests and no significant variation is noticed over the span ( $\mathcal{L}$ ) of the FOV. Finally, the streamwise variation of the shape factor is presented in figure 2.3(b) since the integral quantity is a more reliable parameter in this context. The variation of shape factor over the

FOV is found to be minor, ensuring our expectation of the fully developed states and the validity of the double averaging.

Trips	$U_\tau$ (m/s)	
	$H = 0.135$ m	$H = 0.170$ m
T0	0.0123 (2.5%)	0.0095 (5.5%)
T1	0.0119 (-0.8%)	0.0090 (-1.1%)
T1&T2	0.0120*	0.0090 (-1.1%)
T1&T3	0.0125 (4.2%)	0.0091*

Table 2.2. Shear velocities for different test cases. \* indicates fully developed conditions.

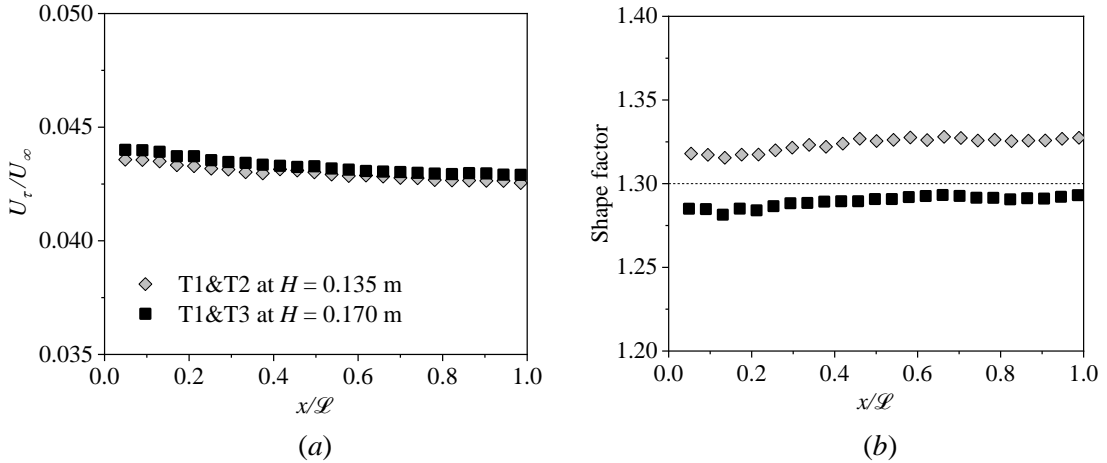


Figure 2.3. Streamwise variation of (a) the ratio of wall-shear velocity and maximum velocity ( $U_\tau/U_\infty$ ) and (b) shape factor for the fully developed states

## 2.4. Mean velocity

Mean velocity profiles for different test cases are presented with inner scaling ( $U^+ = U/U_\tau$  and  $y^+ = yU_\tau/b$ ) in figure 2.4. Velocity profiles for tests T1, T1&T2, and T1&T3 have been shifted by a constant value to enhance visualization. The dashed lines represent the log-law in each case. The edge between the inner and outer layer, as indicated by the vertical lines, is identified based on the position where a significant deviation ( $> 20\%$ ) occurs between the mean profiles and the log-law. Generally, the thickness of the logarithmic layer is considered up to  $0.2\delta$ , but in the context of the present analysis the boundary layer thickness is unknown. Therefore, the location of the outer layer is approximated based on the deviation from the log-law to provide a qualitative comparison between the test cases. The locations of the outer layer edge in test T0, T1, T1&T2, T1&T3 are approximately at  $y^+ = 300, 300, 475, 700$ , respectively. For the test T1&T3, the outer layer is very narrow, and the deviation is minimum. These deviations are an indication that the strength of the wake changes with the change in trip size. Each of the trip conditions is likely to have unique wake characteristics and it is difficult to identify the fully developed condition using only the log-law.



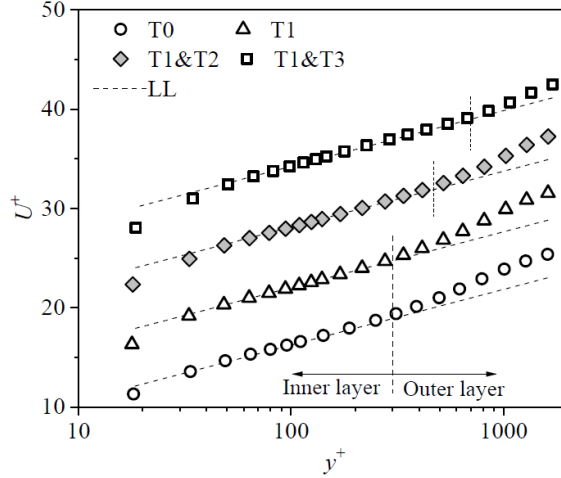


Figure 2.4. Mean streamwise velocity profiles at  $H = 0.135$  m normalized by inner scaling, compared with the log-law profile. Velocity profiles for tests T1, T1&T2, and T1&T3 are shifted vertically by a constant value to enhance visualization.

As mentioned earlier, Coles (1956) was among the first to propose an additional term in the log-law that consists of a wake strength parameter to quantify the deviation of the mean profile from the law-of-the-wall in the outer region. This new equation with the additional term is widely known as the ‘velocity defect law’. The wake parameter  $\Pi$  can be derived from the upper and lower boundary conditions of velocity in the outer region. Several researchers have proposed different forms of the wake function (Coles 1956; Cardoso *et al.* 1989; Guo *et al.* 2005). Based on Granville’s (1976) formulation, Krogstad *et al.* (1992) proposed an alternative velocity defect equation for a ZPG turbulent boundary layer, which can be expressed in the functional form  $f(\Pi) = 0$ , where

$$f(\Pi) = \frac{U_\infty - U}{U_\tau} - \frac{2\Pi}{\kappa} \left[ 1 - \frac{1}{2\Pi} \left( (1+6\Pi) \left(\frac{y}{\delta}\right)^2 - (1+4\Pi) \left(\frac{y}{\delta}\right)^3 \right) \right] - \frac{1}{\kappa} \ln \frac{y}{\delta} \quad (2.5)$$

The defect equation proposed by Krogstad *et al.* (1992) consists of four unknown variables:  $\kappa$ ,  $U_\tau$ ,  $\delta$  and  $\Pi$ , and all these variables can ideally be optimized simultaneously for a given data set. However, this optimization procedure is highly sensitive to the initial guess values and a wrong initial guess may converge the solution to an erroneous estimation of these parameters. This dependency can be made less critical by reducing the number of unknowns. Based on the discussion so far, the magnitude of  $\kappa$  and  $U_\tau$  are known to us and these variables are taken out of the optimization procedure. However, our aim is to estimate the value of  $\Pi$  accurately without any bias to the value of any other parameter. The magnitude of  $\delta$  varies between 0 and  $H$  and the value of  $\Pi$  may vary significantly for an initial guess value of  $\delta$  within this range. Therefore, we have chosen to use the classical definition of the boundary layer thickness to estimate  $\delta$  so that the optimization process is independent of any guess value. It is worth mentioning here that the magnitude of  $\Pi$  is still dependent on the value of  $\kappa$ ,  $U_\tau$  and  $\delta$  but a small change in their values will not lead to an abrupt deviation and inaccurate estimation of  $\Pi$  since these variables are not included in the optimization process. The magnitude of  $\delta$  is determined following the standard procedure, i.e., by the bed-normal location where the mean streamwise velocity is  $0.99U_\infty$ . Having set the values of  $\kappa$ ,  $U_\tau$  and  $\delta$ , the value of  $\Pi$  is estimated by minimizing function  $f$  (equation 2.5). In figure 2.5(a), defect profiles for all trip conditions at a flow depth of 0.135 m are plotted against the profiles

predicted from the Krogstad's defect equation. The profiles of T1, T1&T2, and T1&T3 are shifted vertically by a constant value to enhance visualization. The figure shows that there is good agreement between the experimental data and the defect equation for all test cases. The wake parameter varies between 0.3 and 0.55. The Reynolds number based on displacement thickness ( $Re_{\delta^*}$ ) is 4200. A reasonable value of  $\Pi$  at this value of  $Re_{\delta^*}$  is  $0.4 \pm 0.15$  as reported by several studies in open channel flow and turbulent boundary layers (Balachandar & Patel 2005; Chauhan *et al.* 2009). In [figure 2.5\(a\)](#), it can be seen that the VDL in all test cases is validated by the experimental data, indicates the flow follows a canonical behaviour. Since the value of  $\Pi$  (as shown in the table inset in [figure 2.5a](#)) is different among the test cases, some distinction must be present in their wake characteristics. Therefore, the flow in all four tests cannot be in the fully developed state although they may follow a canonical boundary layer flow behaviour since the fully developed condition is a unique state of open channel flow. Hence, conforming to VDL is mandatory but not sufficient to ensure a fully developed flow when the boundary layer thickness is not known. In wind tunnel TBL, a clear free stream region is present where the streamwise velocity is constant, permitting a precise definition of boundary layer thickness. But in the case of open channel flow, the free surface acts as a weak wall (Nezu 2005) and provides a vertical constraint which may influence the inner flow significantly. This influence is more prominent when the boundary layer edge is very close to the free surface and a deduction of boundary layer thickness based on  $0.99U_\infty$  can be deceiving as seen in [figure 2.5\(a\)](#). The present results were also compared with the composite velocity profile proposed by Chauhan *et al.* (2007) for the ZPG turbulent boundary layer and a similar ambiguity was noticed with the traditional definition of boundary layer thickness.

In previous studies, the boundary layer thickness has been shown to be correlated to the turbulence characteristics (Balachandar & Patel 2005; Flack *et al.* 2005; Roussinova *et al.* 2008; Marusic *et al.* 2015). Based on that observation, the boundary layer thickness ( $\delta'$ ) can be defined as the bed-normal position above which the streamwise Reynolds stress becomes constant and the turbulence intensity is minimum. The distributions of Reynolds stresses are presented in the following sections and used to determine the values of  $\delta'$  for difference test cases. The estimated boundary layer thickness based on the two definitions are compared below in [table 2.3](#).

H	0.135 m				0.17 m			
Case	T0	T1	T1&T2	T1&T3	T0	T1	T1&T2	T1&T3
$\delta/H$	0.89	0.89	0.91	0.94	0.85	0.84	0.83	0.89
$\delta'/H$	0.60	0.76	0.95	1.00	0.52	0.55	0.65	0.93

Table 2.3. Boundary layer thickness.

With the revised definition of boundary layer thickness, the defect profiles for all test cases are presented in [figure 2.5\(b\)](#). Except for the test case T1&T2 (at  $H = 0.135$  m), the defect profiles start to deviate from the theoretical profile near the boundary layer edge although the value of  $\Pi$  is readjusted, which establishes the presence of a unique fully developed condition. It is worth noting here that the magnitude of the wake parameter (shown in the tables in [figure 2.5](#)) and the boundary layer thickness ([table 2.3](#)) is similar in test T1&T2 for both definitions of the boundary layer thickness and the flow state in this test can be considered as the most fully developed among the four cases. However, the difference between [figures 2.5\(a\)](#) and [2.5\(b\)](#) is minor and any conclusion made based solely on this may not be reliable. The true purpose of this analysis is to reveal the root

of the ambiguity while matching the defect law. It is quite clear from this discussion that the validation of the experimental data with the log-law and the defect law may not be sufficient to identify a fully developed flow if the boundary thickness is not accurately estimated. Nevertheless, when the boundary layer thickness is known, this validation is mandatory in a fully developed open channel flow.

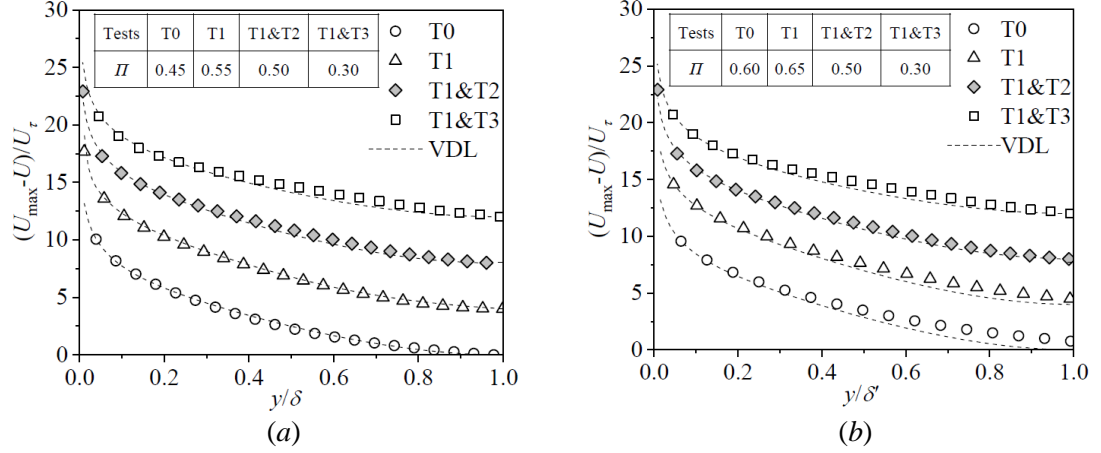


Figure 2.5. Collapse onto Krogstad’s velocity defect law (VDL) for different trip conditions at  $H = 0.135$  m with the normalization of  $y$  coordinate by (a)  $\delta$  and (b)  $\delta'$ . The profiles of T1, T1&T2, and T1&T3 are shifted by a constant value.

## 2.5. Reynolds stresses and higher-order moments

The Reynolds stresses normalized by  $U_\infty$  and  $U_\tau$  are presented in figure 2.6. At both depths, tests T0 and T1 show a zone of near-constant Reynolds stresses adjacent to the free surface except for the bed-normal component of Reynolds stress at  $H = 0.135$  m. The magnitude of the bed-normal component of Reynolds stress must be zero at the free surface and a sudden decrease from the constant magnitude can be seen in the region  $0.85 \leq y/\delta' \leq 1.0$  (figure 2.6b,e). This is more prominent in case of lower flow depth ( $H = 0.135$  m) since the thickness of free stream flow is much less than the higher flow depth ( $H = 0.170$  m). Also, a similar effect can be found in the distributions of Reynolds shear stress in figures 2.6(c) and (f). However, the zone of constant Reynolds stresses corresponds to the region above the boundary layer and is more prominent at the higher flow depth (figure 2.6d,e,f). In the presence of a free stream region above the boundary layer, the stress in this zone should ideally be zero, but it has a very small value because of the influence of the free surface in open channel flow. In the present study, the boundary layer thickness is determined as the bed-normal location above which the streamwise component of Reynolds stress is constant and presented in table 2.3 corresponding to different test cases. Since the boundary layer thickness in test T0 and T1 is below the height of the free surface, these two test conditions are considered to be in the developing regime. At  $H = 0.135$  m, the flow in the case T1&T2 is the closest to the theoretical fully developed state. However, at  $H = 0.170$  m there is a significant constant intensity zone above  $y/H = 0.65$ , even with the additional trip T2. The trip size of T2 was further increased gradually leading to the test case T1&T3, which is seen to be a good

approximation of a fully developed state at higher flow depth. The results from the intermediate increments in trip size are not included here for brevity. Test cases T1&T2 at  $H = 0.135$  m and T1&T3 at  $H = 0.170$  m exhibit a gradual transition from the highest stress close to the wall, to the lowest value near the free surface. The test cases with a lower trip size than the fully developed state are referred to as under-tripped cases (T0 and T1 at  $H = 0.135$  m and T0, T1, T1&T2 at  $H = 0.170$  m) and the flow in these tests are in the developing regime in the test section. A clear free stream region with a constant turbulence intensity zone adjacent to the free surface is visible in the under-tripped cases. On the other hand, the test case T1&T3 at  $H = 0.135$  m is an over-tripped case since the turbulence generated by the trip is much higher than the fully developed flow and this excess turbulence is not dissipated with the upstream flow length. Marusic *et al.* (2015) have mentioned that a unique tripping is required to stimulate a well-behaved turbulent boundary layer flow at a specific free stream velocity. They found a deviation from canonical behaviour when the velocity measurements are conducted close to the trip, which is equivalent to the over-tripped case T1&T3 (at  $H = 0.135$  m) in the present study. Interestingly, the distributions of Reynolds stresses within the logarithmic layer ( $y/\delta' \leq 0.2$ ) show a good collapse on to each other. Above this depth ( $y/\delta' > 0.2$ ), the slopes of the stress profiles start to differ in the outer layer with the variation in trip size. For example, going from T0 to T1&T2, the slope of the profiles is steeper above a distinct point of inflection (marked as A, B and C in figures 2.6 a,b,c) until the fully developed state is reached, then suddenly a bulge appears which is likely due to excess turbulence in the over-tripped case (T1&T3 at  $H = 0.135$  m).

Based on the constant turbulent intensity zone, the magnitude of  $\delta'$  is estimated for each test case and compared with the values of  $\delta$  in table 2.3. Interestingly, with the usual definition, the boundary layer thicknesses ( $\delta$ ) are in a similar range irrespective of the trip size used in the tests. When the boundary layer thickness ( $\delta'$ ) is estimated using the Reynolds stresses, a clear variation with tripping intensity is noticed. The magnitude of  $\delta'$  consistently increases with the increment of the trip size. While comparing the two definitions of the boundary layer thickness, the value of  $\delta$  and  $\delta'$  are found to be close to each other in case of fully developed flows (T1&T2 at  $H = 0.135$  m and T1&T3 at  $H = 0.17$  m) and a large deviation is observed in all under-tripped cases. The test case T1&T3 at  $H = 0.135$  m cannot be considered in this context since the flow does not retain a canonical behaviour and the value of  $\delta'$  is assumed to be equal to the flow depth. The present analysis demonstrates that a fully developed open channel flow can be stimulated experimentally by using the largest trip size that can retain the characteristics of canonical flow. For a lower trip size, the flow in the test section will be in the developing regime and the boundary layer thickness will not be in the same order as the flow depth. On the other hand, a larger trip generates excess turbulence which takes a longer streamwise length to get dissipated. However, the validity of these comments depends on two parameters: (1) flow development length and (2) aspect ratio. There must be a minimum flow development length available upstream of the test section to let the flow develop fully. Also, the aspect ratio of the flow should be high enough so that the effect of the side walls is negligible in the central region. Otherwise, if the channel is too narrow, the flow may deviate from the canonical behaviour due to secondary currents.

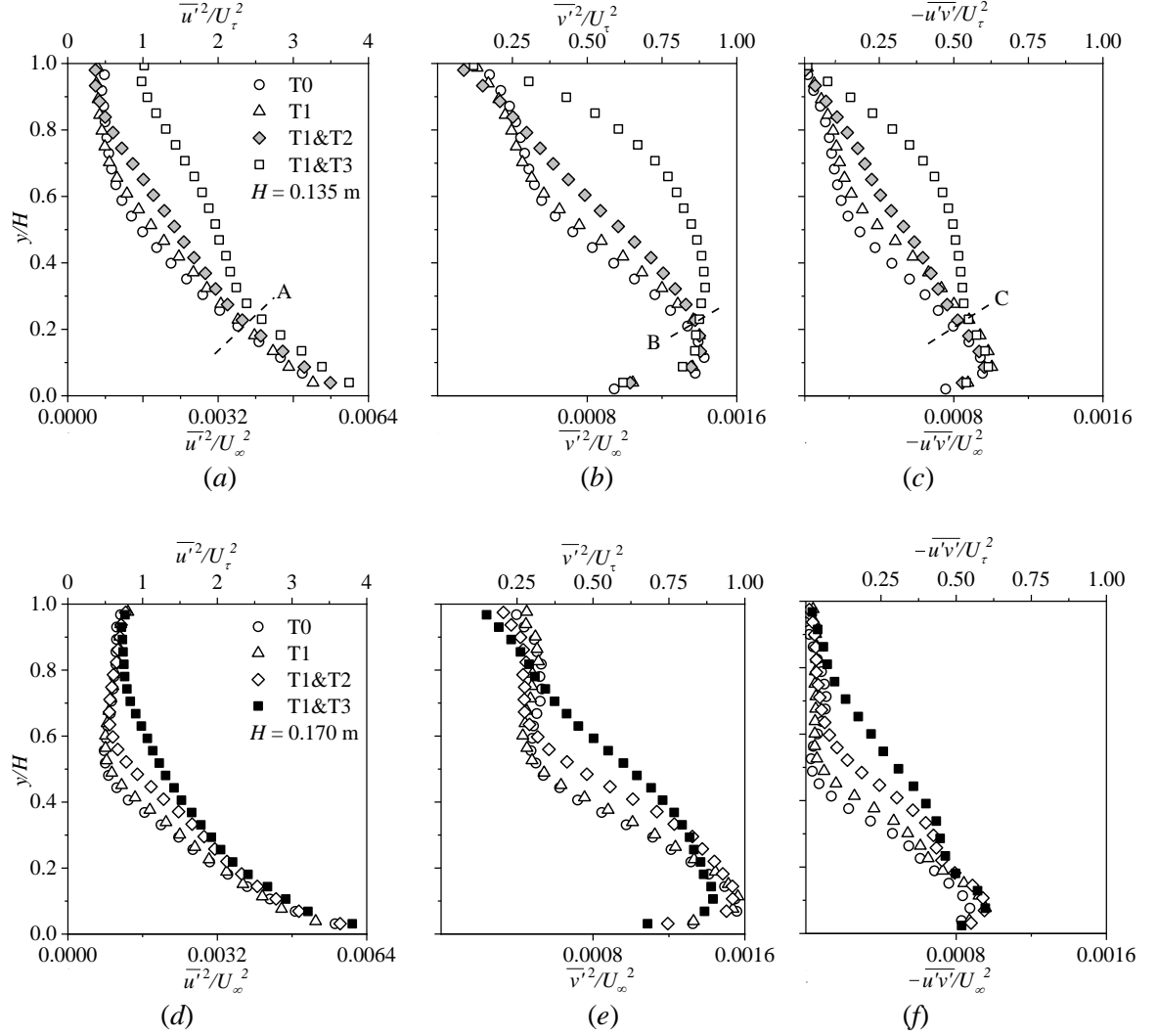


Figure 2.6. Distribution of normalized streamwise, bed-normal and shear stresses: (a,b,c)  $H = 0.135$  m and (d, e, f)  $H = 0.170$  m.

Velocity triple products retain the sign of velocity fluctuations and provide useful information related to coherent events. In [figure 2.7](#), the bed-normal distributions of third-order moments are presented in the form of skewness which is defined as  $S_u = \overline{(u'^3)} / (\overline{u'^2})^{3/2}$  and  $S_v = \overline{(v'^3)} / (\overline{v'^2})^{3/2}$ . The value of skewness of a normal distribution is zero due to symmetry in the distribution of the data points. Any value apart from zero reveals temporal asymmetry in the signal (Balachandar & Bhuiyan 2007), which can be directly correlated with the turbulence characteristics of the flow. In [figures 2.7\(a,e\)](#),  $S_u$  shifts from a positive to a negative value close to the bed, then continuously decreases in the upward direction away from the bed until it reaches a peak value. This represents a strong directional preference by the higher magnitude of the velocity fluctuations of extreme events, indicating a strong coherence in the flow structures. On the other hand, the  $S_v$  profiles ([figures 2.7b,f](#)) also show a similar trend although the skewness value is positive throughout the depth except near the bed. Above the point of maximum skewness, the skewness value reduces and finally reverts back to zero (or a very small value) at a specific height based on the tripping intensity (except the over-tripped case). These specific bed-normal coordinates above which the skewness

values are nearly constant can be correlated with the boundary layer thickness of the corresponding test cases and the value of  $\delta'$  so determined is consistent with the Reynolds stress profiles. Since, the distribution of  $u'$  is negatively skewed and of  $v'$  is positively skewed, the shear stress contribution by ejections is likely to be higher than the sweep events in the boundary layer except in the region very close to the bed and this is consistent with the canonical behaviour of a boundary layer flow. However, in the over-tripped case (T1&T3 at  $H = 0.135$  m),  $|S_u|$  is continuously increasing up to the free surface due to excess turbulence generated by the trip which can be distributed in the vertical direction and create free surface perturbations. This behaviour is consistent with what is seen in figure 2.6(a), where the Reynolds stress at the free surface is found to be much higher than in the other test cases.

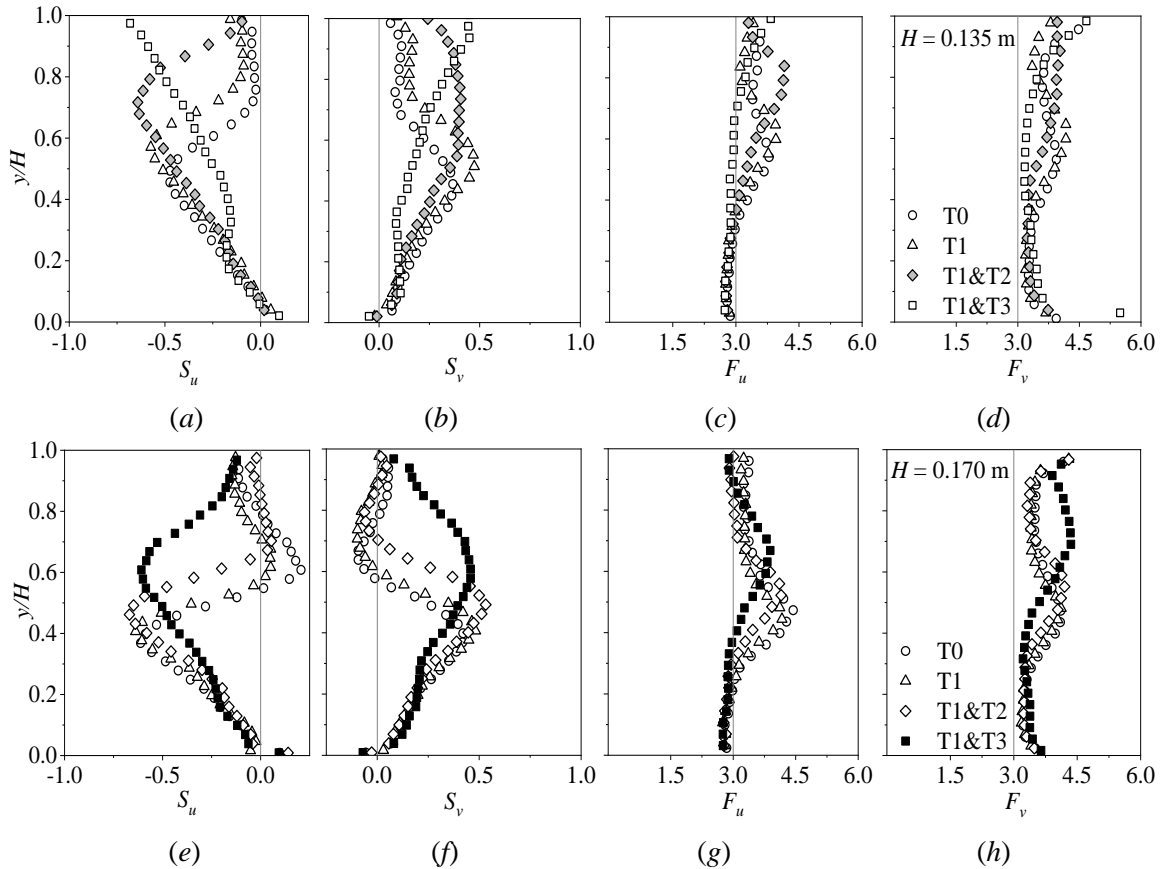


Figure 2.7. Distribution of normalized third-order and fourth-order moments: (a,b,c,d)  $H = 0.135$  m and (e,f,g,h)  $H = 0.170$  m.

Similarly, fourth-order turbulence statistics are illustrated in figures 2.7(c,d,g,h) in the form of flatness factors, defined as  $F_u=(u'^4)/(u'^2)^2$  and  $F_v=(v'^4)/(v'^2)^2$ . The flatness value of three corresponds to the normal distribution. Any value other than three describes the nature of intermittency in the flow (Balachandar & Bhuiyan 2007). The curves in figure 2.7(c,d,g,h) show that the flatness profiles have a peak in a similar location as the skewness profiles which implies that the quadrant events make strong intermittent contributions to the turbulence production (Grass 1971). Except for the over-tripped case,  $F_u$  has a value close to three near the bed, then gradually increases to the peak value and returns to three at the water surface. However, in the over-tripped case (T1&T3 at  $H = 0.135$  m),  $F_u$  and  $F_v$  are close to three throughout the depth except near the free surface. The magnitude of  $F_v$ , even in the fully developed state, is higher than three near the free surface. This is likely because the momentum transfer can only occur in the downward direction due to the restriction imposed by the free surface.

To check the self-similarity of the fully developed flow, the bed-normal distribution of the mean and turbulent quantities of test cases T1&T2 at  $H = 0.135$  m and T1&T3 at  $H = 0.170$  m are compared in figure 2.8 along with the velocity data of previous research (see table 2.4 for details). For the present experimental data,  $\delta'$  is used as the scaling factor of the  $y$  coordinates as it provides an accurate estimation of boundary layer thickness. In each of the graphs, the fully developed profiles collapse onto each other and show good agreement with the data sets of previous research, confirming the validity of the current definition of boundary layer thickness based on the distributions of Reynolds stresses. This implies that identification of the fully developed flow in the current research is accurate and  $\delta'$  can be used as the proper length scale and a viable parameter for defining boundary layer thickness.

Previous Research	Symbols	Type of study	$Re_{\delta'}$	$Re_{\theta}$
Present (T1&T2 at $H = 0.135$ m)	◇	OCF	34 600	3790
Present (T1&T3 at $H = 0.170$ m)	■	OCF	33 200	3486
Nakagawa and Nezu (1977)	+	OCF	10 900	
Simpson <i>et al.</i> (1981)	△	TBL	19 088	
Spalart (1988)	▽	TBL		1410
Tachie <i>et al.</i> (2003)	◁	OCF	54 200	2400
Balachandar and Patel (2005)	▷	OCF	110 000	
Flack <i>et al.</i> (2005)	◊	CF	100 000	10 220
Balachandar and Bhuiyan (2007)	◊	OCF	51 000	
Roussinova <i>et al.</i> (2008)	☆	OCF	30 500	4824
Afzal <i>et al.</i> (2009)	✱	OCF	49 200	3540

Table 2.4. The details of the previous studies used to check the self-similarity of the fully developed state (OCF: Open channel flow, CF: Channel flow, TBL: Turbulent boundary layer).

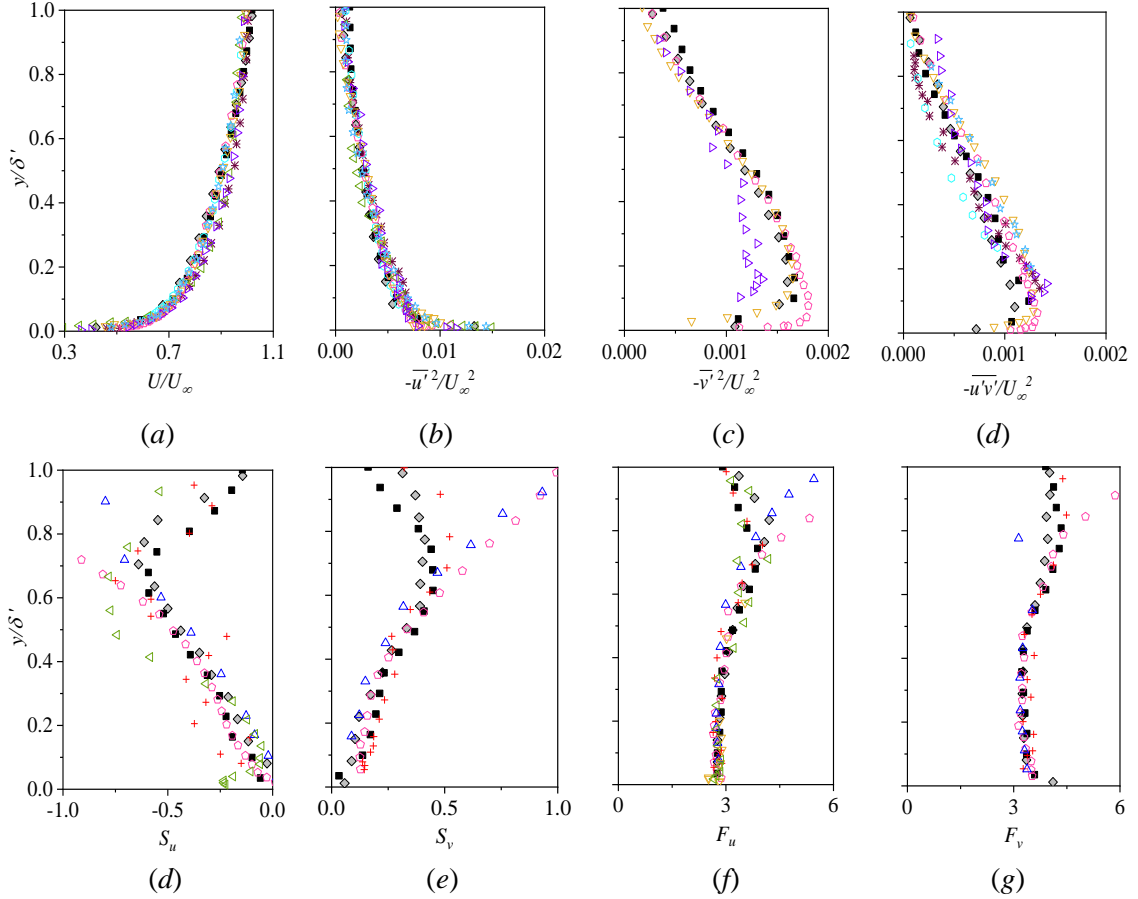


Figure 2.8. Comparison of fully developed profiles with previous studies: (a) Mean streamwise velocity, (b,c,d) Reynolds stresses, (e,f,g,h) Third and fourth-order moments.

## 2.6. Uniform momentum zones

In the previous sections, the trip size was varied to accurately stimulate the flow to be in a fully developed state, the evidence of which is provided by the distributions of Reynolds stresses and higher-order moments. Once the fully developed state is ensured, different aspects of the state of flow can be characterized using uniform momentum zone (UMZ) analysis. In fully developed open channel flow, the boundary layer thickness is nearly equal to the flow depth, which causes a restriction in a transfer of turbulence and momentum between the outer flow and the boundary layer since the free stream region is theoretically not present. This may cause an internal heterogeneity in the flow characteristics and affect the hierarchical pattern of the energy distribution. This flow physics is depicted by identifying and characterising the UMZs of the streamwise velocities in the fully developed state (i.e., test case T1&T3 at  $H = 0.170$  m depth) and these flow characteristics are compared with that of the developing flow (test case T0 at  $H = 0.170$  m depth). The test case T0 is chosen as the developing flow since this is the closest representation of a wind tunnel boundary layer among four test cases. The boundary layer thickness in case T0 is nearly half of the flow depth, enabling a momentum exchange between the boundary layer and free stream without any large influence of the free surface. This comparison demonstrates the effect of the free surface on the temporal variation of boundary layer flow variables and quadrant events in fully developed



open channel flow. One important thing to consider here is that the boundary layer thickness in the fully developed state is ideally constant whereas it is varying with the streamwise position in case of a developing flow. However, the length of the measurement section is small enough to cause any notable variation in the boundary layer thickness to occur within the FOV. Therefore, this comparison can be consistently carried out without any loss of generality.

In incompressible flows, UMZs can be simply defined as the zones of nearly similar streamwise velocities (Adrian *et al.* 2000). The streamwise momentum is nearly constant within such a zone and the velocity variation between adjacent zones is higher than the velocity fluctuation within a zone. As suggested by de Silva *et al.* (2016), these zones of uniform momentum are identified by the peaks in the PDF generated by the instantaneous streamwise vectors below the turbulent/non-turbulent interface (TNTI). The details of the detection methodology for determining TNTI position and the UMZs are provided in the following sections.

### 2.6.1. Detection of turbulent/non-turbulent interface

The turbulent/non-turbulent interface is a thin zone that separates the region of significant turbulence from the region of negligible turbulence. Detecting the location of the TNTI is essential to eliminate the irrotational non-turbulent region from the momentum zone analysis. UMZs are identified by the local maxima in the PDF of the instantaneous streamwise velocities. If the velocity values in the non-turbulent zone are not removed, there is a possibility of having a large outer peak in the PDF which may overshadow the smaller peaks inside the turbulent domain. These peaks correspond to the region with higher momentum, but with insignificant contribution to turbulence generation (de Silva *et al.* 2016).

The detection criteria for the TNTI have been an issue of debate among researchers for years. One of the well-established methods of identifying the TNTI is to consider the vorticity distribution and this method is widely used in jet studies. However, it is more difficult to implement this criterion in boundary layer type flows because of the noisy free stream (Laskari *et al.* 2018). The method of local instantaneous kinetic energy deficit as described in Chauhan *et al.* (2014a,b) has been suggested to eliminate any effect of external perturbations. However, this method was tested and found to be well-suited for wind-tunnel type turbulent boundary layer flows where a significant domain of free stream flow is present. In open channel flows, the influence of free surface must be taken into consideration, especially in the case of fully developed state where the edge of the boundary layer is very close to the free surface. Therefore, we propose a modified form of the equation suggested by Chauhan *et al.* (2014a,b) where the wall-normal free stream velocity ( $V_\infty$ ) is also taken into consideration along with streamwise velocity ( $U_\infty$ ) for better accuracy. Here  $U_\infty$  and  $V_\infty$  are taken as the maximum velocity near the free surface to maintain consistency in the fully developed flow where a free stream flow is theoretically not present. The kinetic energy deficit ( $K$ ) at each point of the flow domain is calculated with respect to a reference frame that is moving with mean free stream velocity ( $U_\infty, V_\infty$ ). For each point on the grid, the average energy deficit over a  $3 \times 3$  window (all surrounding points) is computed by modifying the equation of Chauhan *et al.* (2014a,b) as:

$$K = 100 \times \frac{1}{9(U_\infty^2 + V_\infty^2)} \sum_{m,n=-1}^1 [(U_{m,n} - U_\infty)^2 + (V_{m,n} - V_\infty)^2] \quad (2.6)$$

Once the kinetic energy deficit is calculated throughout the flow domain, a threshold value ( $K_{th}$ ) is required to demarcate between the turbulent and the non-turbulent flow. A domain inside the FOV corresponds to the non-turbulent zone if  $K$  is lower than the threshold value and to the zone of significant turbulence if  $K$  is higher. Therefore, a variable ( $K_b$ ) is defined in such a way that it is zero in the turbulent zone and one in the non-turbulent zone. A contour algorithm is employed to estimate the  $K_b = 0.5$  contour line which represents the TNTI location. The wall-normal coordinates of the local TNTI positions are extracted from all instances and used to calculate the mean  $Y_{TNTI}$  and standard deviation ( $\sigma$ ). Chauhan *et al.* (2014b) initially defined the magnitude of  $K_{th}$  to be equal to the free stream turbulent intensity and then increased by a small amount to match  $Y_{TNTI} + 3\sigma \approx \delta$ , since they assumed a Gaussian distribution with a 95% confidence interval. Laskari *et al.* (2018) reported setting  $K_{th}$  in such a way so that the intermittency profile is constant above  $\delta$  and  $Y_{TNTI} + 3\sigma < 1.4\delta$ . A similar approach is adapted in the present research where  $Y_{TNTI}$  is calculated over a range of threshold values ( $0.2 \leq K_{th} \leq 5.0$ ). The final value of  $K_{th}$  is determined as 0.9 for which  $Y_{TNTI} + 3\sigma \leq \delta'$  in the fully developed test cases. In figure 2.9, the magnitudes of  $Y_{TNTI}$  are plotted against the corresponding threshold values for all test cases. Interestingly, all the profiles collapse onto each other when  $K_{th}$  is higher than 0.9 but deviate significantly for a threshold value lower than 0.9. Therefore, this value is likely to provide an optimum estimation of  $K_{th}$  which differentiates two different types of attributes in the flow field in terms of TNTI positions. If the value of  $K_{th}$  was chosen to be much smaller (i.e., of the order of free surface turbulence intensity), the TNTI location will be highly sensitive to the value of  $K_{th}$  since the variation of  $K$  is small near the free surface because the mean velocity components are close to  $U_\infty$  and  $V_\infty$ . Consequently, any external noise and free surface perturbation will have a strong influence on the location of the TNTI. On the other hand, if  $K_{th}$  is set to be a much larger value, the TNTI will be at a lower position and important information on turbulence and momentum transfer will be lost in the outer domain. Furthermore,

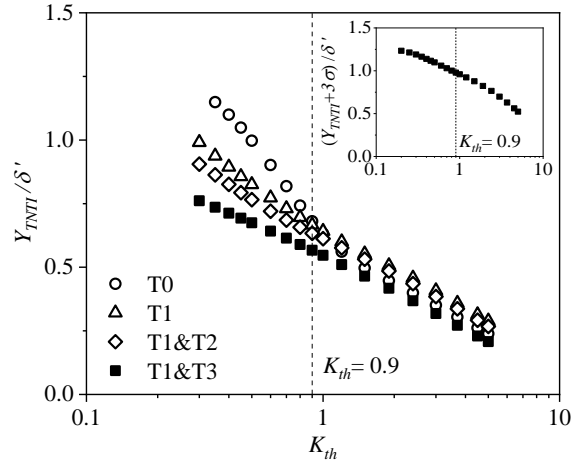


Figure 2.9. Normalized mean TNTI location ( $Y_{TNTI}$ ) for all test cases at  $H = 0.170$  m and the distribution of  $Y_{TNTI} + 3\sigma$  for the fully developed state T1&T3 (inset) corresponding to the value of  $K_{th}$  between 0.3 to 5.0.

the effect of a smaller variation (up to 20%) in the value of  $K_{th}$  was tested by carrying out the momentum zone analysis for five values of  $K_{th}$  (0.7, 0.8, 0.9, 1.0, 1.1) and the number of momentum zones ( $N_{UMZ}$ ) is found to be similar in each case (see appendix A). Therefore, a small variation in the value of  $K_{th}$  has only a minor influence on the UMZ analysis and cannot alter the findings that

are achieved by keeping a constant value of  $K_{th}$  as 0.9 for all test cases. This value is used in all further analyses to maintain consistency.

### 2.6.2. Detection of uniform momentum zones

The UMZs are detected by the PDF of instantaneous streamwise velocity vectors that lies inside the turbulent region i.e., the region in the FOV where  $K$  is greater than  $K_{th}$ . The probability densities are determined by dividing the velocity data of each instance ( $U$ ) into small bins, and the bars corresponding to each bin in the velocity histogram (figure 2.10a) represents the probability that the velocity lies in that specific bin. The peak probability density values (as shown by ‘▼’ in figure 2.10a) in the histogram correspond to each of the momentum zones and the value of  $U/U_\infty$  corresponding to each peak is the modal velocity (MV) of that zone. Each peak is confined by two local minima and these minima values are used as the contour levels of the momentum zones. These contour lines demarcate the area of each momentum zone and are presented in figure 2.10b. The zones are ranked ( $R_i$ ) based on their bed-normal position, i.e., the UMZ adjacent to the TNTI is ranked one and adjacent to the bed is ranked the highest. The value of highest rank depends on the number of UMZs present in that specific instance. The average bed-normal position (i.e., the adjacent upper contour level) and the thickness of momentum zones is represented by  $Y_{UMZ}|_{R_i}$  and  $t_{UMZ}|_{R_i}$  where  $i$  is the rank of the corresponding momentum zone.

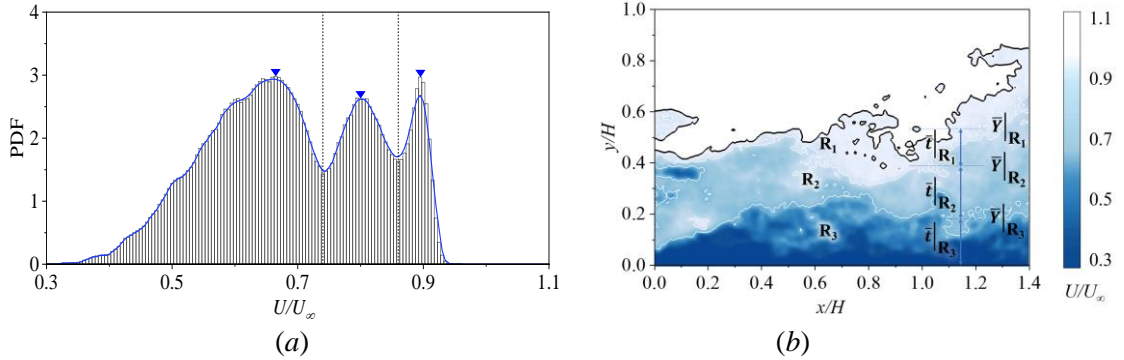


Figure 2.10. (a) PDF of streamwise velocities below TNTI for a single instance. The inverted triangles ‘▼’ indicates the modal velocities and the dashed lines differentiate the UMZs. The continuous blue line represents the curve fitted over the probability data in order to find the modal velocities. (b) corresponding contour plot of the UMZs. The average bed-normal position (i.e., the adjacent upper contour level) and the thickness of momentum zones is presented by  $Y_{UMZ}|_{R_i}$  and  $t_{UMZ}|_{R_i}$  where  $i$  is the rank of the corresponding momentum zone.

The instances with a similar number of peaks in the PDF (i.e., a similar number of UMZs) are likely to have a similar type of coherent event. Laskari *et al.* (2018) correlated the large scale Q2 and Q4 events with the instances of higher and lower than average number of momentum zones, respectively. The variation in flow characteristics with the change in number of momentum zones ( $N_{UMZ}$ ) is shown in the following sections by conditional averaging of flow variables of the instances that belong to a similar number of momentum zones. Therefore, some important considerations must be taken in order to ensure a consistent identification of the magnitude of  $N_{UMZ}$ . Firstly, an optimum selection of the bin size is mandatory in this context since the number of momentum zones may vary significantly with the bin size. Similar to Laskari *et al.* (2018), a bin

size of  $0.5U_\tau$  is used here for a range of velocities,  $U/U_\infty \in [0, 1]$ . However, a non-zero probability density is found only in the range,  $U/U_\infty \in [0.25, 1]$  since the flow velocities very close to the bed can not be captured due to spatial resolution of the data acquisition tool. A smaller and a larger bin size ( $0.25U_\tau$  and  $0.75U_\tau$ ) were also employed for a similar UMZ analysis to study the influence of bin size on the momentum zone analysis. A consistent output is attained for these two bin sizes (see [Appendix B](#)) and the current selection of the bin size is not likely to alter the findings of this paper.

The method of identifying UMZ contour levels is also dependent on the length of the FOV ( $\mathcal{L}$ ) and the number of vectors taken into consideration. Adrian *et al.* (2000) and de Silva *et al.* (2016) have chosen a streamwise length of  $\delta$ , which corresponds to a viscous wall unit  $\mathcal{L}^+ = \mathcal{L}U_\tau/\nu = 2000$ . Laskari *et al.* (2018) have also used a similar  $\mathcal{L}^+$  instead of using the whole FOV for a better comparability. In the present work, the streamwise extent of the FOV is approximately 250 mm ( $\sim 1.4H$  or  $1.7\delta'$ ) that corresponds to 2250 viscous wall units and roughly 25 000 vectors are present in every snapshot with a spatial resolution of  $\sim 1.3$  mm. Since the value of  $\mathcal{L}^+$  corresponding to the whole FOV is in a similar range as mentioned in the previous research, we have chosen to use the whole FOV at highest data resolution for maximum utilization of our data. Further, the momentum zone analysis is also carried out varying the length of the FOV in the range of  $1250 \leq \mathcal{L}^+ \leq 2250$  at similar data resolution which reduces the number of vectors present in the FOV keeping the vector density the same. A minor variation in the number of momentum zones is noticed with the change in streamwise extent of the FOV, but this has a negligible impact on the qualitative trend of the dataset (see [Appendix A](#)).

Once the PDFs of the velocity data are generated, a peak-detection algorithm is required to identify the modal velocities and eliminate other minor peaks. A moving-average filter and a weighted linear least square based local regression algorithm is used in order to fit a smooth curve (shown by the blue line in [figure 2.10a](#)) over the data points ( $b_i, P_i$ ) where  $b_i$  is the  $i$ -th bin and  $P_i$  is the corresponding probability density. As suggested by Laskari *et al.* (2018) and Chen *et al.* (2020), the algorithm involves filtering using three important criteria:  $F_d$  (allowed distance between two peaks),  $F_h$  (minimum of the height of each peak) and  $F_p$  (prominence of each peak based on the relative height to its neighbouring bins). The peaks in the PDF diagram are only recognized if  $F_d > 5$  bins ( $\sim 10\%$  of  $U_\infty$ ),  $F_h > 1$  and  $F_p > 25\%$ . The validity of this algorithm is also taken into consideration while adjusting the bin size and the value of these thresholding parameters are finely adjusted to get the best output. This process merges the peaks in close proximity and removes the peaks whose relative probability density is not significantly higher than the neighbouring bins. The peaks corresponding to very small probability density are also eliminated which also discard any minor peaks generated artificially by the curve fitting algorithm. The PDF of  $N_{UMZ}$  is estimated by identifying the peaks using this algorithm and presented in [figure 2.11\(a\)](#). A maximum of 6 peaks are identified over 4000 instances. The instances corresponding to  $N_{UMZ}$  between 2 to 4 are considered for the UMZ analysis based on a cut-off of probability density value of 0.1 (10% of overall dataset) since the conditional averaging over a small data set will not provide a consistent comparison of the flow characteristics. The accuracy of the peak-detection algorithm is tested by estimating the mean contour levels corresponding to the average bed-normal position of UMZs ( $Y_{UMZ}|_{i,j}$ ) and the modal velocities ( $Y_{MV}|_{i,j}$ ), where subscripts  $i$  and  $j$  indicate the value of  $N_{UMZ}$  and rank, respectively. The distribution of  $Y_{UMZ}|_{i,j}$  and  $Y_{MV}|_{i,j}$  (shown by ‘●’ and ‘△’, respectively) are presented in [figure 2.11](#) for the fully developed flow (test case T1&T3 at  $H = 0.17$  m). The circles at the highest bed-normal positions indicate the position of the TNTI of the

corresponding column. The space between two circles or a circle and the bed in each column represents the average thickness of each of the momentum zones. The average momentum zone thickness gradually decreases with the events of larger number of peaks which helps in accommodating more layers of UMZs. In each case, the average wall-normal positions of the modal velocity contour levels lie within the corresponding momentum zones showing a consistent behaviour and proving validity of the peak-detection algorithm.

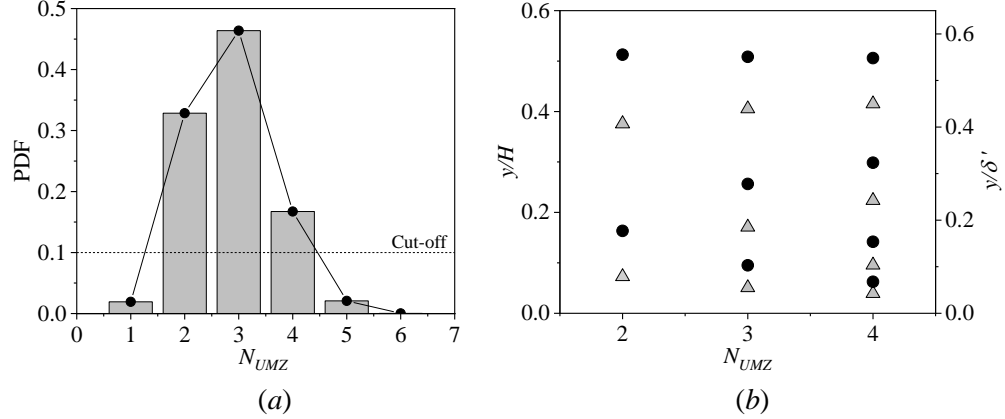


Figure 2.11. (a) PDF of  $N_{UMZ}$  corresponding to bin size  $0.5U_\tau$ ; (b) Bed-normal distribution of  $Y_{UMZ}|_{i,j}$  and  $Y_{MV}|_{i,j}$  (shown by ‘●’ and ‘△’, respectively) for the fully developed flow (test case T1&T3 at  $H = 0.170$  m). The subscripts  $i$  and  $j$  indicate the value of  $N_{UMZ}$  and rank, respectively.

### 2.6.3. Characterization of fully developed flow

In this section, flow properties of the fully developed open channel flow (test case T1&T3 at  $H = 0.17$  m) is characterised by analyzing different attributes of the momentum zones. As mentioned earlier, the velocity data of each instance are used to generate the PDFs and the number of peaks in the PDF indicates the number of momentum zones present at that particular instance. The momentum zones at each instance are ranked based on their bed-normal position. For example, if the PDF of velocity data of a specific instance corresponds to  $N_{UMZ} = 3$ , there will be three momentum zones which are ranked one to three. The rank is one for the zone at the highest bed-normal position and three for the zone closest to the bed. The instances with similar number of UMZs are grouped together to see an overall characteristic of these events. The normalized mean modal velocities ( $U_{MV}|_{R_i}$ ), UMZ contour levels ( $Y_{UMZ}|_{R_i}$ ) and momentum zone thickness ( $t_{UMZ}|_{R_i}$ ) of each group are estimated by the conditional averaging of the data corresponding to their ranks and presented in figure 2.12(a,b,c). The data corresponding to a specific value of  $N_{UMZ}$  are represented by the same colour and the data of the same rank are shown by similar markers. Each of the markers indicate the mean values of modal velocities and the bar represents the distribution around the mean value. The length of the bar is estimated by the magnitude of the 25<sup>th</sup> and 75<sup>th</sup> percentile of the distribution, which shows the extent of centered 50% of the data. The PDFs in figure 2.12(c,d,e) represents one such example of the distribution of  $U_{MV}$ ,  $Y_{UMZ}$  and  $t_{UMZ}$  for  $R_1$  at  $N_{UMZ} = 3$  and the corresponding 25<sup>th</sup> and 75<sup>th</sup> percentile positions are marked with the dashed lines.

The magnitudes of  $U_{MV}$  and  $Y_{UMZ}$  for  $R_1$  are nearly constant (figure 2.12a,b) although the distribution around the centered value gradually reduces when the number of momentum zones increases. There is only the possibility of less variation since the thickness of the momentum zones for  $R_1$  significantly reduces (figure 2.12c) with the increment of  $N_{UMZ}$  to accommodate the additional zones. On the other hand, the magnitudes of  $U_{MV}$  and  $Y_{UMZ}$  for  $R_2$  and  $R_3$  increase significantly with the increment of  $N_{UMZ}$  keeping the thickness similar which indicates the zones corresponding to  $R_2$  and  $R_3$  move upwards and this causes shrinking of the outer-most momentum zone. The difference in magnitudes of the adjacent  $U_{MV}$  and  $Y_{UMZ}$  values at a specific  $N_{UMZ}$  also reduces to accommodate this new zone. This indicates that the new zone appears near the bed which is consistent with the observations of Laskari *et al.* (2018) and Chen *et al.* (2020). Since the fluid parcels near the bed are lifted up towards the outer flow, they gain higher momentum in this process. This upward movement of slow-moving fluid towards the zone of higher momentum reveals the existence of large-scale Q2 events near the bed. On the contrary, if we consider a

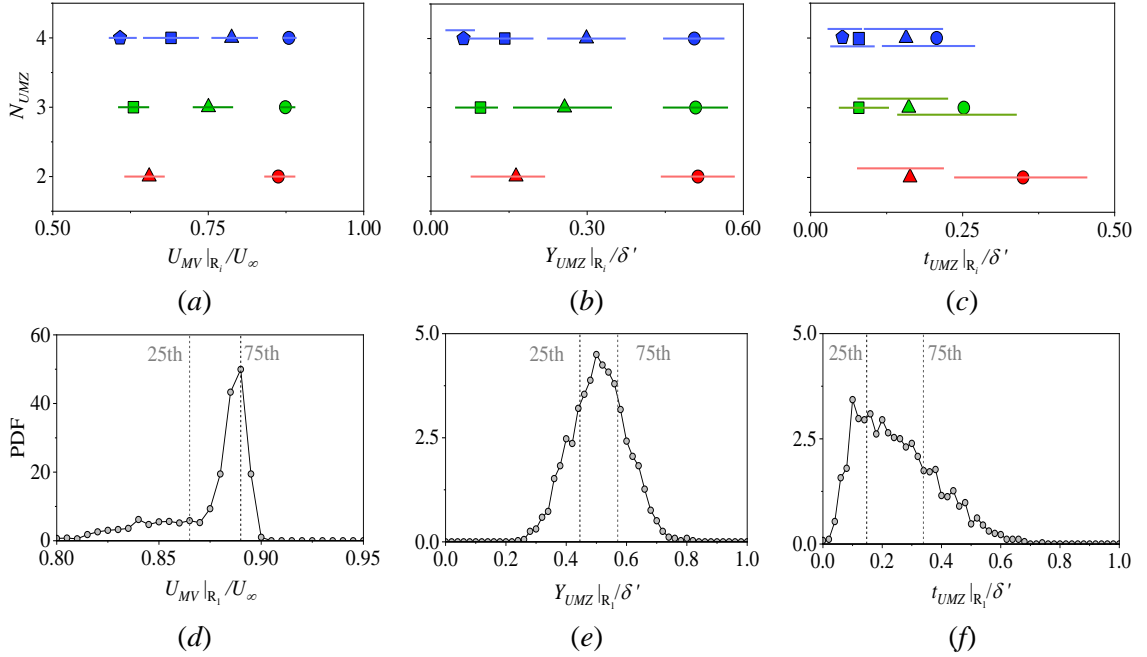


Figure 2.12. Conditional averaging of the data corresponding to a specific value of  $N_{UMZ}$  based on their rank ( $R_i$ ) of (a) modal velocities ( $U_{MV}|_{R_i}$ ), (b) bed-normal position of the mean contour level of UMZs ( $Y_{UMZ}|_{R_i}$ ) and (c) the corresponding thickness of UMZs ( $t_{UMZ}|_{R_i}$ ). Same markers are used for the same rank and same colors for a given  $N_{UMZ}$ . The markers represent the centered values and the bars show the distribution around it based on the magnitude of 25<sup>th</sup> and 75<sup>th</sup> percentile. The distributions for  $N_{UMZ} = 3$  are presented for (d)  $U_{MV}|_{R_1}$ , (e)  $Y_{UMZ}|_{R_1}$  and (f)  $t_{UMZ}|_{R_1}$ . The magnitudes of 25<sup>th</sup> and 75<sup>th</sup> percentiles are shown by the dashed lines.

transition from higher  $N_{UMZ}$  to a lower value, the existence of large-scale Q4 events can be found. When a momentum zone disappears, the modal velocity of a similar ranked UMZ reduces and it moves towards the bed which indicates the downward motion of higher momentum fluid parcels or large-scale sweeping motion near the bed. Therefore, instances with higher number of momentum zones are likely to be highly influenced by large-scale Q2 events, whereas large-scale

Q4 events are dominant in the case of smaller number of momentum zones. Interestingly, these large-scale fluid motions can be found very close to the bed, possibly within the logarithmic layer and the flow in the outer layer shows an opposing characteristic. For example, the magnitudes of  $U_{MV}$  and  $Y_{UMZ}$  for  $R_i > 1$  reduce significantly with an increment in  $N_{UMZ}$ , whereas it is nearly constant for  $R_i = 1$ . Similarly, the thickness of momentum zones for  $R_i = 1$  reduces sharply when a new zone appears but it is nearly constant for higher ranked UMZs. This suggests a variation in flow characteristics between the flow close to the wall and flow near the TNTI which is further investigated in the following sections.

#### 2.6.4. Quadrant events

Herein, the focus of the quadrant analysis is to correlate the momentum zone analysis with the different flow dynamics of the ejections and sweeps, and the traditional quadrant analysis procedure of Lu & Willmarth (1973) is followed. Reynolds stresses at each point are calculated and categorized to the corresponding quadrants by the sign of  $u'$  and  $v'$ . The second quadrant (Q2) corresponds to sweeps while the fourth (Q4) relates to ejections. Shear stress contribution from each quadrant is calculated from

$$\overline{u'v'_{Qi}} = \lim_{T \rightarrow \infty} \int_0^T u'(t)v'(t)dt \quad \text{for } i = 1 \text{ to } 4. \quad (2.7)$$

The hole size is taken as zero in the present analysis so as to include the contributions from all events and not just the extreme events. In order to determine the dominant quadrant events with a variation in  $N_{UMZ}$ , the ratio of shear stress contributions from Q2 and Q4 ( $R_{Q2/Q4} = \overline{u'v'_{Q2}} / \overline{u'v'_{Q4}}$ ) is estimated by conditional averaging of the instances which belong to a specific value of  $N_{UMZ}$  and presented in figure 2.13 for both the developed (T1&T3 at  $H = 0.17$  m) and the developing flow (T0 at  $H = 0.17$  m).

Firstly, the PDFs of  $N_{UMZ}$  for both cases are presented in figure 2.13(a) to provide a comparison between probability of occurrence of the instances corresponding to different number of peaks in the PDF. A cut-off probability density value of 0.1 is implemented here and the instances with  $N_{UMZ} = 2, 3$  and 4 are taken into consideration for further analyses. Interestingly, a similar number of instances (out of total 4000 instances) corresponding to a specific value of  $N_{UMZ}$  are found for both the developed and developing flow. As mentioned in the previous section, the instances with a similar number of momentum zones are grouped together and the magnitudes of  $\overline{u'v'_{Q2}}$  and  $\overline{u'v'_{Q4}}$  are estimated by conditional averaging of the shear stress contribution to Q2 and Q4 events for each of these groups. The ratio of  $\overline{u'v'_{Q2}}$  and  $\overline{u'v'_{Q4}}$  provides an indication of the dominant event, i.e., the maximum shear stress is generated by the ejection events if  $R_{Q2/Q4} > 1$  and by the sweep events when  $R_{Q2/Q4} < 1$ . The bed-normal distribution of  $R_{Q2/Q4}$  is presented for both the fully developed flow (figure 2.13b) and the developing flow (figure 2.13c). The fully developed flow shows a vertical variability of the coherent events. For  $N_{UMZ} = 2$ , the magnitude of  $R_{Q2/Q4}$  is the highest at  $y/\delta' \approx 0.6$  and indicates strong dominance of ejections over sweeps at this depth. Below this depth, the value of  $R_{Q2/Q4}$  gradually decreases and becomes nearly equal to one near the bed ( $y/\delta' < 0.3$ ). However, in the case of  $N_{UMZ} = 4$ , the bed-normal position of this peak value of  $R_{Q2/Q4}$  moves towards the bed ( $y/\delta' \approx 0.2$ ) and the value of  $R_{Q2/Q4}$  is nearly equal to one at  $y/\delta' > 0.35$ . The distribution of  $N_{UMZ} =$

3 provides an intermediate characteristic exhibiting two peaks at  $y/\delta' \approx 0.6$  and  $y/\delta' \approx 0.2$ . In the case of developing flow, the maximum value of  $R_{Q2/Q4}$ , irrespective of number of momentum zones, is observed near  $y/\delta' \approx 0.75$  which is much closer to the boundary layer thickness in comparison to the fully developed flow and the distributions of  $N_{UMZ} = 2, 3$  and  $4$  appears to be similar in pattern. Some similarity with the developed flow can be seen since the magnitude of  $R_{Q2/Q4}$  gradually decreases in the range  $0.45 < y/\delta' < 1.0$  and increases in the lower flow domain with the increment of  $N_{UMZ}$ . However, the vertical shifting of the peak value of  $R_{Q2/Q4}$  is not present in the developing flow. This comparison of vertical variability can be more prominently seen when the bin size is reduced to  $0.25U_\tau$  and a higher range of values of  $N_{UMZ}$  is available (see Appendix B). However, we choose to present the results corresponding to the bin size  $0.5U_\tau$  since a higher number of instances are present corresponding to each value of  $N_{UMZ}$  making this analysis more reliable. Also, the peak-detection algorithm may provide some inconsistency in determining the number of peaks for some specific instances for a smaller bin size, although it is unlikely to alter the overall conclusion.

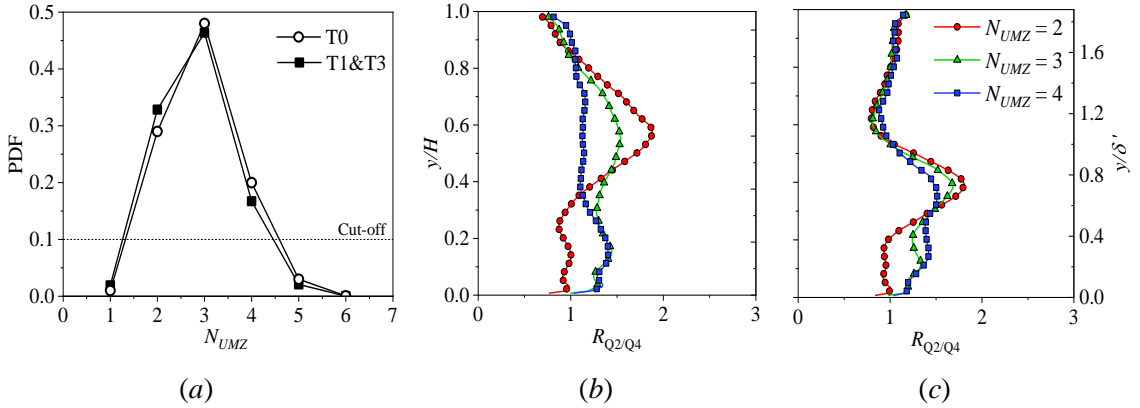


Figure 2.13. (a) PDF of  $N_{UMZ}$  corresponding to bin size  $0.5U_\tau$  for the developing flow (T0 at  $H = 0.170$  m) and the fully developed flow (T1&T3 at  $H = 0.170$  m). Conditional averaging of ratio of shear stress contribution from Q2 and Q4 events based on the value of  $N_{UMZ}$  for (b) the fully developed flow (T1&T3 at  $H = 0.170$  m) and (c) the developing flow (T0 at  $H = 0.170$  m).

### 2.6.5. Large-scale fluid motions

The quadrant analysis shows a significant vertical variation in the coherent events with the change in number of momentum zones in case of fully developed flow. The shear stress contribution to the ejections and sweeps are determined based on the instantaneous velocity fluctuations at each point. In the present section, the large-scale fluid motions are detected based on the distribution of instantaneous velocity deficit which is estimated by subtracting the double-averaged profile from the spatially averaged velocity distribution of each instance. The flow near the bed can produce large-scale Q2 or Q4 events based on the signs of the velocity deficits. The velocity deficits are conditionally averaged over all instances that belong to a specific value of  $N_{UMZ}$  and the distribution of these normalized streamwise and bed-normal velocity deficits ( $U_{def}/U_\infty$  and  $V_{def}/U_\infty$ ) are presented for the fully developed flow in figure 2.14(a,b) and the developing flow in figure 2.14(c,d). For  $N_{UMZ} = 2$  (i.e., for a lower number of momentum zones), the streamwise



velocity deficit is positive and the bed-normal velocity deficit is negative at  $y/\delta' \leq 0.4$ , which indicates the existence of large-scale Q4 events. For a higher number of momentum zones,  $U_{def}$  is negative and  $V_{def}$  is positive the presence of large-scale Q2 events near the bed. Near the bed, this variation in large-scale fluid motion with the change in number of momentum zones is present in both the fully developed and the developing flow. However, in the case of fully developed flow, an opposite nature of large-scale fluid motion is also observed in the boundary layer above  $y/\delta' \geq 0.4$ , i.e., large-scale Q4 events are present for higher number of momentum zones and large-scale Q2 events for lower number of momentum zones. This opposing characteristic in the outer layer is not prominent in the developing flow.

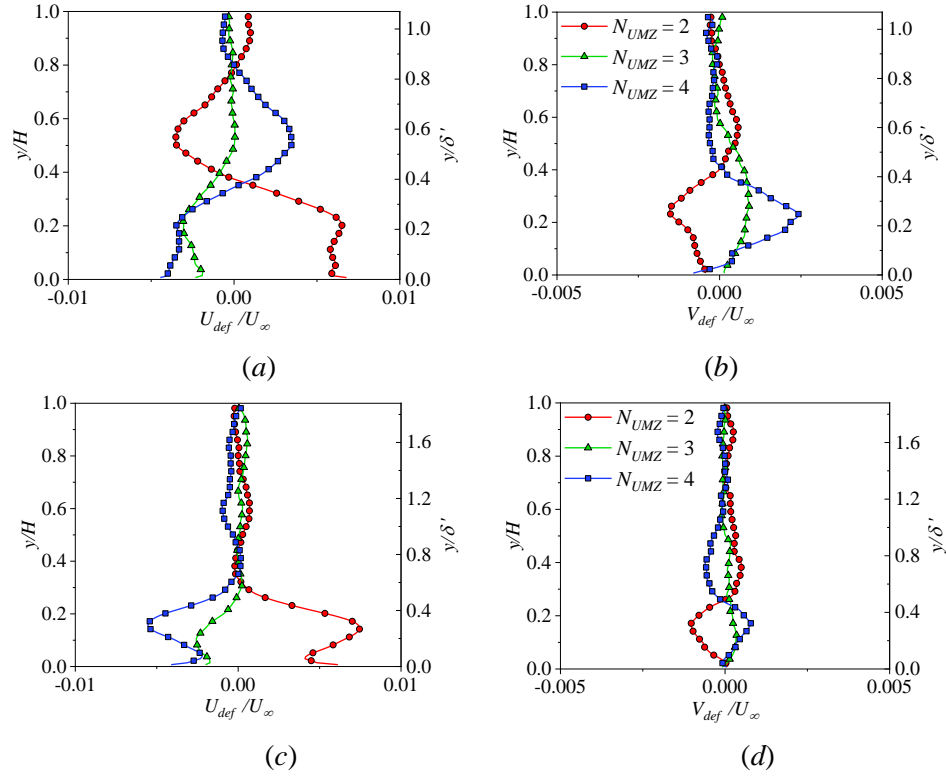


Figure 2.14. Conditional averaging of normalized streamwise and wall-normal velocity deficit based on the value of  $N_{UMZ}$  for (a,b) the fully developed flow (T1&T3 at  $H = 0.170$  m) and (c,d) the developing (T0 at  $H = 0.170$  m).

In open channel flow, the constraint imposed by the free surface always exists although its influence on the flow varies depending on the bed-normal position of the edge of the boundary layer. The magnitudes of the velocity deficits are nearly zero at  $y/\delta' \geq 0.3$  (figure 2.14c) in case of the distribution of streamwise velocity deficit for the developing flow, which is similar to what was found by Laskari *et al.* 2018. However, the bed-normal velocity deficit profiles corresponding to  $N_{UMZ} = 2$  and 4 change signs at a similar depth, which is likely caused by the vertical constraint generated by the free surface. In the fully developed state, the influence of this constraint is so high that it alters the distribution of both velocity deficit profiles. To understand the intricate details of the fluid motion and coherent events that cause vertical variability in open channel flow, the shear stress contribution to the quadrant events (pointwise) is correlated with the large-scale fluid

motions. In the present analysis, the instances are grouped based on the nature of large-scale fluid motion inside the logarithmic layer ( $y/\delta' \leq 0.2$ ). Depending on the signs of the integrals of the velocity deficits inside the logarithmic layer, the flow near the bed can be induced to large-scale Q2 events (denoted as  $E_1$ ) if  $\int_0^{0.2\delta'} U_{def} dy < 0$  and  $\int_0^{0.2\delta'} V_{def} dy > 0$ , whereas large-scale Q4 events ( $E_2$ ) occur when  $\int_0^{0.2\delta'} U_{def} dy > 0$  and  $\int_0^{0.2\delta'} V_{def} dy < 0$ . It is worth mentioning here that the method of identifying large-scale fluid motion is different from quadrant analysis where the signs of the velocity fluctuations are used to determine the Q2 and Q4 events at each point. Here, our focus is to demonstrate an overall sweeping or ejecting motion of fluid considering the whole area inside the FOV. Events  $E_1$  and  $E_2$  covers nearly 70% of the total instances in both the developing and developed flow. The average overall shear stress contribution of  $E_1$  and  $E_2$  to ejections and sweeps ( $-\overline{u'v'}_{Q2+Q4}|_{E_1+E_2} = -\overline{u'v'}_{Q2}|_{E_1} - \overline{u'v'}_{Q4}|_{E_1} - \overline{u'v'}_{Q2}|_{E_2} - \overline{u'v'}_{Q4}|_{E_2}$ ) are estimated considering all the instances that belong to either  $E_1$  or  $E_2$ . Since these two events do not have exactly the same number of instances, average shear stress contribution of  $E_1$  and  $E_2$  are calculated separately to maintain consistency and then added together. For example, if  $n_i$  number of instances are present for  $E_i$ , then  $-\overline{u'v'}_{Qj}|_{E_i}$  at each point can be calculated as  $\sum -u'v'_{Qj}|_{E_i} / n_i$  where  $j = 2$  or  $4$  depending on the quadrant and  $i = 1$  or  $2$  depending on the event type. This procedure differs from the method of estimation of shear stress contribution of Q2 and Q4 events by pointwise quadrant analysis, in which the total shear stress corresponding to each quadrant is divided by the total number of instances which indirectly consider their probability of occurrence to ensure that the total shear stress is equal to the sum of all four quadrant. In the present analysis, the total shear stress corresponding to either  $E_1$  or  $E_2$  is divided by the number of instances that belongs to each group since our objective is to see the overall flow characteristics of these specific events. Figure 2.15 shows that the bed-normal distribution of  $-\overline{u'v'}_{Q2+Q4}|_{E_1+E_2}$  is of the same order for the fully developed and the developing flow. In the following section, we have looked into the distribution of  $-\overline{u'v'}_{Q2}|_{E_1} - \overline{u'v'}_{Q4}|_{E_1} - \overline{u'v'}_{Q2}|_{E_2} - \overline{u'v'}_{Q4}|_{E_2}$  separately, which reveals the variation in shear stress distribution of  $E_1$  and  $E_2$  to different quadrants, although total shear generation is comparable.

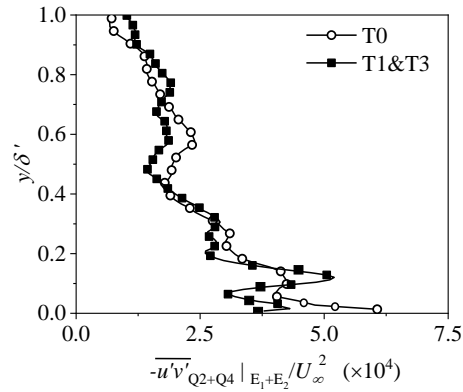


Figure 2.15. Bed-normal distribution of normalized total shear stress contribution by large-scale Q2 and Q4 events ( $-\overline{u'v'}_{Q2+Q4}|_{E_1+E_2}$ ) in the logarithmic layer for the fully developed flow (T1&T3 at  $H = 0.170$  m) and the developing flow (T0 at  $H = 0.170$  m).

Our focus is to study the overall flow characteristics of an event that belongs to either  $E_1$  or  $E_2$  and to demonstrate their heterogeneity in distribution towards different coherent events depending on the varied influence of the free surface. The contribution of  $E_1$  and  $E_2$  to ejections and sweeps (based on actual point-based quadrant analysis) can depict this variability in the distribution of shear stress in developing and fully developed open channel flows. Figure 2.16 presents the bed-normal distribution of  $-\overline{u'v'}_{Q2}|_{E_1}$ ,  $-\overline{u'v'}_{Q4}|_{E_1}$ ,  $-\overline{u'v'}_{Q2}|_{E_2}$  and  $-\overline{u'v'}_{Q4}|_{E_2}$  for test cases T0 and T1&T3 at  $H = 0.17$  m. These distributions show a contrast in the flow characteristics of a developing and a developed flow. For direct shear stress generation (contribution to Q2 by large-scale Q2 events,  $-\overline{u'v'}_{Q2}|_{E_1}$  and contribution to Q4 by large-scale Q4 events,  $-\overline{u'v'}_{Q4}|_{E_2}$ ) (figure 2.16a,d), ejections in fully developed flow are the major contributor in shear generation in the flow close to bed, whereas sweeps dominate in the case of developing flow. Also, a significant shear contribution is found to be restricted at the region adjacent to the bed (i.e.,  $y/\delta' \leq 0.3$  for  $-\overline{u'v'}_{Q2}|_{E_1}$  and  $y/\delta' \leq 0.4$  for  $-\overline{u'v'}_{Q4}|_{E_2}$ ) in the case of fully developed flow, whereas it is distributed over a larger depth in developing flow (i.e.,  $y/\delta' \leq 0.7$  for  $-\overline{u'v'}_{Q2}|_{E_1}$  and  $y/\delta' \leq 0.6$  for  $-\overline{u'v'}_{Q4}|_{E_2}$ ). This is likely because of the scale effect of the normalization which helps to depict the constraint provided by the free surface based on their relative location of the boundary layer thickness with respect to the total depth of flow. On the other hand, the cross shear generations (contribution to Q4 by large-scale Q2 events,  $-\overline{u'v'}_{Q4}|_{E_1}$  and contribution to Q2 by large-scale Q4 events,  $-\overline{u'v'}_{Q2}|_{E_2}$ ) (figure 2.16b,c) are likely to have the maximum shear generation away from the bed and thus control the majority of the quadrant events in the flow away from the wall. Interestingly, the bed-normal distributions of  $-\overline{u'v'}_{Q2}|_{E_2}$  are of the same order of magnitude in both developed and developing flow, indicating a similar contribution to ejections by  $E_2$  in the outer layer. It is to be noticed here that the ejected fluid parcels in the developing flow can move upward and reach the free stream flow through momentum exchange between the outer flow and the boundary layer. This is not possible in the fully developed flow state and the ejected fluid must be swept away through the surrounding fluid causing higher shear generation to sweeping events, the evidence of which can be found in the distribution of  $-\overline{u'v'}_{Q4}|_{E_1}$ . This shear stress component in fully developed flow is significantly higher than that of developing flow throughout the depth of flow (except very close to the bed) which illustrates the dissimilarities in the shear generation in the outer boundary layer of a developing and a developed open channel flow. It is worth mentioning here that this variation in the quadrant shear distribution is present although their overall contribution to shear generation is mostly similar throughout the depth (Figure 2.15). This depicts that the alteration and readjustment of inner flow properties occur in the boundary layer in an open channel based on the extremity of the influence of the free surface. The effect of this alteration may not be clearly visible in the time-averaged quantities such as distribution of mean velocity and shear stresses. However, it may have adverse effects and cause inaccuracy in fluid-structure interaction studies since the inner properties of the flow structures can vary significantly depending on the position of the edge of the boundary layer compared to the total depth of flow.

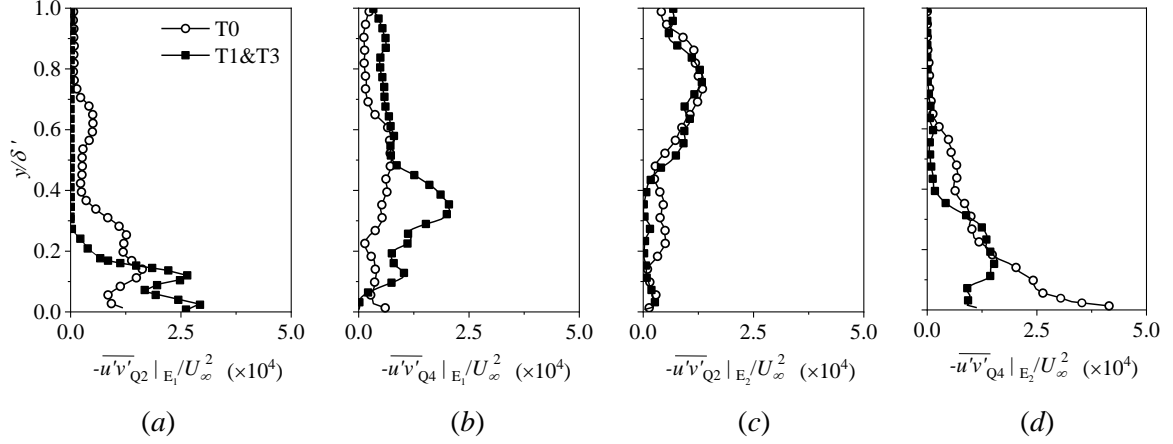


Figure 2.16. Conditional averaging of shear stress contribution based on the large-scale Q2 ( $E_1$ ) and Q4 ( $E_2$ ) events in the logarithmic layer for (a,b) the fully developed flow (T1&T3 at  $H = 0.170$  m) and (c,d) the developing flow (T0 at  $H = 0.170$  m). The subscript  $Q_i$  indicates the contribution in ejection and sweep events for  $i = 2$  and  $4$ , respectively.

Finally, the total shear stress contribution to Q2 and Q4 (considering the instances that belong to either  $E_1$  or  $E_2$ ) is calculated for test cases T0 and T1&T3 and their ratio ( $-\overline{u'v'}_{Qi}|_{E_1+E_2, T1\&T3} / -\overline{u'v'}_{Qi}|_{E_1+E_2, T0}$ ,  $i = 2$  or  $4$  based on the quadrant) is presented in figure 2.17(a), which substantiates the previous findings. Except in the region close to the bed ( $y/\delta' \leq 0.15$ ), the shear stress contribution to sweep events is higher in case of fully developed flow due to the constraint created by the free surface, whereas ejections dominate in the developing flow. To evaluate the contribution of ejections over sweeps for individual test cases, the ratio of shear stress contributions to Q2 and Q4 ( $R_{Q2/Q4}|_{E_1+E_2}$ ) is calculated and its depthwise variation is provided in figure 2.17(b) to compare the test cases T0 and T1&T3. A similar trend is found in the outer domain ( $y/\delta' \geq 0.3$ ) for both test cases. The shear stress contribution from Q2 in both cases is higher than that of Q4 between  $0.6 \leq y/\delta' \leq 1$  and lower than the contribution of Q4 in the region  $0.3 \leq y/\delta' \leq 0.6$ . However, a significant difference can be seen in the magnitude of  $R_{Q2/Q4}|_{E_1+E_2}$ . For example, the magnitude of  $R_{Q2/Q4}|_{E_1+E_2}$  is greater than one at  $0.6 \leq y/\delta' \leq 1$  in both test cases but the peak value of  $R_{Q2/Q4}|_{E_1+E_2}$  is nearly three times higher in the case of developing flow. The distribution of  $R_{Q2/Q4}|_{E_1+E_2}$  in the region  $0.6 \leq y/\delta' \leq 1$  implies that the contribution from sweeps are comparatively much higher in the fully developed flow (similar to what was mentioned in the previous discussions) although, qualitatively, they have shown a similar trend since the ejections near the edge of the boundary layer are dominant over sweeps in both cases. This alteration in the quadrant events near the boundary layer edges may also affect the flow in the inner domain, the evidence of which can be found in the distribution of  $R_{Q2/Q4}|_{E_1+E_2}$  near the bed ( $y/\delta' \leq 0.15$ ). In this region, ejections are major shear stress contributor in the developed flow whereas, maximum shear stress is generated by sweeping events in the developing flow.

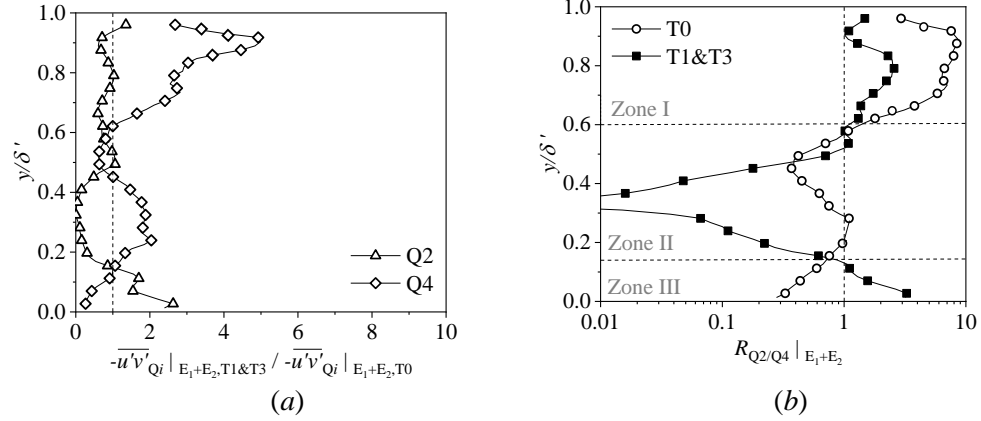


Figure 2.17. (a) Ratio of total shear stress contribution by T1&T3 and T0 (to Q2 or Q4 events). (b) Ratio of total shear stress contribution to Q2 and Q4 events (for T0 and T1&T3). The instances which belong to either  $E_1$  or  $E_2$  are considered here to estimate shear stress contributions.

Based on the observations in figure 2.17, the whole depth of flow in the fully developed state can be divided into three domains: (1) zone I ( $0.6 \leq y/\delta' \leq 1$ , dominated by ejections), (2) zone II ( $0.15 \leq y/\delta' \leq 0.6$ , dominated by sweeps) and (3) zone III ( $0 \leq y/\delta' \leq 0.15$ , dominated by ejections). These three zones, depending on their depthwise positions, can be correlated as the region between the TNTI and the free surface, the outer boundary layer flow upto TNTI and the logarithmic layer, respectively. The existence of these three layers reconfirms the vertical variability in the flow characteristics due to strong influence of the free surface.

## 2.7. Summary and conclusions

The characteristics of the fully developed flow in an open channel are explored using planar PIV measurements. Four different upstream tripping arrangements (T0, T1, T1&T2, T1&T3) are used at two channel aspect ratios, keeping the flow Reynolds number the same. T2 and T3 are additional trips that are used along with a standard trip T1 to stimulate the fully developed flow at aspect ratios of nine and seven, respectively. In fully developed open channel flows, the free stream region is theoretically not present and the flow in the outer layer is influenced by the presence of the free surface. Although free surface velocity or the maximum velocity has been widely used as the equivalent free stream velocity, uncertainty caused by the free surface perturbations is reasonably high, thus causing inaccuracy in the calculation of boundary layer thickness as compared to a standard turbulent boundary layer. A validation of the ‘log-law’ and ‘velocity defect law’ may not be sufficient in resolution of the fully developed state in open channel flow. Therefore, a revised boundary layer thickness ( $\delta'$ ) is estimated based on the turbulence characteristics and higher-order moments. T1&T2 is the fully developed state at an aspect ratio of nine ( $H = 0.135$  m) while T1&T3 is the comparable flow at an aspect ratio of seven ( $H = 0.170$  m) in this study. The bed-normal distribution of mean velocity, Reynolds stresses and higher-order turbulence of the two fully developed test cases are evaluated to check the self-similarity and the validity with previous literature, and it provides a good collapse between data sets. This ensures that  $\delta'$  is the more reliable and acceptable choice of the boundary layer thickness in open channel flow studies. Once the fully

developed open channel flow is achieved, the characteristics of the state of the flow is explored by identifying the zones of uniform momentum. The number of momentum zones in each instance is determined by the peaks in the PDF diagram which is created by using the velocity data below the TNTI. The position of the TNTI is estimated using the method of Chauhan *et al.* (2014a,b) with some modifications to suit open channel flow. The PDFs of  $U/U_\infty$  show a maximum of six peaks for a bin size of  $0.5U_\tau$  but only the instances with  $2 \leq N_{UMZ} \leq 4$  are considered for the momentum zone analysis based on a cut-off probability density. The characterisation of momentum zones reveals existence of large-scale Q2 events in the logarithmic layer for the higher number of momentum zones and large-scale Q4 events for a lower number of momentum zones which is substantiated by the distributions of velocity deficit. In fully developed state, the characteristics of large-scale fluid motion above the logarithmic layer is opposite i.e., large-scale Q2 events are present for lower number of momentum zones and large-scale Q4 events can be found when number of momentum zones is higher. The conditional averaging of  $R_{Q2/Q4}$  based on the value of  $N_{UMZ}$  shows a vertical variability in the flow characteristics in the fully developed state which is not present in the developing flow. Finally, large-scale ejections and sweep motions are correlated with the pointwise quadrant analysis which demonstrates the difference in the shear stress distribution to quadrant events between the developing and the developed flow condition. In the outer layer, the sweeping events in the fully developed flow have higher shear generation compared to the developing flow due to the influence of the free surface. In fully developed flow, the boundary layer thickness is of the order of the total depth of flow and a free stream region is theoretically not present. Therefore, momentum exchange between the boundary layer and the outer flow domain is not possible or highly restricted by the free surface, altering the inner flow characteristics of fully developed flow more prominently than the developing flow. Although this alteration of flow properties cannot be depicted in the time-averaged statistics, the vertical variability and temporal heterogeneity in the fully developed flow may create inconsistency in fluid-structure interaction studies since the fluid that approaches and interacts with the structure has significantly different inner flow properties.

## References

- Adrian, R. J., Meinhart, C. D. & Tomkins, C. D. 2000 Vortex organization in the outer region of the turbulent boundary layer. *J. Fluid Mech.* **422**, 1–54.
- Afzal, B., Faruque, M. A. & Balachandar, R. 2009 Effect of Reynolds number, near-wall perturbation and turbulence on smooth open-channel flows. *J. Hydraul. Res.* **47** (1), 66–81.
- Andreopoulos, J., Durst, F., Zaric, Z. & Jovanovic, J. 1984 Influence of Reynolds number on characteristics of turbulent wall boundary layers. *Exp. Fluids* **2** (1), 7–16.
- Balachandar, R. & Bhuiyan, F. 2007 Higher-order moments of velocity fluctuations in an open-channel flow with large bottom roughness. *J. Hydraul. Eng.* **133** (1), 77–87.
- Balachandar, R., Blakely, D., Tachie, M. & Putz, G. 2001 A study on turbulent boundary layers on a smooth flat plate in an open channel. *J. Fluids Eng.* **123** (2), 394–400.
- Balachandar, R. & Patel, V. C. 2005 Velocity measurements in a developed open channel flow in the presence of an upstream perturbation. *J. Hydraul. Eng.* **43** (3), 258–266.

- Balachandar, R. & Ramachandran, S. S. 1999 Turbulent boundary layers in low Reynolds number shallow open channel flows. *J. Fluids Eng.* **121** (3), 684–689.
- Bonakdari, H., Larrarte, F., Lassabatere, L. & Joannis, C. 2008 Turbulent velocity profile in fully-developed open channel flows. *Environ. Fluid Mech.* **8** (1), 1–17.
- Cameron, S. M., Nikora, V. I. & Coleman, S. E. 2008 Double-averaged velocity and stress distributions for hydraulically-smooth and transitionally-rough turbulent flows. *Acta Geophys.* **56** (3), 642–653.
- Cardoso, A. H., Graf, W. H. & Gust, G. 1989 Uniform flow in a smooth open channel. *J. Hydraul. Res.* **27** (5), 603–616.
- Chauhan, K., Monkewitz, P. A. & Nagib, H. M. 2009 Criteria for assessing experiments in zero pressure gradient boundary layers. *Fluid Dyn. Res.* **41** (2), 021404.
- Chauhan, K., Nagib, H. & Monkewitz, P. 2007 On the composite logarithmic profile in zero pressure gradient turbulent boundary layers. *In 45th AIAA Aerospace Sciences Meeting and Exhibit*, p. 532.
- Chauhan, K., Philip, J. & Marusic, I. 2014a Scaling of the turbulent/non-turbulent interface in boundary layers. *J. Fluid Mech.* **751**, 298–328.
- Chauhan, K., Philip, J., de Silva, C. M., Hutchins, N. & Marusic, I. 2014b The turbulent/non-turbulent interface and entrainment in a boundary layer. *J. Fluid Mech.* **742**, 119–151.
- Chen, X., Chung, Y. M. & Wan, M. 2020 Uniform-momentum zones in a turbulent pipe flow. *J. Fluid Mech.* **884**, A25.
- Clauser, F. H. 1956 The turbulent boundary layer. *Adv. Appl. Mech.* (Eds., H.L. Dryden and T. von Karman) **4**, 1–51.
- Clift, R., Grace, J. R. & Weber, M. E. 1978 Bubbles, Drops, and Particles. Academic Press, New York, US.
- Coles, D. 1956 The law of the wake in the turbulent boundary layer. *J. Fluid Mech.* **1** (2), 191–226.
- Djenidi, L., Talluru, K. M. & Antonia, R. A. 2019 A velocity defect chart method for estimating the friction velocity in turbulent boundary layers. *Fluid Dyn. Res.* **51** (4), 045502.
- Eisma, J., Westerweel, J., Ooms, G. & Elsinga, G. E. 2015 Interfaces and internal layers in a turbulent boundary layer. *Phys. Fluids.* **27** (5), 055103.
- Erm, L. P. & Joubert, P. N. 1991 Low-Reynolds-number turbulent boundary layers. *J. Fluid Mech.* **230**, 1–44.
- Flack, K. A., Schultz, M. P. & Shapiro, T. A. 2005 Experimental support for Townsend’s Reynolds number similarity hypothesis on rough walls. *Phys. Fluids.* **17** (3), 035102.
- Forliti, D. J., Strykowski, P. J. & Debatin, K. 2000 Bias and precision errors of digital particle image velocimetry. *Exp. Fluids* **28** (5), 436–447.
- Granville, P. S. 1976 A modified law of the wake for turbulent shear layers. *J. Fluids Eng.* **98**, 578–580.
- Grass, A. J. 1971 Structural features of turbulent flow over smooth and rough boundaries. *J. Fluid Mech.*, **50** (2), 233–255.
- Guo, J., Julien, P. Y. & Meroney, R. N. 2005 Modified log-wake law for zero-pressure gradient turbulent boundary layers. *J. Hydraul. Res.* **43** (4), 421–430.
- Gad-el Hak, M. & Bandyopadhyay, P. R. 1994 Reynolds number effects in wall-bounded turbulent flows. *Appl. Mech. Rev.* **47** (8), 307–365.

- Heidari, M., Balachandar, R., Roussinova, V. & Barron, R. M. 2017 Reconsideration of the overlap region in smooth shallow open channel flows. *Can. J. Civ. Eng.* **44** (3), 161–173.
- Hinze, J. O. 1959 *Turbulence: An Introduction to its Mechanism and Theory*. McGraw-Hill Book Company Inc., New York.
- Hoffmann, J. A. & Mohammadi, K. 1991 Velocity profiles for turbulent boundary layers under freestream turbulence. *J. Fluids Eng.* **113** (3), 399–404.
- Keulegan, G. H. 1938 *Laws of turbulent flow in open channels*, vol. 21. National Bureau of Standards US.
- Kirkgöz, M. S., & Ardiçlioğlu, M. 1997 Velocity profiles of developing and developed open channel flow. *J. Hydraul. Eng.* **123** (12), 1099–1105.
- Kironoto, B. A. & Graf, W. H. 1995 Turbulence characteristics in rough non-uniform open-channel flow. *Proc. Instn. Civ. Engrs. Wat., Marit. & Energy.* **112** (4), 336–348.
- Kolmogorov, A. N. 1991 The local structure of turbulence in incompressible viscous fluid for very large Reynolds numbers. *Proc. Royal Soc. Lond.* **434** (1890), 9–13.
- Krogstad, P. A., Antonia, R. A. & Browne, L. W. B. 1992 Comparison between rough- and smooth-wall turbulent boundary layers. *J. Fluid Mech.* **245**, 599–617.
- Laskari, A., de Kat, R., Hearst, R. J. & Ganapathisubramani, B. 2018 Time evolution of uniform momentum zones in a turbulent boundary layer. *J. Fluid Mech.* **842**, 554–590.
- Longmire, E. K. & Eaton, J. K. 1992 Structure of a particle-laden round jet. *J. Fluid Mech.* **236**, 217–257.
- Lu, S. S. & Willmarth, W. W. 1973 Measurements of the structure of the Reynolds stress in a turbulent boundary layer. *J. Fluid Mech.* **60** (3), 481–511.
- Mahananda, M., Hanmaiahgari, P. R., Ojha, C. S. P. & Balachandar, R. 2019 A new analytical model for dip modified velocity distribution in fully developed turbulent open channel flow. *Can. J. Civ. Eng.* **46** (8), 657–668.
- Marusic, I., Chauhan, K., Kulandaivelu, V. & Hutchins, N. 2015 Evolution of zero-pressure-gradient boundary layers from different tripping conditions. *J. Fluid Mech.* **783**, 379–411.
- Meinhart, C. D. & Adrian, R. J. 1995 On the existence of uniform momentum zones in a turbulent boundary layer. *Phys. Fluids* **7** (4), 694–696.
- Mignot, E., Hurther, D. & Barthelemy, E. 2011 Double-averaging turbulence characteristics in flows over a gravel bed. *J. Hydraul. Res.* **49** (5), 703–704.
- Miguntanna, N. S., Moses, H., Sivakumar, M., Yang, S. Q., Enever, K. J. & Riaz, M. Z. B. 2020 Re-examining log law velocity profile in smooth open channel flows. *Environ. Fluid Mech.* pp. 1–34.
- Monkewitz, P. A., Chauhan, K. A. & Nagib, H. M. 2007 Self-consistent high-Reynolds number asymptotics for zero-pressure-gradient turbulent boundary layers. *Phys. Fluids.* **19** (11), 115101.
- Nakagawa, H. & Nezu, I. 1977 Prediction of the contributions to the Reynolds stress from bursting events in open-channel flows. *J. Fluid Mech.* **80** (1), 99–128.
- Nasif, G., Balachandar, R. & Barron, R. M. 2020 Supercritical flow characteristics in smooth open channels with different aspect ratios. *Phys. Fluids.* **32** (10), 105102.
- Nezu, I. 2005 Open channel flow turbulence and its research prospect in the 21<sup>st</sup> century. *J. Hydraul. Eng.* **131**(4), 229-246.



- Nezu, I. & Rodi, W. 1986 Open channel flow measurements with a laser doppler anemometer. *J. Hydraul. Eng.* **112** (5), 335–355.
- Nikora, V., Ian, M., Stephen, M., Stephen, C., Dubravka, P. & Roy, W. 2007 Double-averaging concept for rough-bed open-channel and overland flows: Theoretical background. *J. Hydraul. Eng.* **133** (8), 873–883.
- Peruzzi, C., Poggi, D., Ridolfi, L. & Manes, C. 2020 On the scaling of large-scale structures in smooth-bed turbulent open-channel flows. *J. Fluid Mech.* **889**, A1.
- Pizer, S. M., Amburn, E. P., Austin, J. D., Cromartie, R., Geselowitz, A., Greer, T., Ter Haar Romeny, B., Zimmerman, J. B. & Zuiderveld, K. 1987 Adaptive histogram equalization and its variations. *Comput. Gr. Image Process.* **39** (3), 355–368.
- Prandtl, L. 1925 Bericht über untersuchungen zur ausgebildeten turbulenz. *Z. Angew. Math. Mech.* **5**, 136–139.
- Pu, J. H., Tait, S., Guo, Y., Huang, Y. & Hanmaiahgari, P. 2018 Dominant features in three-dimensional turbulence structure: comparison of non-uniform accelerating and decelerating flows. *Environ. Fluid Mech.* **18** (2), 395–416.
- Reynolds, O. 1883 An experimental investigation of the circumstances which determine whether the motion of water shall be direct or sinuous, and of the law of resistance in parallel channels. *Philos. Trans. Royal Soc.* **174**, 935–982.
- Roussinova, V. 2009 Turbulent structures in smooth and rough open channel flows: effect of depth. PhD thesis, University of Windsor, Canada.
- Roussinova, V., Biswas, N. & Balachandar, R. 2008 Revisiting turbulence in smooth uniform open channel flow. *J. Hydraul. Res.* **46** (sup1), 36–48.
- Sarkar, S. 2016 Measurement of turbulent flow in a narrow open channel. *J. Hydrol. Hydromech.* **64** (3), 273–280.
- Sarkar, S. & Dey, S. 2010 Double-averaging turbulence characteristics in flows over a gravel bed. *J. Hydraul. Res.* **48** (6), 801–809.
- Sciacchitano, A., Neal, D. R., Smith, B. L., Warner, S. O., Vlachos, P. P., Wieneke, B. & Scarano, F. 2015 Collaborative framework for PIV uncertainty quantification: comparative assessment of methods. *Meas. Sci. Technol.* **26** (7), 074004.
- Shavit, U., Lowe, R. J. & Steinbuck, J. V. 2007 Intensity capping: a simple method to improve cross-correlation PIV results. *Exp. Fluids* **42** (2), 225–240.
- de Silva, C. M., Hutchins, N. & Marusic, I. 2016 Uniform momentum zones in turbulent boundary layers. *J. Fluid Mech.* **786**, 309–331.
- de Silva, C. M., Marusic, I. & Hutchins, N. 2014 Regions of uniform streamwise momentum in turbulent boundary layers. *In 19th Australasian Fluid Mechanics Conference, RMIT University, Melbourne, Australia (8-11th December)*.
- de Silva, C. M., Philip, J., Hutchins, N. & Marusic, I. 2017 Interfaces of uniform momentum zones in turbulent boundary layers. *J. Fluid Mech.* **820**, 451–478.
- Simpson, R. L., Chew, Y. T. & Shivaprasad, B. G. 1981 The structure of a separating turbulent boundary layer. Part 2. Higher-order turbulence results. *J. Fluid Mech.* **113**, 53-73.
- Singha, A. 2009 Shallow wake in open channel flow - a look into the vertical variability. PhD thesis, University of Windsor, Canada.
- Song, T. & Chiew, Y. M. 2001 Turbulence measurement in nonuniform open-channel flow using acoustic doppler velocimeter (ADV). *J. Eng. Mech.* **127** (3), 219–232.

- Spalart, P. R. 1988 Direct simulation of a turbulent boundary layer up to  $Re_\theta=1410$ . *J. Fluid Mech.* **187**, 61-98.
- Steffler, P. M., Rajaratnam, N. & Peterson, A. W. 1985 LDA measurements in open channel. *J. Hydraul. Eng.* **111** (1), 119–130.
- Tachie, M. F., Balachandar, R. & Bergstrom, D. J. 2003 Low Reynolds number effects in open-channel turbulent boundary layers. *Exp. Fluids.* **34**(5), 616-624.
- Taylor, G. I. 1937 The statistical theory of isotropic turbulence. *J. Aeronaut. Sci.* **4** (8), 311–315.
- Thielicke, W. & Stamhuis, E. 2014 PIVlab - towards user-friendly, affordable and accurate digital particle image velocimetry in MATLAB. *J. Open Res. Softw.* **2** (1).
- Wiener, N. 1964 Extrapolation, Interpolation, and Smoothing of Stationary Time Series: With Engineering Applications. M.I.T. Press, Massachusetts, US.
- Yang, S. Q., Tan, S. K. & Lim, S. Y. 2004 Velocity distribution and dip-phenomenon in smooth uniform open channel flows. *J. Hydraul. Eng.* **130** (12), 1179–1186.

## CHAPTER 3

### EFFECT OF FREE SURFACE PERTURBATION ON THE CHARACTERISTICS OF FULLY DEVELOPED SMOOTH OPEN CHANNEL FLOW

The effect of free surface perturbation on the downstream turbulence characteristics in a smooth open channel flow is investigated using PIV at a constant depth Reynolds number of  $3.5 \times 10^4$ . The perturbations of varying degrees are imposed using light boards floating on the free surface. In the presence of the perturbation, the mean velocity profiles show a dip while the Reynolds shear stress tends to become negative near the free surface. The perturbation effect is prominent in the profiles of the higher-order moments, which show significant alteration of turbulence characteristics. The orientation of JPDF of velocity fluctuations near free surface shifts from ejection and sweep events to outward and inward interactions in the presence of perturbations. The ratio of shear stress contribution due to the combination of ejections and sweeps, to that by combined inward and outward interactions, shows that the shear penetration is farther towards the bed with increase in perturbation.

**Keywords:** Boundary layer turbulence, Free surface perturbation, Higher-order moments, Open channel flow turbulence, Particle Image Velocimetry (PIV), Quadrant analysis, Reynolds stresses.

#### 3.1. Introduction

The study of fluid-structure interaction is of perennial interest to hydraulic engineers. Many laboratories and research groups world-wide are focussed on studying various aspects of this interaction. In the laboratory, it is necessary to have a fully developed flow approaching the structure in order to dynamically match the fluid-structure interaction with field conditions and with the experiments being conducted in other laboratories. Moreover, to validate CFD predictions, a fully developed approach flow as an inlet condition is required to maintain consistency in results between different studies. However, the approach flow may deviate from the fully developed state due to external perturbations causing scale effects, which result in improper modelling of the flow physics. The use of floater boards in laboratory flumes to dampen the free surface fluctuations is one such example of an external perturbation which may unintentionally alter the downstream turbulence characteristics.

In many respects, the fully developed flow in a smooth open channel resembles a typical turbulent boundary layer (TBL). As in TBLs, open channel flow (OCF) has been traditionally divided into inner and outer regions. The inner region consists of a viscous sublayer, a buffer layer and a logarithmic layer. The velocity distribution in the overlapping logarithmic layer is described by the well-known log-law:

$$\frac{U}{U_\tau} = \frac{1}{\kappa} \ln \left[ \frac{yU_\tau}{\nu} \right] + B \quad (3.1)$$

where  $U$  is the mean streamwise velocity,  $U_\tau$  is the shear velocity and  $\nu$  is the kinematic viscosity of the fluid. For a smooth wall turbulent boundary layer, the von Kármán constant  $\kappa$  is taken as 0.41 and  $B$  is between 5.0 and 5.5 (Steffler *et al.* 1985, Nezu and Rodi 1986, Balachandar *et al.*

2001). To include the outer region, Coles (1956) modified the log-law by adding a wake function ( $w$ ) to quantify the mean velocity deficit as:

$$\frac{U_\infty - U}{U_\tau} = -\frac{1}{\kappa} \ln\left(\frac{y}{\delta}\right) + \frac{2\Pi}{\kappa} \left( w\left(\frac{y}{\delta}\right) \right) \quad (3.2)$$

where  $\delta$  is the boundary layer thickness,  $\Pi$  is the wake parameter which represents the deviation of mean velocity from the log-law at  $y = \delta$ . Using a large data set of TBL results, Chauhan *et al.* (2009) suggested a positive value of  $\Pi$  ( $0.44 \pm 0.05$ ). However, there is no well-defined value for  $\Pi$  in open channels. Balachandar and Patel (2005) noted it to be 0.4 in open channel flow, Kirkgöz and Ardiçlioğlu (1997) reported a  $\Pi$  value of 0.1, whereas Cardoso *et al.* (1989) and Roussinova *et al.* (2008) deciphered it to be a negative value ( $\approx -0.3$ ). Although much of our understanding of open channel turbulence characteristics is borrowed from zero-pressure gradient TBLs, there is a clear distinction between them. In OCF, the free surface behaves like a weak wall and can significantly influence the inner flow (Nezu, 2005). When the flow is fully developed, theoretically the boundary layer thickness is equal to the flow depth and there is no free stream region as in a TBL flow. Therefore, interaction between the free stream and the boundary layer region does not occur and the effect of confinement due to the free surface is inevitable. A small perturbation at the free surface can influence the turbulence field since the disturbance can potentially get amplified. Handler *et al.* (1993) and Das *et al.* (2021) reported a higher value of pressure-strain term and dissipation rate near the free surface compared to the free stream in zero-pressure gradient TBL flows. Brocchini and Peregrine (2001) explained the dynamics of the free surface turbulence and discussed the sustenance of this turbulence. The effects of free surface turbulence were also studied by enhancing the level of perturbation using a bluff body near the free surface (Reichl *et al.* 2005, Sheridan *et al.* 1997, Balachandar and Patel 2005, Lin and Rockwell 1999), or by creating surface waves (Li *et al.* 2005, Singh *et al.* 2018). A bluff body can also create a significant free surface deformation based on the gap between the body and the free surface and the prevailing Froude number of the flow. At low Froude number, Reichl *et al.* (2005) found a similarity between wake characteristics of a cylinder near a free surface and a cylinder near a solid wall. Balachandar and Patel (2005) used a square cylinder spanning the width of the flume and placed it close to the free surface to generate an upstream perturbation in the flow field. They found that the effect of the bluff body persisted at a downstream location which was located 27 times the depth of flow from the source of the perturbation. A similar conclusion has been made by Balachandar *et al.* (1997) and Balachandar and Tachie (2001) even in the case of a slender bluff body placed in the flow. Cimbala *et al.* (1988) mentioned that the growth of shedding vortices is possible due to hydrodynamic instability in the flow and large-scale structures may exist at a far downstream location. This confirms that the disturbance generated from a bluff body near the free surface may sustain for a long distance without any additional source of turbulence. However, these perturbations were created intentionally to study the flow in the downstream region.

In hydraulic engineering laboratories, light floater boards are placed on the free surface at the inlet section of the flume to suppress the free surface waves. Their effect on the velocity characteristics at a downstream measuring station has been previously assumed to be negligible. In the present study, we have compared the characteristics of open channel flows at a far downstream location with and without the presence of a floater board. In the beginning, the flow is allowed to

develop to a fully developed state to set a base condition. The free surface perturbation is then introduced, and the level of perturbation is increased gradually to observe the changes in the dynamics of the flow. The influence of the free surface perturbation is evaluated by comparing the profiles of the mean velocity with the fully developed state. The quadrant decomposition of velocity fluctuations is carried out to acquire a better understanding of the coherent events. The probability density function and the joint probability density function of velocity fluctuations reveal the nature of turbulence dispersion inside the flow field. Finally, the extent of shear layer penetration into the flow domain is discussed using the distribution of shear stress contribution from each quadrant and the anisotropy tensor.

### 3.2. Experimental setup

The experiments were carried out in a recirculating water flume of the Hydraulic Engineering Research Laboratory at the Centre for Engineering Innovation (CEI), University of Windsor. The flume is 16 m in length, 1.2 m in width and 0.8 m in depth. Flow straighteners are used in the upstream section to create uniformity in the inflow turbulence. A tailgate at the end of the flume is used to adjust the flow depth by allowing a free fall into the settling tank. In our experiments, the pump was operated at a constant frequency of 20 Hz to maintain a mean inlet depth averaged velocity ( $U_o$ ) of 0.26 m/s and a flow depth ( $H$ ) of 0.135 m, i.e., the depth Reynolds number ( $Re_H$ ) is kept fixed at 35,100. The aspect ratio (width/depth,  $b/H$ ) is maintained to be seven and the velocity measurements are carried out in the central plane of the channel. At higher aspect ratios ( $\geq 5$ ), it is known that there exists a section of two-dimensional flow in the centre of the flume which is free from the effects of secondary currents (Nasif *et al.* 2020). Therefore, employing a higher aspect ratio enables us to identify the effects of free surface perturbations without any significant influence of secondary currents. In the beginning, a base test case (F0) was set up without any free surface perturbation. The flow was tripped with a patch of coarse roughness elements to stimulate the flow to a fully developed state in the measurement section. The trip was installed on the flume bed near the inlet section (see table 3.1). In the fully developed state, the Reynolds number based on the displacement thickness ( $Re_\theta$ ) was 3791, where  $\theta$  is the momentum





Inflow conditions	Test cases	Test conditions								
	<b>F0:</b> No floater board is used, fully developed state	<b>Floater details:</b> <table border="1"> <thead> <tr> <th>Floaters</th> <th>Floater details</th> </tr> </thead> <tbody> <tr> <td>F1</td> <td><math>L = 0.5</math> m</td> </tr> <tr> <td>F2</td> <td><math>L = 1.5</math> m</td> </tr> <tr> <td>F1M</td> <td><math>L = 0.5</math> m Mesh: 1 mm sq. opening 1 mm thick</td> </tr> </tbody> </table> <b>Geometry details:</b> <ul style="list-style-type: none"> <li>Distance between starting edge of the floater and FOV = 4.5 m</li> <li>Distance between trip and FOV = 2.5 m</li> </ul>	Floaters	Floater details	F1	$L = 0.5$ m	F2	$L = 1.5$ m	F1M	$L = 0.5$ m Mesh: 1 mm sq. opening 1 mm thick
Floaters	Floater details									
F1	$L = 0.5$ m									
F2	$L = 1.5$ m									
F1M	$L = 0.5$ m Mesh: 1 mm sq. opening 1 mm thick									
Short floater 	<b>F1:</b> A short floater is placed behind the flow straightener									
Long floater 	<b>F2:</b> A longer floater board is placed behind the flow straightener									
Short floater + Mesh 	<b>F1M:</b> The short floater wrapped with a square mesh is used									

Table 3.1. Test conditions

thickness. The shape factor of the mean velocity profile ( $\delta^*/\theta$ ) is 1.31, where  $\delta^*$  was the displacement thickness. The Froude number ( $U_o/\sqrt{gh}$ , where  $g$  is the gravitational acceleration) of the flow was maintained as 0.2.

Following the data acquisition for the base case, the measurements were repeated with floaters of different lengths. Tests F1 and F2 use a floater with length of 0.5 and 1.5 m, respectively. Details of the floater boards and test conditions are presented in [table 3.1](#). The floaters were placed on the free surface in the immediate downstream of the flow straighteners, similar to that observed in many laboratories. The floater boards were made of Styrofoam and the test section was 4.5 m downstream from the edge of the floater. The fourth test case, F1M was similar to test case F1, except that the floater was wrapped with a fine wire mesh having 1 mm wire thickness and 1 mm square openings.

The field-of-view (FOV) was chosen approximately  $30H$  downstream of the floaters. Velocity components in the central vertical plane were measured with a two-dimensional planar PIV system. A dual pulse Nd:YAG lasers (532 nm wavelength at 50 mJ/pulse) was operated at a pulse repeat frequency of 2.9 Hz. Laser pulse duration was 4 ns and the time between two laser pulses was set at 2.3 ms. The laser was placed below the flume to minimize the scattering effect at the free surface. Using a combination of spherical and cylindrical lenses, the laser sheet was set to 1 mm thickness to reduce the effects of out-of-plane particle motion. The flow was seeded with 10  $\mu\text{m}$  spherical silver-coated hollow glass spheres with an effective density of 1100  $\text{kg}/\text{m}^3$ . The ability of the particles to follow the flow can be quantified by the particle Stokes number ( $St_p$ ) which can be calculated as the ratio of particle response time to the turbulence time scale (Longmire and Eaton 1992). The value of  $St_p$  was evaluated as  $5.31 \times 10^{-5}$ , which satisfies the criterion proposed by Clift *et al.* (1978):  $St_p \ll [2(\rho_p/\rho) + 1] / 9 = 0.36$ . A PowerViewPlus 8 MP CCD camera with Nikon AF NIKKOR 50 mm f/1.8D lens was used to acquire 4000 image pairs of resolution 3320 pixels  $\times$  2496 pixels. The camera was operated in dual capture mode synchronized with the laser pulse repeat frequency of 2.9 Hz. The images were processed in PIVlab using a Fast Fourier Transform (FFT) window deformation algorithm with an interrogation area of  $16 \times 16$  pixels (reduced from  $64 \times 64$  pixels in two steps with 50% overlap). Less than 5% of the vectors were identified as bad and replaced with interpolated vectors. A Matlab code was developed for post-processing of the data sets. The mean velocity measurement had an uncertainty of 2% and 4000 images were found to be sufficient to evaluate the turbulence characteristics, with a maximum uncertainty of 3% for Reynolds stresses at mid-depth. The details of uncertainty analysis are provided in Das *et al.* (2021) and not repeated here for brevity.

Mean and turbulence parameters are calculated by double-averaging of the data set over the 4000 instances. Double-averaging is a straightforward space-time (ensemble) averaging of the velocity field (Cameron *et al.*, 2008, Mignot *et al.*, 2011, Vladimir *et al.*, 2007, Sarkar and Dey, 2010). Initially, time-averaged velocities are determined, and the velocity fluctuations ( $u', v'$ ) are calculated by subtracting the mean from the instantaneous data. Reynolds stresses and higher-order turbulence characteristics are computed from the velocity fluctuations. Spatial-averaging of these time-averaged data provide the final distribution of the mean and turbulence parameters. Double-averaging is used in the present study since a larger data set can provide better turbulence statistics. However, in the test cases F1, F2 and F1M, the flow is dissipative in nature. The strength of the shear layer that is shed from the floaters is expected to reduce in the downstream direction. Unlike a fully developed flow, double-averaging is not ideally valid for such a condition. In [figure 3.1](#), the

mean and turbulence parameters at three different locations in the FOV ( $x/\mathcal{L} = 0.25, 0.50, 0.75$ , where  $\mathcal{L} = 250$  mm is the FOV length) are compared with the double-averaged (DA) profiles (represented by the dashed lines) for the test case with the largest free surface perturbation (F1M). Figure 3.1(a,b,c) shows the bed-normal distribution of mean streamwise velocity ( $U$ ), Reynolds normal stress ( $\overline{u'^2}$ ) and Reynolds shear stress ( $-\overline{u'v'}$ ) normalized by mean inflow velocity ( $U_o$ ). In figure 3.1(d), third-order moments of streamwise velocity fluctuations are presented in the form of the skewness factor:  $S_u = \overline{u'^3} / (\overline{u'^2})^{3/2}$ . The mean velocity profiles and Reynolds normal stresses at all three location exhibit almost no difference. A minor deviation is noticed in the case of Reynolds shear stresses and the third-order moment. Considering the uncertainty in calculating the higher-order moments, these deviations are likely to have negligible effect on double-averaging. Also, streamwise variations of the mean velocity ( $U$ ) and Reynolds stress ( $\overline{u'^2}/U_o^2$ ) at three different depths ( $y/H = 0.2, 0.5, 0.8$ ) were monitored (not shown here for brevity) and was found to be insignificant over the length of the FOV. For the above reasons, double-averaging was adopted in the present study.

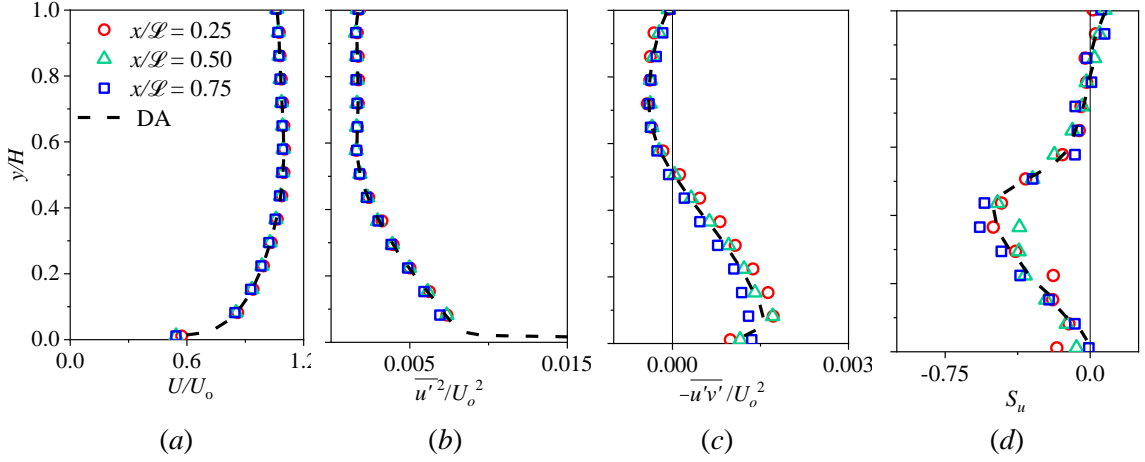


Figure 3.1. Distributions for test case F1M at three different  $x/\mathcal{L}$  locations: (a) streamwise velocity, (b) streamwise Reynolds normal stress, (c) Reynolds shear stress, (d) third-order moments of streamwise velocity fluctuations (in the form of skewness). The dashed-lines represent the double-averaged (DA) profiles.

### 3.3. Results and discussions

#### 3.3.1. Mean velocity distribution

The streamwise normalised mean velocity profiles in outer scaling ( $U/U_o$  and  $y/H$ ) and inner scaling ( $U^+ = U/U_\tau$  and  $y^+ = yU_\tau/\nu$ ) are presented in figure 3.2.  $U_\tau$  is calculated by optimizing the functions  $f_1$  and  $f_2$  defined by,

$$f_1(U_\tau) = \frac{dU}{dy} - \frac{U_\tau}{\kappa} \frac{1}{(y_i + y_o)} \quad (3.3)$$

$$f_2(U_\tau) = U - \frac{U_\tau}{\kappa} \ln \left[ \frac{(y_i + y_o)U_\tau}{\nu} \right] - U_\tau B \quad (3.4)$$

The values of  $\kappa$  and  $B$  are taken as 0.41 and 5, respectively. Double-averaged mean velocity data within a range of  $30 \leq y^+ \leq 0.2Re_\tau$  (where  $Re_\tau = U_\tau H / \nu$  and  $Re_\tau = U_\tau H / \nu$ ) are used in this analysis (Balachandar and Patel 2005). In the beginning,  $U_\tau$  is calculated using the total shear stress method, i.e.,  $U_\tau^2 = (v \partial U / \partial y - \overline{u'v'})_{y=0}$  which involves the extrapolation of the linear region of the Reynolds shear stress profile to the bed (Flack *et al.* 2005, Roussinova *et al.* 2008). This value of  $U_\tau$  is used as an initial guess while optimizing the function  $f_1$ , which uses a linear least squares fit algorithm in the form of  $y - mx = 0$ , forcing the intercept to be zero. Here,  $U_\tau/\kappa$  is the slope of the line ( $m$ ). The function  $f_2$  is then independently optimized in a similar fashion. This two-step method is repeated iteratively until the difference between two successive  $U_\tau$  values (from optimization of the functions  $f_1$  and  $f_2$ ) is less than a predefined threshold value. At each iteration,  $y_o$  is finely adjusted to get a converged solution. In the present analysis,  $y_o$  is taken as a small correction factor since true values of the  $y$  coordinates depend on the accuracy of masking of the PIV images (Das *et al.* 2021). The  $y$  coordinates are modified as  $y = y_i + y_o$ . The values of  $U_\tau$  corresponding to different test cases are presented in table 3.2. Based on these  $U_\tau$  values, Coles' wake strength parameter values ( $\Pi$ ) are calculated, which quantify the deviation of the experimental profiles from the log-law (Coles 1956).

Test cases	F0	F1	F2	F1M
$U_\tau$ (ms <sup>-1</sup> )	0.0119	0.0122	0.0124	0.0129
$\Pi$	0.52	0.17	-0.2	-0.37

Table 3.2. Shear velocity ( $U_\tau$ ) and wake strength parameter ( $\Pi$ ) for all test cases

As mentioned earlier, the flow is fully developed for test F0 and the bed-normal distribution of streamwise velocity component in this test case is represented by the closed symbols in the figure 3.2. In comparison to the fully developed profile, a clear dip is observed adjacent to the free surface when the floater is introduced (figure 3.2a). The dip is larger when the floater is longer or roughened by the wire mesh, which clearly indicates that the dip is caused by the shear layer developed from the bottom of the floater and transported downstream. The dip also changes the shape of the mean velocity profile because of the momentum re-distribution to satisfy continuity considerations. The cases of the flows with free surface perturbation have higher mean velocity values near the bed than that noticed in the fully developed flow to compensate for the lower velocity adjacent to the free surface. The velocity corresponding to the point of inflection in the velocity distribution is the highest in the test case F1M and located at the lowest bed-normal position, since the dip is the largest in this case. This redistribution of the mean streamwise velocity components cause a change in the values of shear velocities, which is directly related to the slope of the velocity profile. Therefore, the value of  $U_\tau$ , as shown in table 3.2, gradually increases with



the increase in free surface perturbation. In [figure 3.2\(b\)](#), the dip in the mean velocity profile creates a deviation from the fully developed state in the outer layer. This is quantified by the value of  $\Pi$ , which can be correlated to the distribution of the mean streamwise velocity component in the outer layer and also depends on the characteristics of inflow turbulence (Hoffmann and Mohammadi 1991). As shown in [table 3.2](#), the value of  $\Pi$  decreases with the increase in perturbations and becomes negative for higher perturbations in test F2 and F1M. In several previous research works, this dip phenomenon is commonly identified in the flow with low aspect ratio and related to the secondary currents. When the channel aspect ratio is less than five, a dip is observed in the mean velocity profile even in the central plane of an OCF (Bonakdari *et al.* 2008, Mahananda *et al.* 2019, Nakagawa and Nezu 1977, Nasif *et al.* 2020, Nezu and Rodi 1986, Yang Shu-Qing *et al.* 2004). However, laboratory experiments in OCF are also restricted in width due to the side walls of the flume. Kirkgöz and Ardiçlioğlu (1997) observed a dip in the velocity profile close to the side walls but absent in the center of the channel. In the present study, the measurements are obtained in the central vertical plane and the aspect ratio is kept larger than five. The fact that the dip is absent in the fully developed flow but observed for flows with free surface perturbations is a reflection of the role of the floater boards. The possible reasons for this dip are explained using the distribution of Reynolds stresses, the higher-order moments and quadrant analysis in the following sections.

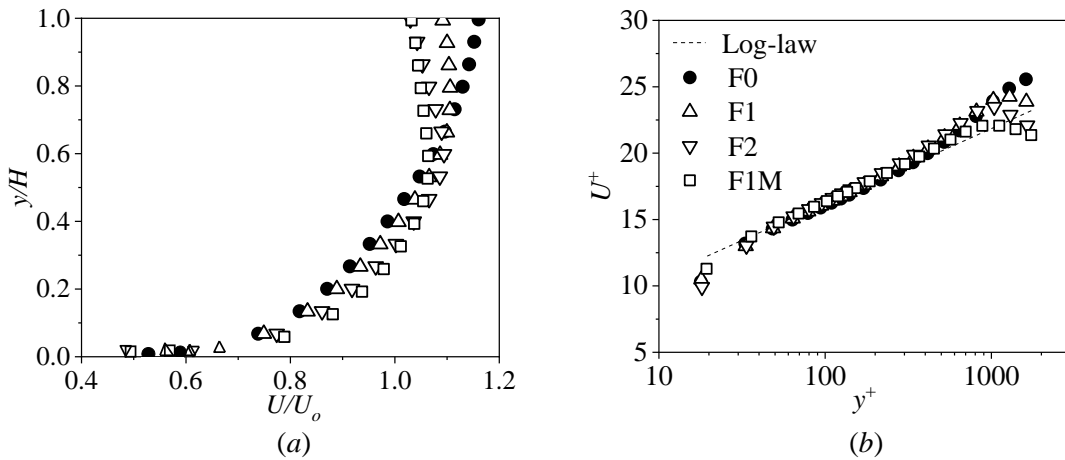


Figure 3.2. Normalized streamwise velocity profiles: (a) outer scaling, (b) inner scaling; (F0: no float, F1: shorter float, F2: longer float, F1M: shorter float with mesh).

### 3.3.2. Reynolds stresses

[Figure 3.3](#) presents the Reynolds stress ( $\overline{u'^2}$ ,  $\overline{v'^2}$  and  $-\overline{u'v'}$ ) profiles normalized by the mean streamwise inlet velocity ( $U_o$ ). For test F0, the Reynolds stresses are maximum near the bed and gradually decrease to a minimum value near the free surface. Starting at the bed and up to  $y/H = 0.4$ , the distributions of the Reynolds stresses in the perturbed cases are quite comparable with the fully developed flow. However, the perturbed cases show a clear distinction near the free surface since the shear layer developed from the bottom of the floater boards (due to the no-slip condition) is transported into the flow. This shear layer is not supported by any turbulence regeneration beyond the physical length of the floaters. Any perturbation generated from the floaters is expected to weaken downstream and diminish within a short distance. However, the effects of the free surface perturbation are clearly visible in the Reynolds stress profiles although the measuring station is

located far downstream of the floaters. The high level of perturbation in test F1M creates a bulge in the normal stress profiles above the depth  $y/H = 0.55$ , which is more prominent in [figure 3.3\(b\)](#). Interestingly, near the free surface, normal stresses are less in test F1 than that in F0 and more in tests F2 and F1M. It appears that the use of the short floater in test F1 results in reducing the free surface disturbance by the time the flow reaches the measuring station, while it is amplified (or at least not reduced) in case of the longer floater (F2) and the mesh wrapped floater (F1M).

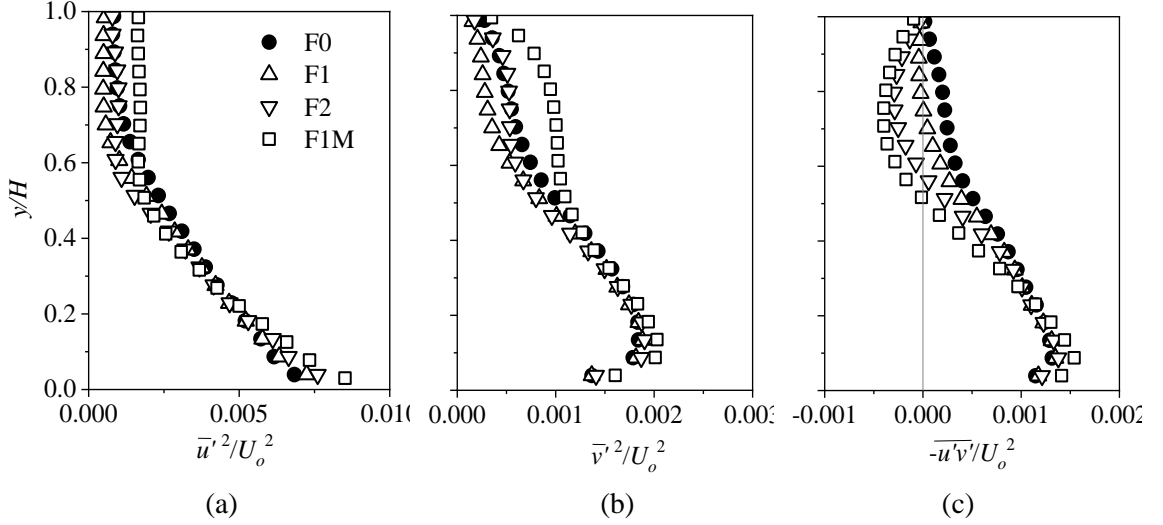


Figure 3.3. Distribution of Reynolds stresses, normalized by local mean velocity, (a) streamwise component, (b) bed-normal component, (c) shear stress component.

The normal stresses only provide an evaluation of the magnitude of the velocity fluctuations, whereas the Reynolds shear stress ( $-\bar{u}'v'/U_o^2$ ) retains the sign ( $\pm$ ) information. [Figure 3.3\(c\)](#) reveals the orientation of velocity fluctuations and illustrates why the normal stresses are low in the case of F1. The shear stress near the free surface reduces in F1 because of the change in sign of the velocity fluctuations and finally becomes negative with the increase in perturbation. This may happen when there is an alteration of the turbulence characteristics. When either of the velocity fluctuations change sign from positive to negative or vice-versa, there must be a transitional situation, where the magnitudes of the velocity fluctuations are close to zero. Therefore, the Reynolds stresses adjacent to the free surface are minimum in test F1. With increase in perturbation, the magnitude of the velocity fluctuations in the similar region starts to increase although their orientation or sign ( $\pm$ ) may be different from the fully developed case. Therefore, the Reynolds shear stress becomes negative in test cases F2 and F1M. The zone of negative shear is the largest in test F1M which displays the deepest turbulence penetration towards the bed.

### 3.3.3. Higher-order moments

Higher-order turbulence characteristics provide a deeper insight into the flow physics. Third-order moments are presented as skewness factors:  $S_u = (\overline{u'^3}) / (\overline{u'^2})^{3/2}$  and  $S_v = (\overline{v'^3}) / (\overline{v'^2})^{3/2}$ , whereas fourth-order moments are shown in the form of flatness factors:  $F_u = (\overline{u'^4}) / (\overline{u'^2})^2$  and  $F_v = (\overline{v'^4}) / (\overline{v'^2})^2$ . The values of skewness and flatness factors corresponding to a normal

distribution of velocity fluctuations are zero and three, respectively. A non-zero skewness value shows the nature of temporal variation of the turbulence properties, while a deviation of flatness value from three reveals the nature of intermittency in the flow. The distribution of skewness and flatness factors along the direction normal to the bed are presented in figure 3.4. The skewness profiles (figures 3.4a,b) in the test cases with free surface perturbation have a trend similar to the fully developed profile in the range  $0.0 \leq y/H \leq 0.4$  with minor deviations, which seem to increase with increasing  $y/H$ . As the near-bed turbulence characteristics are expected to be similar in all test cases, the deviations from the fully developed case are due to the influence from the free surface region penetrating into the flow. However, in figures 3.4(c,d), the flatness profiles for all cases overlap on to each other. Above this depth ( $y/H = 0.40$ ), the profiles start to deviate among the test cases, since the turbulence of the inverted shear layer generated from the floater has suppressed the characteristics of the boundary layer developing from the bed. For test F1M, the magnitudes of skewness and flatness factors gradually reduce above  $y/H = 0.40$ , whereas these values in other cases continue increasing until they attain the highest magnitudes. The bed-normal coordinates of the highest magnitudes in skewness and flatness profiles are approximately at  $y/H = 0.58, 0.56, 0.51, 0.43$  in test cases F0, F1, F2, F1M, respectively. This reveals the extent of the turbulence penetration of the free surface perturbation towards the bed which is greater with higher perturbation. However, the magnitude of the peak skewness and flatness values are higher than F0 in test case F1 and F2, and lower in F1M. An important parameter to consider is the initial strength of the floater generated turbulence and the domain over which this turbulence is distributed. For example, turbulence generated from the mesh-wrapped floater (F1M) results in relatively greater penetration of the shear layer into the flow (as compared to F1 and F2) and subsequently cause greater mixing in the immediate downstream region of the floater. The window where we are observing the flow is at a far downstream location. Therefore, the floater mesh generated turbulence, before reaching the measuring location gets more evenly dispersed throughout the penetration zone than the regular floaters. Consequently, the level of turbulence mixing in F1M is lower in the FOV and the peak value of skewness is the least among the test cases. This is corroborated with the bed-normal distribution of the flatness factors (figures 3.4c,d), the values of which in case F1M are the closest to three (as compared to other test cases) throughout the depth. The values of the skewness and flatness factors near the free surface are also in clear coherence with the influence of varying degree of free surface perturbations. When the free surface perturbation is generated using the short floater (F1) the magnitude of the skewness factor reduces from the fully developed case at  $y/H \geq 0.8$ , whereas the flatness values are nearly similar. With the increase in perturbation by using the long floater (F2), the skewness values tend to change sign and the flatness values are less than three in the range  $0.8 \leq y/H \leq 1.0$  for  $S_u$ ,  $0.68 \leq y/H \leq 0.82$  for  $S_v$ ,  $0.7 \leq y/H \leq 0.9$  for  $F_u$  and  $0.75 \leq y/H \leq 0.92$  for  $F_v$ , which indicates the crossover between the coherent events, i.e. ejections to sweeps or vice versa (Gad-el-Hak and Bandyopadhyay, 1994). A similar phenomenon is also observed in the bed-normal distribution of  $S_u$  and  $F_u$  in the case of F1M. This alteration of the turbulent coherent events is investigated using the joint probability distribution of velocity fluctuations and presented in Section 3.4. Also it is worth noting that there is a sudden increase in the values of  $F_v$  very close to the free surface, which is visible in all test cases. This is caused by the effect of vertical confinement of the free surface and it is also prominent in absence of the floater (test case F0).

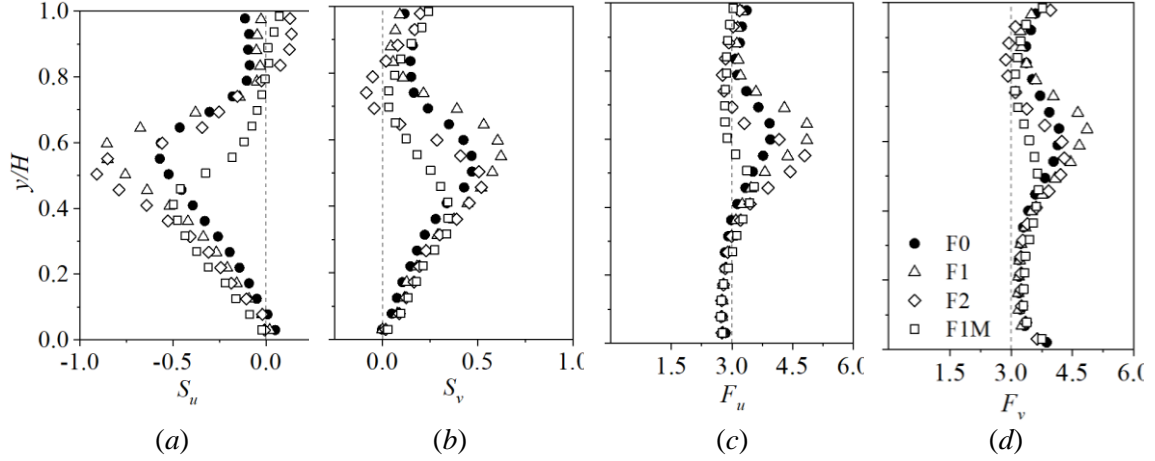


Figure 3.4. Third-order and fourth-order moments of velocity fluctuations in the form of (a,b) skewness factor, (c,d) flatness factor.

The understanding of the turbulence characteristics with free surface perturbation is further substantiated by observing the probability density functions (PDFs) of normalized streamwise velocity fluctuations ( $u'/U$ ) at four bed-normal positions:  $y/H = 0.95, 0.8, 0.6, 0.4$ , which is presented in figure 3.5. In the fully developed case F0, the distribution of probability density ( $P$ ) is narrow at  $y/H = 0.95$ , and the probability density is the highest near  $u'/U = 0$ , indicating the existence of small-scale structures near the free surface. The turbulence length scale increases gradually while moving towards the bed. Consequently, the PDF becomes wider and the probability of occurrence of velocity fluctuations of higher magnitude increases gradually. In the free surface perturbation cases, the PDFs do not follow a similar pattern as seen in the fully developed case. When the perturbation is generated by the smooth floaters, the PDFs have peaks higher than that noticed in F0 at  $y/H = 0.95$  and  $0.8$  in test F1 and between  $y/H = 0.95$  and  $0.6$  in test F2, which demonstrates the alteration of turbulence characteristics. The PDFs in test F1M look alike at  $y/H = 0.95, 0.8$  and  $0.6$  because of the homogeneity in the evenly dispersed turbulence generated from the mesh-wrapped floater. At  $y/H = 0.4$ , PDFs of all four test cases are similar indicating that there is minimal influence of the free surface perturbation at or below this depth.

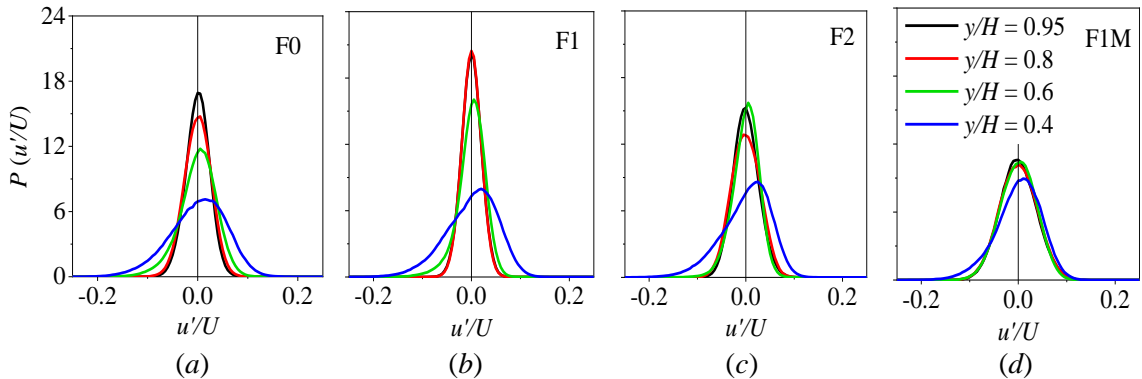


Figure 3.5. Probability density function of streamwise velocity fluctuations at four depths:  $y/H = 0.95, 0.8, 0.6, 0.4$  in test cases (a) F0, (b) F1, (c) F2, (d) F1M.

### 3.3.4. Quadrant analysis

Useful information about the turbulence characteristics can be extracted by exploiting the signs of velocity fluctuations and the most conventional way of doing this is by quadrant analysis. The four quadrants are defined as: Q1 ( $u' > 0, v' > 0$ ), Q2 ( $u' < 0, v' > 0$ ), Q3 ( $u' < 0, v' < 0$ ) and Q4 ( $u' > 0, v' < 0$ ) (Lu and Willmarth 1973, Balachandar and Bhuiyan 2007). Generally, in a fully developed flow field, dominant coherent events belong to the second (ejection) and fourth (sweeps) quadrants. The relatively slow-moving fluid parcel is lifted to the outer layer in the ejection phase and carried away by the outer flow in the sweeping phase. These coherent events corresponding to Q2 and Q4 are the major contributors to the total shear stress production which can be represented as a function of the velocity fluctuations:

$$-\overline{u'v'} = -\int_{-\infty}^{+\infty} \int_{-\infty}^{+\infty} u'v' P(u',v') du'dv' \quad (3.5)$$

where  $P(u',v')$  is the joint probability density function (JPDF) of velocity fluctuations. The JPDF illustrates the distribution of velocity fluctuations in a flow field and correlates it with the coherent events (Wallace 2016). To observe the effect of the floaters, the contours of JPDFs are plotted in [figure 3.6](#) at four different depths ( $y/H = 0.95, 0.8, 0.6, 0.4$ ) which are identified as the zones of relative importance from the discussion of Section 3.3. Since the flow field is reasonably uniform, eleven consecutive streamwise positions in the gridded data are considered for this analysis. Therefore, at each depth, 44 000 instantaneous velocity data are used to obtain better statistics.

The directional preferences of the JPDFs reveal the change in the turbulence characteristics of the flow due to the varying degree of free surface perturbation. These preferences depend on the signs of the velocity fluctuations which provide important information regarding the nature of the coherent events. In the fully developed flow in test F0 (first column of [figure 3.6](#)), the JPDFs at  $y/H = 0.4, 0.6$  and  $0.8$  are strongly skewed towards the second and fourth quadrants, indicating ejection of slow-moving fluid and sweeping of ejected fluid by the high momentum surrounding fluid. Close to the free surface ( $y/H = 0.95$ ), the directional preference becomes weaker and as expected the total shear stress tends to zero. For the test case F1, at  $y/H = 0.95$ , the JPDF shows no strong directional preference, indicating the least production of the shear stress and a transitional nature of shifting of dominant events. With further increment of free surface perturbation (tests F2 and F1M), the directional orientation of JPDFs shifts towards first (outward interactions) and third (inward interactions) quadrants at  $y/H = 0.95$ . The value of shear stresses ( $-\overline{u'v'}$ ) near the free surface becomes negative in test cases F2 and F1M as seen earlier in [figure 3.3](#). A similar characteristic, as seen at  $y/H = 0.95$ , can be found at  $y/H = 0.8$ , except that the respective directional preferences are now stronger in F0, F2 and F1M (second row, [figure 3.6b](#)). At depth  $y/H = 0.6$ , the JPDF contours are strongly oriented towards Q2/Q4 in test F0 and F1, and Q1/Q3 in F1M, whereas the JPDF in test case F2 is mildly skewed to first and third quadrants and nearly lose the directional preference, showing a transition of shear stress from positive to negative near this bed-normal position ([figure 3.6c](#)). Finally, all four test cases show a similar directional orientation of JPDFs at  $y/H = 0.4$ , indicating an absence of any significant influence of the floaters ([figure 3.6d](#)).

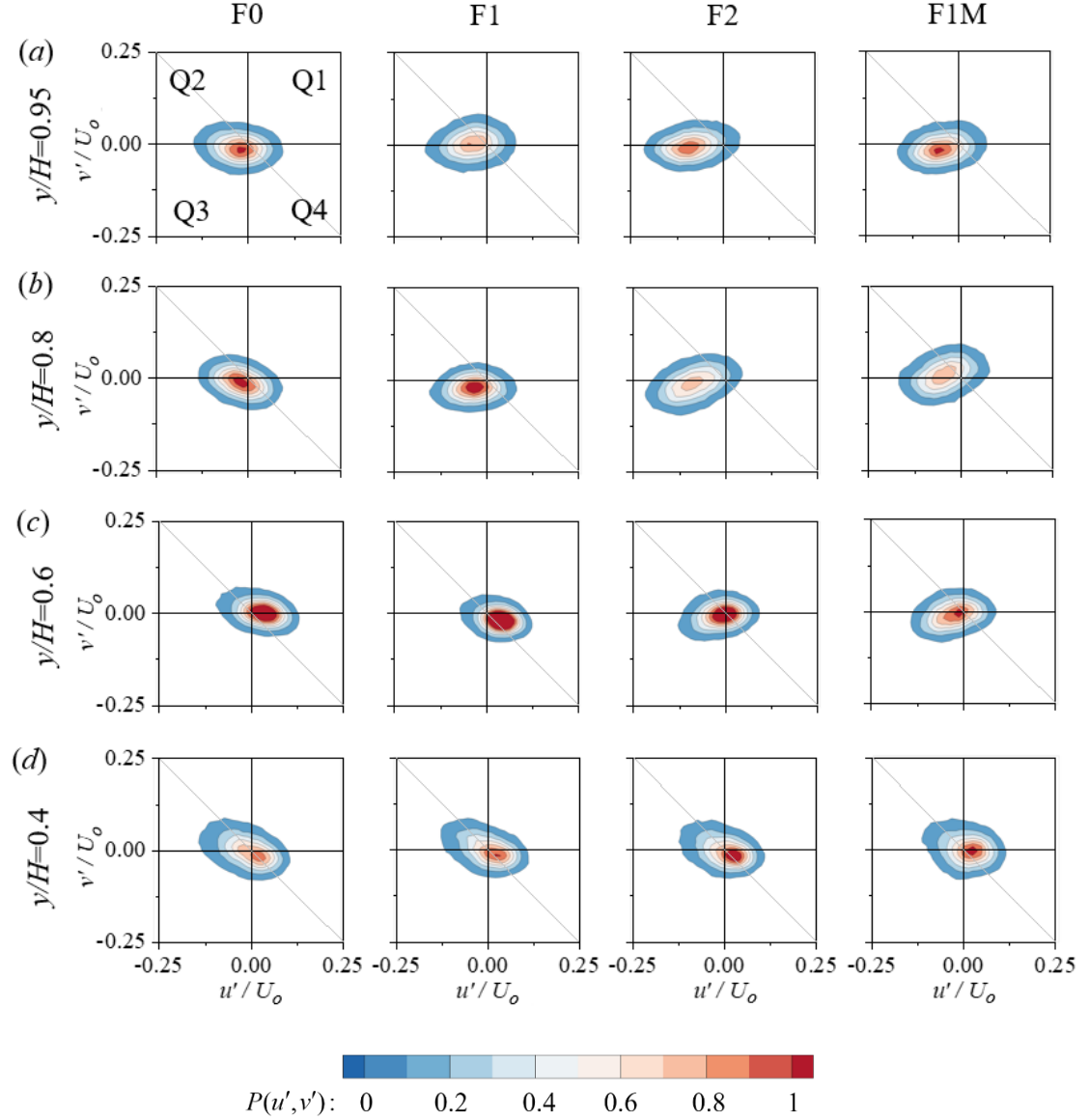


Figure 3.6 Joint probability density function,  $P(u', v')$  in test cases F0 (first column), F1 (second column), F2 (third column) and F1M (fourth column) at  $y/H = (a) 0.95, (b) 0.8, (c) 0.6, (d) 0.4$ .  $P(u', v')$  is normalized in such a way that the maximum probability density is unity.

When the free surface perturbation is added, the flow near the free surface is induced to four types of quadrant events from the bottom boundary layer and the top inverted shear layer. Sweeps and ejections from the floater generated turbulence are opposite in nature to the sweeps and ejections from the bottom boundary layer. The dominant Q1 and Q3 events in tests F2 and F1M are pseudo Q2 and Q4 events generated from the inverted shear layer formed in the bottom of the floaters. However, the dominance of Q1 and Q3 events can only be seen in the zone of shear layer penetration inside the flow and the effects of the free surface perturbations are restricted to the area adjacent to the free surface. The bottom boundary layer dominates the turbulence characteristics

near the bed which is evident from the similarity of the JPDFs in all test cases at  $y/H = 0.4$ . However, the bed is present throughout the test section, whereas the lengths of the floaters are negligible compared to the bed. Therefore, it may appear that the bed generated turbulence should surpass the effects of the floaters at a far downstream location as there is no scope for turbulence regeneration beyond the length of the floaters. But the present experiments show that the perturbation generated from the floaters is sustained over a long distance, which is similar to the wake of a bluff body near the free surface. This is because the turbulence intensity of the bed boundary layer is minimum near the free surface and a small change in turbulence characteristics can become noticeable. Also, the turbulence in the shear layer developed from the floaters is not a random perturbation. The JPDFs of velocity fluctuations show that it has a strong coherence, which prevents it from dissipating faster.

The JPDFs clearly demonstrate that the flow characteristics deviate from the fully developed state with the introduction of free surface turbulence and its effects are prominent far downstream. The shear layer from the floaters can penetrate inside the flow domain and the extent of penetration varies with the level of perturbation. To quantify a depth up to which the influence of the floaters exists, the probability of occurrence of each of the quadrant events was calculated and presented in figure 3.7. In the fully developed case F0, as illustrated in figure 3.7(a), Q2 and Q4 events are dominant similar to what is found in the JPDFs. In the other test cases, the probability of occurrence of Q2 and Q4 reduce near the free surface and finally becomes lower than the probability of occurrence of Q1 and Q3 above  $y/H \approx 0.75, 0.6, 0.5$  for F1, F2 and F1M, respectively. This reconfirms the occurrence of shifting of the dominant quadrant events of the velocity fluctuations and the turbulence penetration of the floater generated shear layer inside the flow.

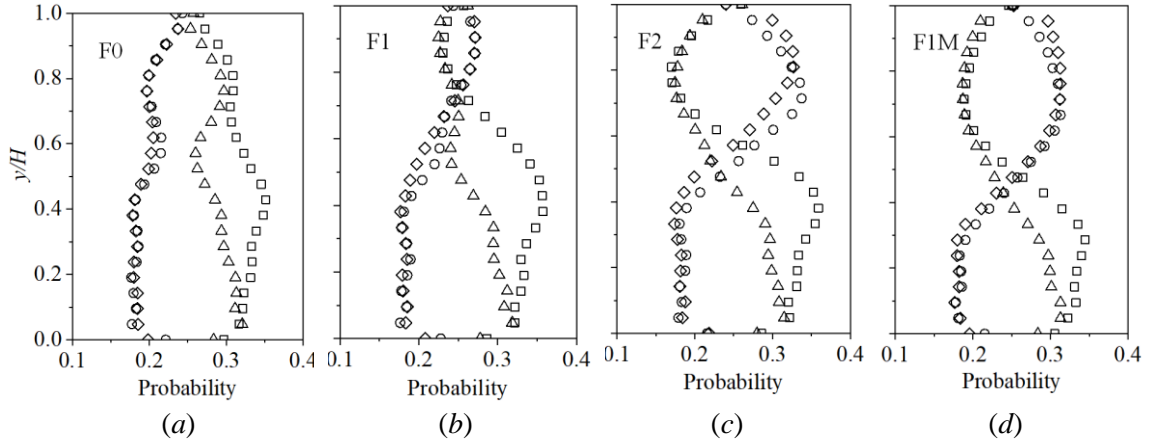


Figure 3.7. Probability of occurrence of the quadrant events in test (a) F0, (b) F1, (c) F2, (d) F1M. ( $\circ$  Q1,  $\Delta$  Q2,  $\diamond$  Q3,  $\square$  Q4)

Further, the shear stress contributions from each of the quadrant events are estimated by the traditional approach of Lu and Willmarth (1973). Reynolds stresses corresponding to each quadrant are categorized based on the signs of the velocity fluctuations and can be calculated as,

$$-\overline{(u'v')}_{Q_i} = -\lim_{T \rightarrow \infty} \int_0^T u'(t)v'(t)I(t)dt \quad \text{for } i = 1 \text{ to } 4 \quad (3.6)$$

where  $I(t)$  is determined based on the quadrant events corresponding to the hole size ( $H_0$ ), i.e.,

$$I(t) = \begin{cases} 1 & \text{when } |u'v'|_Q \geq H_Q u'v' \\ 0 & \text{otherwise} \end{cases} \quad (3.7)$$

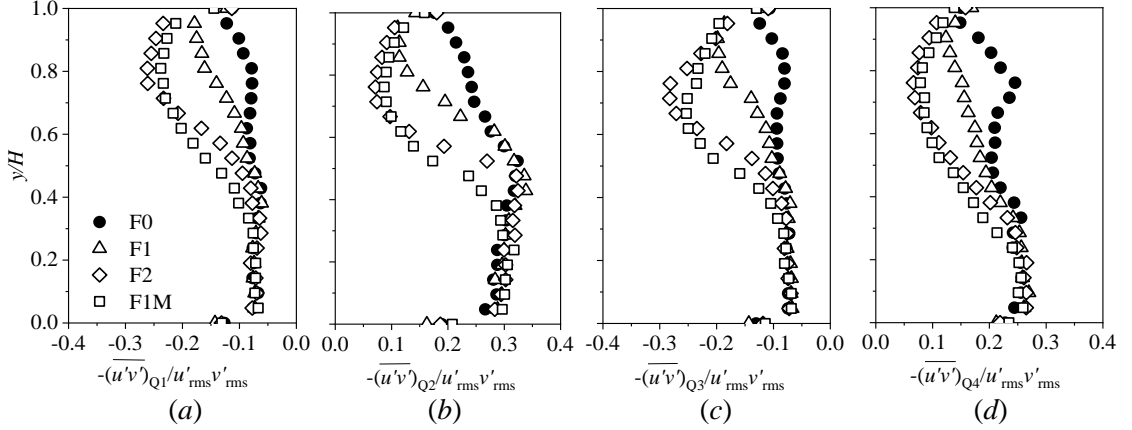


Figure 3.8. Reynolds shear stress contribution from (a) Q1, (b) Q2, (c) Q3, (d) Q4 at each test condition.

The hole size is kept zero to consider the contribution from all events. The bed-normal distribution of the shear stress contributions from each of the quadrant events normalized by  $u'_{rms} v'_{rms}$  (where,  $u'_{rms}$ ,  $v'_{rms}$  are the root-mean-squared velocity fluctuations of streamwise and bed-normal component) and presented in figure 3.8. Similar to the profiles of skewness and flatness factors (figure 3.4), the distributions of Reynolds shear stress from each quadrant show good agreement between all test cases below  $y/H = 0.4$ . Above this depth ( $y/H > 0.4$ ), a clear deviation from the fully developed state is noticed in presence of the floaters and the deviation increases with the level of perturbation. The shear stress distributions show a sudden reduction in magnitude in Q2 and Q4 (figure 3.8b,d), and an increase in magnitude in Q1 and Q3 (figure 3.8a,c) adjacent to the free surface. This indicates a shifting of dominance of coherent events from Q2/Q4 to Q1/Q3, which is similar to what is shown in figure 3.6 and 3.7. In the case of the longer floater (F2) and the mesh-wrapped floater (F1M), the change in the profile is substantial indicating a higher impact of the shear layer penetration than the single floater (F1). Interestingly, no significant difference is observed when the ratio of shear stress contribution from Q2 and Q4 ( $R_{Q2/Q4}$ ) is compared between the test cases (figure 3.9a) and the peak values also occur at a similar location. Since the distribution of shear stress in each quadrant is uniformly influenced by the effect of the floaters (e.g., with the free surface perturbation, the shear stress contribution near the free surface reduces for both second and fourth quadrant events), the difference between the test cases is not clearly visible in the ratio  $R_{Q2/Q4}$ . Therefore, we have calculated the combined shear stress contribution from (Q2+Q4) and (Q1+Q3) events, the ratio of which ( $R_{Q2+Q4/Q1+Q3}$ ) enables us to see the effects of quadrant event switching. Figure 3.9(b) shows that the value of  $R_{Q2+Q4/Q1+Q3}$  is less than one adjacent to the free surface when the free surface perturbation is introduced. In the test case F1, this position is near  $y/H = 0.75$ , whereas it is at  $y/H = 0.57$  and  $0.5$  in cases F2 and F1M, respectively. These are the locations above which event switching occurs. The validity of the ratio  $R_{Q2+Q4/Q1+Q3}$  is re-established by the distribution of the Reynolds stress anisotropy tensor ( $b_{ij}$ ), which can be estimated as (Lumley 1979):



$$b_{ij} = \frac{\overline{u'_i u'_j}}{2k} - \frac{\delta_{ij}}{3} \quad (3.8)$$

where  $(b_{ij})$  is a symmetric tensor bounded by  $[-1/3, 2/3]$ ,  $i$  and  $j$  are the directional indices,  $\delta_{ij}$  is the Kronecker delta function and  $k$  is the turbulent kinetic energy. The value of  $k$  can be obtained as  $k = 0.5 \left( \overline{u'^2} + \overline{v'^2} + \overline{w'^2} \right)$ , where  $w'$  is the spanwise velocity fluctuation. Since planar PIV measurements have been carried out to acquire the streamwise and bed-normal components of the velocity data, the value of  $\overline{w'^2}$  is not available and is therefore approximated by using the formulation of Roussinova *et al.* (2009):

$$\overline{w'^2}^{1/2} = 0.4 \left[ \overline{u'^2}^{1/2} + \overline{v'^2}^{1/2} \right] \quad (3.9)$$

This equation was also validated with the results of Nezu and Nakagawa (1993) and Leonardi *et al.* (2004). The bed-normal distribution of shear stress component  $(-b_{12})$  of  $(b_{ij})$  is presented in figure 3.9(c), which resembles to the profiles of  $R_{Q2+Q4/Q1+Q3}$  since the anisotropy is directly related to the distribution of shear stresses and reveals any alteration of the turbulence characteristics in the flow field. The value of  $-b_{12}$  tends to become zero close to the bed and free surface indicating isotropic turbulence in these regions. The profiles of  $-b_{12}$  are in good agreement among the test cases in the range:  $0 < y/H < 0.4$  and the value of  $-b_{12}$  is greater than zero throughout the depth in the fully developed flow. With the introduction of the free surface perturbation, the value of  $-b_{12}$  becomes less than zero near the free surface. The anisotropy tensor changes the sign at varying bed-normal positions based on the intensity of the perturbation generated by the floaters, which is in coherence with the figure 3.9(b). It is worth noting that the degree of anisotropy in F2 is higher than that in F1M in the range  $0.67 < y/H < 0.95$ . Therefore, the degree of alteration in the turbulence characteristics is more critical with the longer floater although the turbulence penetration of the floater generated shear layer is the largest in case of the mesh-wrapped floater.

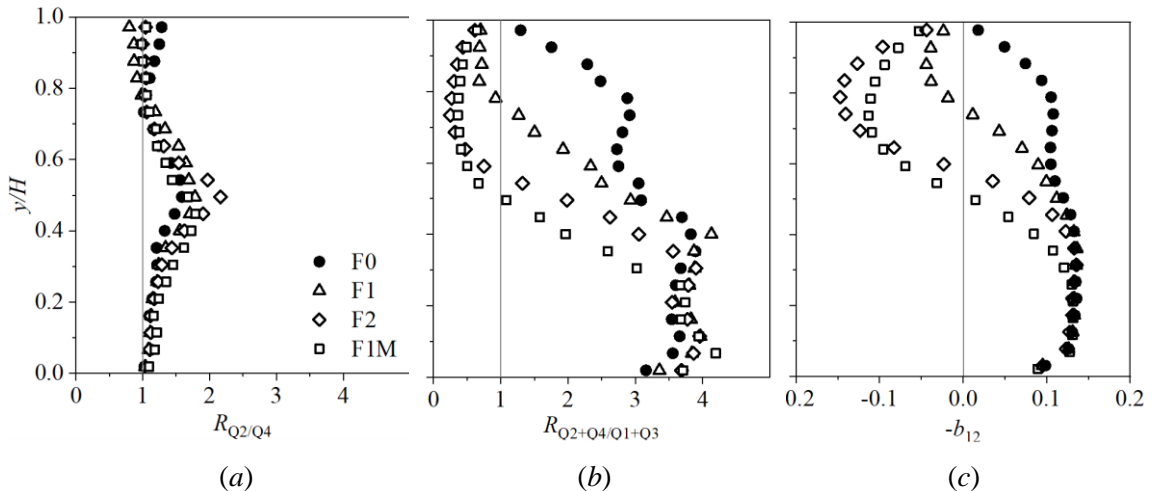


Figure 3.9. Ratio of shear stress contribution from (a) Q2 and Q4 ( $R_{Q2/Q4}$ ), (b) Q2+Q4 and Q1+Q3 ( $R_{Q2+Q4/Q1+Q3}$ ). (c) Shear stress component of Reynolds stress anisotropy tensor ( $-b_{12}$ ).

### 3.4. Summary and conclusions

In this paper, the effect of free surface perturbation is investigated in smooth open channel flows. The free surface perturbation is created by using light floater boards near the inlet section of the flume. Three types of floaters are used: a short floater (F1), a long floater (F2) and a short floater with mesh wrapping (F1M). The results of the perturbed flow are compared against fully developed flow at a downstream section far from the floaters. The shear layer generated from the floaters create a dip in the mean velocity profile near the free surface, which gets larger with the increase in the perturbation intensity (F1 to F1M). This dip indicates the sustenance of the floater induced turbulence in the far downstream, which is also evident in the bed-normal distribution of Reynolds stresses and higher-order turbulence statistics. Near the free surface, the shear stress gradually becomes negative with the increase in perturbation, indicating an alteration of the flow characteristics. The skewness and flatness profiles also show a deviation in turbulence characteristics from the fully developed state when the floaters are added. In the presence of the floaters, the dominance of the Q2 and Q4 events in shear stress generation shifts to Q1 and Q3 events near the free surface, which occurs due to the combined contributions of ejection and sweep events of the inverted shear layer developed from the floaters. The degree of anisotropy in the turbulence characteristics and the extent of shear layer penetration towards the bed vary with the intensity of the free surface perturbation.

Floater boards are widely used in open channel experiments in order to minimize the surface waves. However, the present analysis reveals that this practice may have unintended adverse effects because the approach flow changes remarkably with the addition of a floater. Caution should be exercised, and experiments be preferably carried out without any floaters. If using a floater is unavoidable (e.g., in case of significant unwanted waves and pump generated undulations at the free surface), a short floater can be used far upstream of the test section, possibly before the flow straighteners, and the velocity data should be validated with the fully developed flow profiles.

### References

- Balachandar, R., Blakely, D., Tachie, M. & Putz, G. 2001 A study on turbulent boundary layers on a smooth flat plate in an open channel. *J. Fluids Eng.* **123** (2), 394–400.
- Balachandar, R., Chu, V. H. & Zhang, J. 1997 Experimental study of turbulent concentration flow field in the wake of a bluff body. *J. Fluids Eng.* **119** (2), 263–270.
- Balachandar, R. & Patel, V. C. 2005 Velocity measurements in a developed open channel flow in the presence of an upstream perturbation. *J. Hydraul. Res.* **43** (3), 258–266.
- Balachandar, R. & Tachie, M. F. 2001 A study of boundary layer–wake interaction in shallow open channel flows. *Exp. Fluids.* **30** (5), 511–521.
- Bonakdari, H., Larrarte, F., Lassabatere, L. & Joannis, C. 2008 Turbulent velocity profile in fully-developed open channel flows. *Environ. Fluid Mech.* **8** (1), 1–17.
- Brocchini, M. & Peregrine, D. H. 2001 The dynamics of strong turbulence at free surfaces. Part 1. Description. *J. Fluid Mech.* **449**, 225–254.
- Cameron, S. M., Nikora, V. I. & Coleman, S. E. 2008 Double-averaged velocity and stress distributions for hydraulically-smooth and transitionally-rough turbulent flows. *Acta Geophys.* **56** (3), 642–653.

- Cardoso, A. H., Graf, W. H. & Gust, G. 1989 Uniform flow in a smooth open channel. *J. Hydraul. Res.* **27** (5), 603–616.
- Chauhan, K. A., Monkewitz, P. A. & Nagib, H. M. 2009 Criteria for assessing experiments in zero pressure gradient boundary layers. *Fluid Dyn. Res.* **41** (2), 021404.
- Cimbala, J. M., Nagib, H. M. & Roshko, A. 1988 Large structure in the far wakes of two-dimensional bluff bodies. *J. Fluid Mech.* **190**, 265–298.
- Clauser, F. H. 1956 The Turbulent Boundary Layer. *Adv. Appl. Mech.* (Eds. H. L. Dryden and Th. von Kármán), **4**, 1-51.
- Clift, R., Grace, J. R. & Weber, M. E. 1978 Bubbles, Drops, and Particles. Academic Press, New York, US.
- Coles, D. 1956 The law of the wake in the turbulent boundary layer. *J. Fluid Mech.* **1** (2), 191–226.
- Das, S., Balachandar, R. & Barron, R. M. 2021 Analysis of fully developed state in open channel flow using uniform momentum zones. *J. Fluid Mech.* (under review).
- Flack, K. A., Schultz, M. P. & Shapiro, T. A. 2005 Experimental support for Townsend's Reynolds number similarity hypothesis on rough walls. *Phys. Fluids.* **17** (3), 035102.
- Gad-el-Hak, M. & Bandyopadhyay, P. 1994 Reynolds number effects in wall-bounded turbulent flows. *Appl. Mech. Rev.* **47** (8), 307–365.
- Handler, R. A., Jr, T. F. S., Leighton, R. I. & Swearingen, J. D. 1993 Length scales and the energy balance for turbulence near a free surface. *AIAA J.* **31** (11), 1998-2007.
- Hoffmann, J. A. & Mohammadi, K. 1991 Velocity profiles for turbulent boundary layers under freestream turbulence. *J. Fluids Eng.* **113** (3), 399–404.
- Kirkgöz, M. S. & Ardiçlioğlu, M. 1997 Velocity profiles of developing and developed open channel flow. *J. Hydraul. Eng.* **123** (12), 1099–1105.
- Leonardi, S., Orlandi, P., Djenidi, L. & Antonia, R. A. 2004 Structure of turbulent channel flow with square bars on one wall. *Int. J. Heat Fluid Flow.* **25**, 384–392.
- Li, F. C., Kawaguchi, Y., Segawa, T. & Suga, K. 2005 Simultaneous measurement of turbulent velocity field and surface wave amplitude in the initial stage of an open channel flow by PIV. *Exp. Fluids.* **39** (6), 945–953.
- Lin, J. C. & Rockwell, D. 1999 Horizontal oscillations of a cylinder beneath a free surface: vortex formation and loading. *J. Fluid Mech.* **389**, 1–26.
- Longmire, E. K. & Eaton, J. K. 1992 Structure of a particle-laden round jet. *J. Fluid Mech.* **236**, 217–257.
- Lu, S. S. & Willmarth, W. W. 1973 Measurements of the structure of the Reynolds stress in a turbulent boundary layer. *J. Fluid Mech.* **60** (3), 481–511.
- Lumley, J. L. 1979 Computational modeling of turbulent flows. *Adv. Appl. Mech.* **18**, 126–176.
- Mahananda, M., Hanmaiahgari, P. R., Ojha, C. S. P. & Balachandar, R. 2019 A new analytical model for dip modified velocity distribution in fully developed turbulent open channel flow. *Can. J. Civ. Eng.* **46** (8), 657–668.
- Mignot, E., Hurther, D. & Barthelemy, E. 2011 Discussion of "Double-averaging turbulence characteristics in flows over a gravel bed". *J. Hydraul. Res.* **49** (5), 703–704.
- Nakagawa, H. & Nezu, I. 1977 Prediction of the contributions to the Reynolds stress from bursting events in open channel flows. *J. Fluid Mech.* **80**, 99–128.
- Nasif, G., Balachandar, R. & Barron, R. M. 2020 Supercritical flow characteristics in smooth open channels with different aspect ratios. *Phys. Fluids.* **32** (10), 105102.

- Nezu, I. 2005 Open channel flow turbulence and its research prospect in the 21st century. *J. Hydraul. Eng.* **131** (4), 229-246.
- Nezu, I. & Nakagawa, H. 1993 Turbulence in Open Channel Flows. IAHR Monograph, Balkema, Rotterdam, The Netherlands.
- Nezu, I. & Rodi, W. 1986 Open-channel flow measurements with a laser doppler anemometer. *J. Hydraul. Eng.* **112** (5), 335-355.
- Nikora, V., McEwan, I., McLean, S., Coleman, S., Pokrajac, D. & Walters, R. 2007 Double-averaging concept for rough-bed open channel and overland flows: Theoretical background. *J. Hydraul. Eng.* **133** (8), 873-883.
- Reichl, P., Hourigan, K. & Thompson, M. C. 2005 Flow past a cylinder close to a free surface. *J. Fluid Mech.* **533**, 269-296.
- Roussinova, V., Balachandar, R., & Biswas, N. 2009 Reynolds stress anisotropy in open-channel flow. *J. Hydraul. Eng.* **135** (10), 812-824.
- Roussinova, V., Biswas, N. & Balachandar, R. 2008 Revisiting turbulence in smooth uniform open channel flow. *J. Hydraul. Res.* **46** (sup1), 36-48.
- Sarkar, S. & Dey, S. 2010 Double-averaging turbulence characteristics in flows over a gravel bed. *J. Hydraul. Res.* **48** (6), 801-809.
- Sheridan, J., Lin, J.-C. & Rockwell, D. 1997 Flow past a cylinder close to a free surface. *J. Fluid Mech.* **330**, 1-30.
- Singh, S. K., Raushan, P. K. & Debnath, K. 2018 Combined effect of wave and current in rough bed free surface flow. *Ocean Eng.* **160**, 20-32.
- Steffler, P. M., Rajaratnam, N. & Peterson, A. W. 1985 LDA measurements in open channel. *J. Hydraul. Eng.* **111** (1), 119-130.
- Wallace, J. M. 2016 Quadrant analysis in turbulence research: history and evolution. *Annu. Rev. Fluid Mech.* **48** (1), 131-158.
- Yang, S.-Q., Tan, S.-K. & Lim, S.-Y. 2004 Velocity distribution and dip-phenomenon in smooth uniform open channel flows. *J. Hydraul. Eng.* **130** (12), 1179-1186.

## CHAPTER 4

### QUANTIFICATION OF THE WAKE OF A WALL-MOUNTED FOAM-COVERED CIRCULAR CYLINDER

The wake characteristics of wall-mounted finite solid and foam-covered circular cylinders (height/diameter = 0.9) are explored experimentally using PIV and numerically using LES at a depth Reynolds number of 35 100. The foam-covered cylinder consists of an inner cylinder wrapped by a highly porous foam which is enclosed by a top and base plate. The height and the outer diameter of both cylinders are the same. It is found that the streamwise extent of the reverse flow region is longer for the foam-cover cylinder. Close to the cylinder, the width of the reverse flow region of the foam-covered cylinder is narrower than the solid cylinder and of the order of the diameter of the inner cylinder. An asymmetric vortex generation can be seen in the mid-horizontal plane due to asymmetry in the foam structures. The reattachment line on the top surface of the foam-covered cylinder is a curved line whereas it is a straight line for the solid cylinder. The temporal distribution of the coefficient of sway shows an oscillating nature in the wake of the solid cylinder, which is not prominent in case of the foam-covered cylinder. The coefficient of drag of the foam-covered cylinder is found to be higher than for the solid cylinder. The FFT analysis shows two dominating frequencies for the solid cylinder but no dominating frequencies can be found for the foam-covered cylinder. Finally, SPOD modes are presented in order to substantiate our findings of a longer and asymmetric wake region of the foam-covered cylinder.

**Keywords:** Turbulent boundary layers, Turbulence control, Vortex dynamics.

#### 4.1. Introduction

##### *4.1.1. Motivation*

The flow around surface-mounted submerged circular cylinders has received considerable attention from fluid dynamists due to its wide range of practical relevance and industrial applications. Examples of such flow includes atmospheric boundary layer flow around urban buildings, wind turbine masts, chimney stacks, trees, pantographs of high-speed trains, rockets on a launchpad, ocean currents on offshore structures, oil platforms, submarine periscopes and heat exchangers. Most importantly, a better understanding on this type of flow field can have direct implications in preserving nature and protecting marine ecology. Aquatic plantation creates resistance to the flow, reduces the length scale of turbulence and controls nutrient transport (Ghisalberti and Nepf, 2009) which makes it suitable as a shelter and habitat for fishes and other micro or macro aquatic organisms (Kemp, Harper & Crosa 2000). A study of the flow around these plantations requires a physical model for any experimental or computational research, which have been, so far, simplified as a single (Heidari 2016) or array of cylinders (Chang and Constantinescu 2015, Taddei *et al.* 2016, Nicolai *et al.* 2020) to the best knowledge of the author. In the present study, a wall-mounted circular cylinder covered by a highly porous foam is used to generate a flow field that may represent that around vegetation. The inner circular cylinder can be considered as

the stem of a plant, whereas the foam structures are a simplified form of the branches. However, the flow past foam-covered cylinders can also be applicable to various industrial applications, such as in filters, mixers and heat exchangers (Bhattacharyya *et al.* 2006). In the context of its application in the field of heat transfer, Abdi *et al.* (2017) mentioned that foam-covered cylinders can be a good alternative to finned cylinders since they can provide more efficient heat transfer due to a much larger surface area. The foam coating also reduces the frequency of vortex shedding in the wake of a cylinder (Abdi *et al.* 2014) and breaks up the large-scale flow structures which increases its potential to be used in various man-made civil engineering structures. For example, a foam scaffolding around the bridge piers can provide a resting place for fish and other water habitants, and likely to protect the piers by reducing scour and breaking up the large-scale flow structures. Despite the fairly large scope of applicability, the details of turbulence characteristics and coherent flow structures formed around a foam-covered cylinder are not well-explored. As a matter of fact, studies on foam-covered cylinders are scarce and these studies are mostly confined to the evaluation of the efficiency of infinite cylinders with dense metal foam wrapping in heat transfer applications (Bhattacharyya *et al.*, 2006, 2011; Odabae *et al.* 2011; Abdi *et al.* 2014, 2017). Therefore, the aim of the present study is to visualize the flow field around a foam-covered cylinder, identify the variability in the coherent structures compared to a solid cylinder wake.

#### 4.1.2. Literature review

The flow around an infinite cylinder can be considered as two-dimensional since it is mostly guided by one geometric length scale which is the diameter of the cylinder. But the flow around a submerged finite cylinder creates a highly three-dimensional wake and is dominated by two length scales: height ( $h$ ) and diameter ( $d$ ) of the cylinder, the ratio of which is known as the cylinder aspect ratio. The wake characteristics of finite solid cylinders are explored for a wide range of aspect ratios by several researchers (Kawamura *et al.* 1984, Okamoto and Sunabashiri 1992, Sumner 2013, Porteous *et al.* 2014, Essel *et al.* 2021). In the context of the present research with  $h/d = 0.9$ , our discussion will be mostly concentrated on the wake characteristics of cylinders with low aspect ratio, i.e., cylinders for which the aspect ratio is less than a critical value. As identified in the literature, this critical aspect ratio can vary between one to seven depending on the boundary layer thickness relative to the height of the cylinder (Sumner 2013, Essel *et al.* 2021). Therefore, the cylinders used in the present study can be safely assumed as cylinders with low aspect ratio. The wake characteristics of a low aspect ratio cylinder is different than that of a high aspect ratio cylinder in terms of length of the reverse flow and recirculation region, location of reattachment points, presence of saddle point, etc. A more prominent distinction between the high and low aspect ratio cylinders can be seen in the coherent flow structures. The main difference can be identified in the formation of a von Karman vortex street. In the wake of the high aspect ratio cylinder, a periodic von Karman vortex shedding can be seen from either edge of the cylinder, which turns into a symmetric vortex pair from both sides of the cylinder and joins at the top to form an arch-shaped vortex shedding (denoted by 2 in figure 4.1) (Pattenden *et al.* 2005, Essel *et al.* 2021). A difference can be found in the horseshoe vortex system as well. The approach flow to a cylinder encounters high stagnation pressure in front of the cylinder and gets deflected either upward or downward (denoted by 8 in figure 4.1). The rolling motion of the downward flow at the base of the cylinder creates the horseshoe vortex structure which gets extended on the sides of the cylinder (denoted by 1 in figure 4.1). At higher aspect ratio, formation of primary and secondary horseshoe vortex

systems can be seen around the base of the cylinder. But the secondary horseshoe vortices may not be visible in case of low aspect ratio cylinders. The fluid particles that were deflected upward by the stagnation pressure gets separated at the upstream leading edge of the cylinder and reattaches on the top surface of the cylinder (denoted by 12 in figure 4.1). The distance of reattachment also varies with the aspect ratio of the cylinder. As mentioned by Sumner *et al.* (2015), the reattachment length increases with the increment in the aspect ratio for aspect ratio less than one, whereas this length decreases with the increment of aspect ratio when aspect ratio is greater than one. Several well-defined vortical structures can also be seen on the top of the cylinder, such as tip vortex, free end arch vortex, leading-edge vortex (denoted by 3, 5, 6, respectively in figure 4.1), etc. Further details on the different flow structures around a finite cylinder have been provided by Pattenden *et al.* 2005, Krajnović 2011 and Essel *et al.* 2021 and discussion is not included here for brevity.

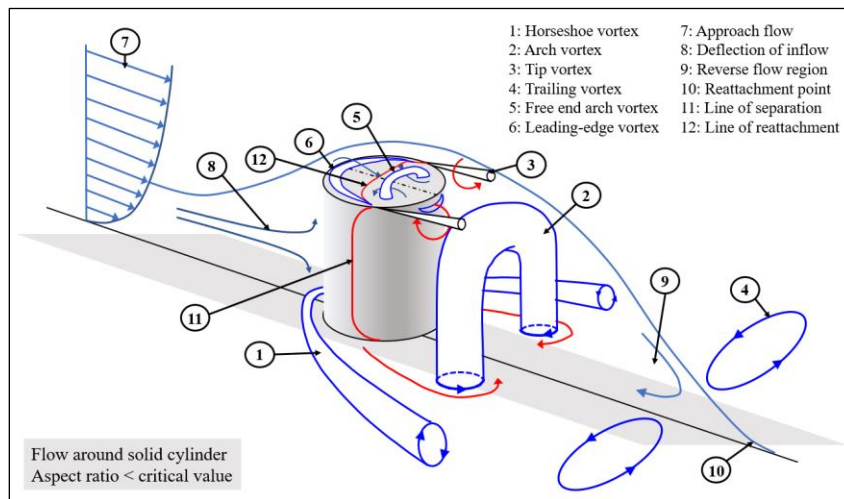


Figure 4.1. Schematic diagram of important flow features of a flow around a surface mounted low aspect ratio circular cylinder. (Adapted from Pattenden *et al.* 2005, Krajnović 2011 and Sumner 2013)

Three-dimensional coherent flow structures around a finite length cylinder can cause flow induced oscillations resulting in higher wind-loading which can affect the integrity of the structures and can cause failures in extreme conditions. Several active and passive flow controls have been implemented in order to eliminate these issues. Active flow control systems such as flow actuators, synthetic jets, additional rotating cylinders are mostly built with complex mechanical instruments and requires an external source of power. On the other hand, passive flow controls such as a splitter plate, base plate, cavity and surface roughness can be less complex, less resource extensive and less expensive. Adding a coating of foam on a cylinder is another simple but efficient way of passive wake control. It can protect the solid structure by creating an intermediate flow region which isolates the solid body from the oscillating wake (Yuan *et al.* 2016). The porous media can be very effective in breaking up the large-scale vortical structures and reduce the frequency of vortex shedding, thus minimizing the flow induced vibration of a structure (Bruneau *et al.* 2006, Bhattacharyya *et al.*, 2011). As suggested by Sueki *et al.* (2010) and Liu *et al.* (2014), the porous

coating can also be used to reduce aerodynamic noise. Abdi *et al.* (2014, 2017) have conducted a comparative study on the flow and heat transfer characteristics between a solid, a finned and a foam-covered cylinder of similar outer diameter. The cylinders were placed horizontally in the wind-tunnel, and treated as infinitely long. They have reported a longer, asymmetric wake region downstream of the foam-covered cylinder compared to the solid cylinder. Further, they observed that the magnitude of the three dimensionality of the flow behaviour in the  $x$ - $z$  plane was higher than that in the  $x$ - $y$  plane (where  $x$ ,  $y$ ,  $z$  are the streamwise, wall-normal and transverse direction).

More directly relevant research can be found in the studies of Zong and Nepf (2012), Chang and Constantinescu (2015), Taddei *et al.* (2016), Nicolai *et al.* (2020) who have investigated the wake characteristics of a fully submerged surface-mounted patch of array of cylinders by varying the porosity (aspect ratio = patch height/diameter = 1). The packing density is measured in the form of a ratio of the area covered by the cylinders and the total patch area ( $\phi$ ). Zong and Nepf (2012) reported a steady near-wake region (in the immediate downstream of the cylinder) with a uniform distribution of longitudinal velocity. This was followed by a flow recovery region wherein the longitudinal velocity increased in streamwise direction. It was observed that the length of these regions increases when the porosity is higher (i.e., when  $\phi$  is low) which indirectly indicates a longer wake region. The von Karman vortex street is only found in case of highly dense array of cylinders (i.e., when  $\phi$  is high) since they mostly act like a single unit. In their comprehensive study on a array of cylinders, Taddei *et al.* (2016) observed that the magnitude of drag coefficient increased with an increase in  $\phi$  (up to the maximum achievable value of  $\phi = 0.24$ ), but then decreased for the solid cylinder which is ideally a representation of  $\phi = 1$ . In fact, they have reported higher coefficient of drag than the solid cylinder in all test cases except for the lowest value of  $\phi$ . On the contrary, the drag force for a porous media or a cylinder with a porous coating is reported to have lower coefficient of drag by Bhattacharyya and Singh (2011) and Hasegawa and Sakaue (2020). This discussion reveals the intricacy in the flow characteristics in the presence of a porous media and seeks further investigation on this matter.

In the present study, wake characteristics of a finite foam-covered circular cylinder is explored in contrast to the wake of a solid cylinder with a similar dimension. The wake study is carried out experimentally using Particle Image Velocimetry (PIV) and computationally using Large Eddy Simulation (LES) under a fully developed open channel flow. A comparison is made based on the mean and turbulent flow variables, width and length of the wake region, frequency response and coherent flow structures. The paper is organised into seven sections: §4.2 and 4.3 are dedicated to the experimental and numerical methodology and their validation. §4.4 explores the instantaneous coherent structures using  $\lambda_2$  criteria, §4.5 describes the mean and turbulent wake characteristics, §4.6 is devoted to the frequency analysis, §4.7 presents the orthogonal decomposition of the flow field to reveal the structured and coherent vortex formation and §4.8 is the conclusion.

## 4.2. Methodology

### 4.2.1. Geometry of the solid and foam-covered cylinders

The geometries of the solid and foam-covered cylinders were generated using open-source software ParaView and Blender. The solid cylinder has a diameter ( $d$ ) of 0.05 m and a height ( $h$ ) of 0.044 m, giving an aspect ratio ( $h/d$ ) of 0.9. The foam geometry was produced following a previously validated approach, the details of which can be found in Abishek *et al.* (2017, 2018).



The geometric properties of the open-cell foam were set in order to generate a highly porous structure (95%) considering its intended practical relevance and potential industrial applications. For example, a foam structure with high porosity will not interrupt the overall fluid discharge of a system but can provide a much higher surface area which can yield more efficient heat transfer than a solid cylinder. A schematic diagram of the foam-covered cylinder is presented in figure 4.2(a) and a cross-sectional view with a 90° cut-out is shown in figure 4.2(b). The foam cylinder consists of four parts: an inner solid cylinder, an annular foam structure, a top plate and a bottom plate. The inner solid cylinder has a diameter ( $d_i$ ) of 0.022 m and is covered with the foam structures keeping the outer diameter equal to  $d$ , i.e., the same for both the solid and foam-covered cylinders. The top and bottom plates have a thickness of 0.0025 m. The polydispersity of the foam structures is compared with previous literature in figure 4.2(c) (White *et al.* 1970, Kraynik *et al.* 2004, Montminy *et al.* 2004). The CAD geometry was directly used in the numerical modelling, whereas the experimental study was conducted using a model which was fabricated using an ‘Ultimaker S5’ 3D printer at the Centre of Engineering Innovation, University of Windsor. The printer is capable of producing accurate and stable 3D models made of ABSplus plastic with a resolution of 0.1 mm (1/20th of the diameter of a single strut of the foam structure).

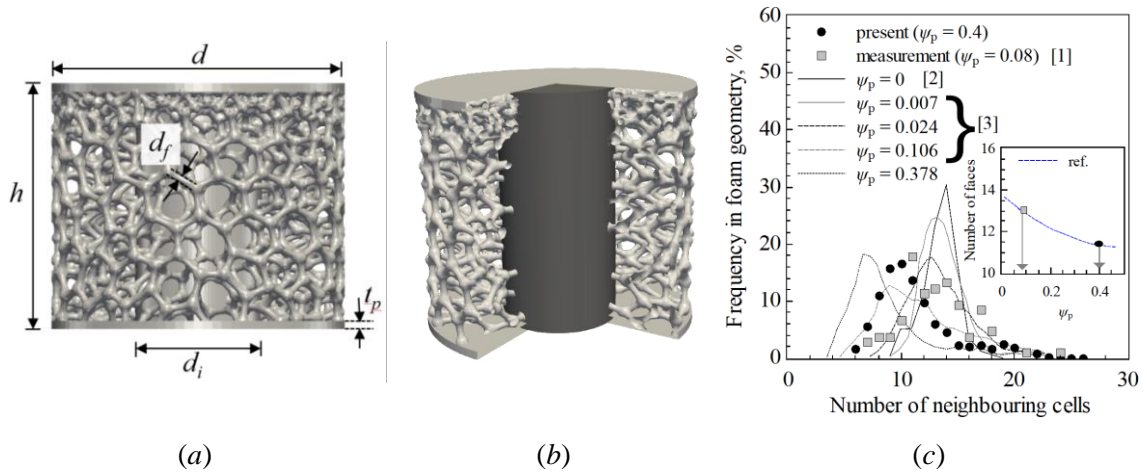


Figure 4.2. Geometry of the foam-covered cylinder: (a) front view, (b) cross-sectional view with a 90° cut-out.  $d$  and  $d_i$ : outer and inner diameter of the cylinder, 0.05m and 0.022m, respectively,  $d_f$ : thickness of a single strut of the foam structure, 3 mm,  $t_p$ : thickness of the base and the top plate, 5 mm,  $h$ : height of the cylinder, 0.0436 m. (c) polydispersity index and the distribution in the number of pores per cell in the foam. [1]: Montminy *et al.* (2004), [2]: White and Vlack (1970), [3]: Jaganathan *et al.* (2008).

#### 4.2.2. Experimental methodology

The experiments were carried out in a recirculating open channel flume (figure 4.3a) located at the Hydraulic Engineering Research Laboratory. The flume has a length of 16 m with a rectangular cross-section of width 1.2 m and depth 0.8 m. The side and bottom walls are made of transparent glass to provide optical access. The upstream settling tank minimizes the inflow perturbations and the honeycomb flow straighteners with variable circular cross-section are placed at the inlet to gradually eliminate any external perturbation and to manage the inflow turbulence level. The tailgate at the downstream end of the flume creates a free-fall into the downstream settling tank and

controls the depth of the water in the flume. The pump was operated at a constant frequency to maintain a constant flow Reynolds number  $Re_H = U_o H / \nu = 35\ 100$ , where  $U_o$  is the depth-averaged inflow velocity,  $H$  is the flow depth,  $\nu$  is the kinematic viscosity of water. The inlet flow was adequately tripped with roughness elements installed at the floor of the flume to stimulate a fully developed approach flow at the measuring station. A fully developed approach flow is mandatory to maintain commonality and consistency among different experimental facilities. The details of the trips and the process of conditioning the approach flow are provided in Das *et al.* (2021a,b). The aspect ratio of the flow (width of flume/depth of water) is nine, which is large enough to eliminate any influence of secondary currents in the measuring planes (Nakagawa & Nezu 1977). In an extensive study on open channel flows at variable aspect ratios, Nasif *et al.* (2020) suggested that there exists a section of fairly two-dimensional flow and minimal spanwise variations over the mid 80% of the flume width when the aspect ratio is larger than five. Since the cylinders were placed at the centre of the flume and the measurement planes span up to the radius of the cylinder from the centre of the flume, it can safely be assumed that any influence of secondary flow is negligible. Both the solid cylinder and the foam-covered cylinder were fully submerged and the free surface height was approximately three times the height of the cylinders. The blockage ratio of the flow is  $d/B = 0.04$ , where  $B$  is the channel width. The origin of the coordinate system was taken at the centre of the cylinder on the bed. The axes in the streamwise, depthwise and spanwise directions are presented as  $x$ ,  $y$ ,  $z$ , respectively. The velocity measurements were carried out in six fields-of-view on the  $x$ - $y$  plane with a streamwise extent of  $4d$ , consisting of one upstream plane (P0) and two downstream planes (P1 and P2) as shown in figure 4.3(b). The planes P0 and P1 are the mid-vertical planes ( $z/d = 0$ ) whereas the plane P2 is located at the outer edge of the cylinder.

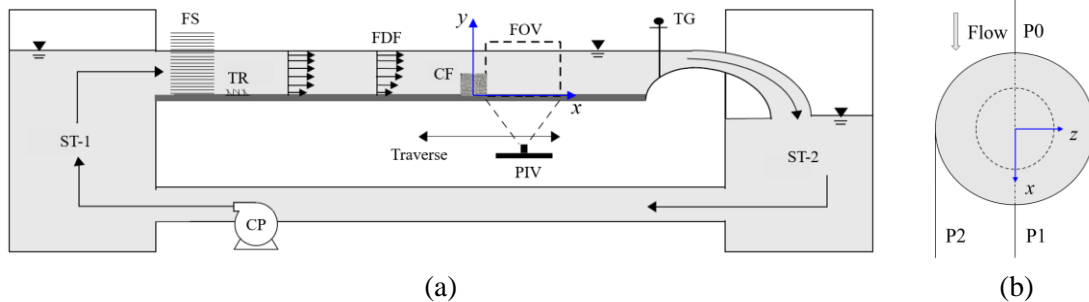


Figure 4.3. (a) Experimental setup. CF: solid cylinder or foam-covered cylinder, CP: central pump, FS: flow straighteners, FDF: fully developed flow, PIV: particle image velocimeter, ST-1,2: upstream and downstream settling tanks, TG: tail gate, TR: inflow tripping. (b) top view of the cylinder showing the measurement planes. The dashed line represents the inner cylinder.

Velocity measurements were carried out in the vertical planes ( $x$ - $y$  plane) using a two-component planar PIV system that consists of dual pulse Nd:YAG lasers of 532 nm wavelength and 50 mJ/pulse with a maximum output of 800 mJ. Each laser pulse duration was 4 ns and time between two pulses was set to be 2.3 ms. The laser emitter box was orthogonally placed underneath the flume to illuminate the flow from the bottom. Two cylindrical lenses with focal lengths of -15 mm and -25 mm were attached at the laser outlet to stretch the beam into a vertical laser sheet. A spherical lens (focal lengths of 1000 mm) was mounted at the top of the cylindrical lenses, to maintain equal intensity at the edges of the laser sheet. A PowerViewPlus 8 MP CCD camera was installed on one side of the flume and aligned parallel with the laser sheet. Nikon AF NIKKOR

50mm f/1.8D lens was used to acquire the images of resolution 3320 pixels  $\times$  2496 pixels. The camera was operated in dual capture mode synchronized with the laser pulse repeat frequency of 2.9 Hz. Before starting the experiment, the flume water was circulated through a sand filter for several days to remove unwanted particles from the tap water. The flow was then seeded with 10  $\mu\text{m}$  spherical silver-coated hollow glass spheres with an effective density of 1100 kg/m<sup>3</sup>. The particles' Stokes number ( $St_p$ ) was calculated to check the ability of the particles to follow the flow.  $St_p$  was determined by the ratio of particle response time to turbulent time scale (Longmire & Eaton 1992) and was evaluated as  $5.31 \times 10^{-5}$  which satisfies the criterion proposed by Clift *et al.* (1978):  $St_p \ll [2(\rho_p / \rho) + 1] / 9 = 0.36$ . Four thousand image pairs were taken for each test condition and analyzed using PIVlab (Thielicke & Stamhuis 2014). After background subtraction, the images were pre-processed using the Contrast-Limited Adaptive Histogram Equalization (CLAHE) technique (Pizer *et al.* 1987). Intensity capping and Wiener denoise filtering were used to minimize the error. The particle illuminations between image pairs were correlated by the Fast Fourier Transform (FFT) window deformation algorithm where the interrogation window of 64 $\times$ 64 pixels was reduced to 16 $\times$ 16 pixels with a spatial overlap of 50%. The velocity data (spatial resolution of 1.3 mm) were then post-processed in PIVlab using standard deviation and median filters with a predefined threshold value to remove and replace bad vectors. Less than 7% of vectors were identified as bad and replaced by interpolated vectors. MATLAB codes were developed for analyzing the experimental data. The overall uncertainty in mean velocity ( $U$ ) measurement is  $\pm 2\%$  of  $U_o$ . Statistical analysis of the data shows that four thousand images are adequate to calculate the higher-order moments with uncertainties of  $\pm 2\%$ ,  $\pm 2\%$ ,  $\pm 2.5\%$  in Reynolds stresses  $\overline{u'^2}$ ,  $\overline{v'^2}$  and  $-\overline{u'v'}$ , respectively. The uncertainty analysis is discussed in detail in Chapter 2 and in Das *et al.* (2021a) and not repeated here for brevity.

### 4.2.3. Computational methodology

#### 4.2.3.1. Computational domain and mesh

The computational domain is  $19d$  in length ( $7d$  and  $12d$  upstream and downstream of the cylinder, respectively) and  $10d$  in width ( $5d$  on each side of the cylinder) for both the solid and foam-covered cylinder (figure 4.4a). The height of the domain is the water depth  $H$  in both cases which is nearly three times the cylinder height. The number of mesh cells is approximately 10 and 15 million, for the case of the solid cylinder and foam-covered cylinder, respectively. The time step size is  $0.005d/U_o$  and the cell size varies between  $0.00625d$  to  $0.05d$  corresponding to the Courant number less than or equal to one. In figure 4.4(b), the mesh around the foam structure is shown and four prism layers are provided around the cross-section of each strut to properly resolve the flow. Inner iterations are carried out at each time step until the absolute equation residual for each variable in the numerical solution is equal or less than  $1 \times 10^{-7}$ . The time-averaging of the flow variables is carried out over a non-dimensional time of  $650d/U_o$ , which corresponds to approximately 35 flow-through cycles over the length of the simulation domain. The boundary condition on the side and top walls of the simulation domain is taken as free-slip wall, whereas the bottom wall and the cylinder or the foam surfaces are considered as no-slip walls. Although the top wall of the domain represents the free surface, a free-slip boundary condition is used since the free surface is fairly steady and no significant fluctuation was noticed during the experiments. The fully developed

profiles of velocity components, Reynolds stresses and turbulent length scale are provided at the inlet and synthetic eddy generation is used for better accuracy. The pressure outlet is used as an outflow condition and the flow variables at the inlet are determined by a separate LES simulation where recycling from outlet to inlet is used to achieve a fully developed state. The same mesh size as used at the inlet of the flow around cylinder simulation is taken throughout the flow domain ( $4H \times 6H$ ) to prevent any inaccuracy generated by the interpolation while imposing the boundary condition.

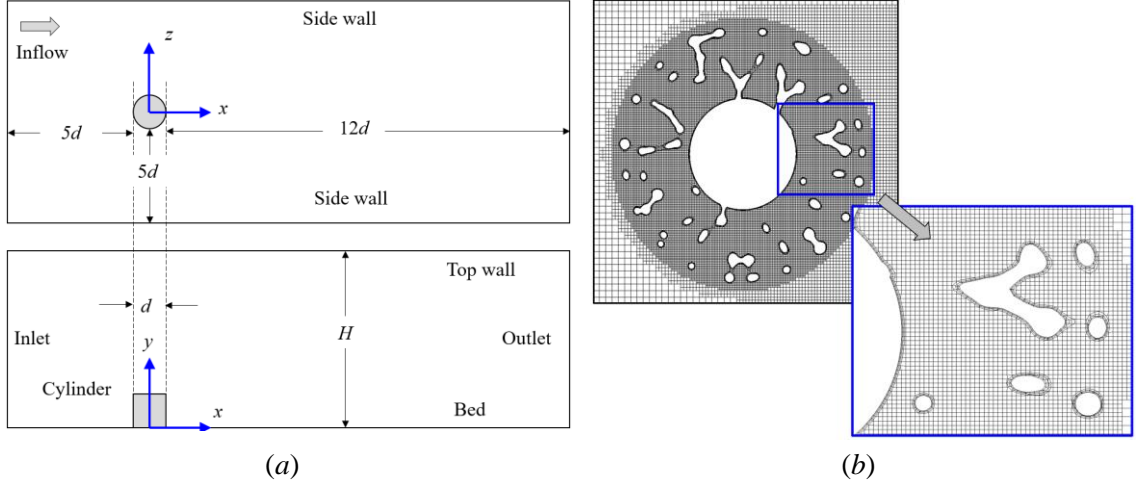


Figure 4.4. (a) Top and front view of the simulation domain, (b) mesh around the foam structures.

#### 4.2.3.2. Mathematical formulations

The dynamics of the flow in this problem is highly three-dimensional and requires a high-resolution numerical modelling to capture the intricate flow details. The turbulent flow is modelled using LES which is governed by the unsteady filtered continuity and Navier-stokes equations which can be presented as,

$$\frac{\partial U_i}{\partial x_i} = 0 \quad (4.1)$$

$$\frac{\partial U_i}{\partial t} + \frac{\partial (U_i U_j)}{\partial x_j} = -\frac{\partial P}{\partial x_j} + \nu \frac{\partial}{\partial x_j} \left( \frac{\partial U_i}{\partial x_j} + \frac{\partial U_j}{\partial x_i} \right) - \frac{\partial \tau_{ij}}{\partial x_j} \quad (4.2)$$

where  $\widetilde{U}$  and  $\widetilde{P}$  are the filtered velocity and pressure,  $\tau_{ij}$  is the sub-grid scale stress which is determined by the dynamic Smagorinsky sub-grid scale model (Lilly 1992) to provide a closure to this system of equations. The magnitude of  $\tau_{ij}$  can be approximated as

$$\tau_{ij} - \frac{1}{3} \delta_{ij} \tau_{kk} = 2\nu_t \bar{S}_{ij} \quad (4.3)$$

where  $\delta_{ij}$  is the Kroecker delta function,  $\nu_t$  is the sub-grid scale eddy viscosity and  $\bar{S}_{ij}$  is the strain rate tensor. The magnitude of  $\nu_t$  can be determined as  $\nu_t = C_s \Delta^2 \bar{S}$  where  $C_s$  is the Smagorinsky

constant,  $\Delta$  is the filter width ( $\Delta = \Delta V^{1/3}$ , where  $\Delta V$  is the volume of a cell) and  $|\bar{S}| = \sqrt{2\bar{S}_{ij}\bar{S}_{ij}}$ . In the dynamic Smagorinsky model,  $C_s$  is a local time varying coefficient on the filtered velocity field which is determined for a length scale greater than the grid length scale. The strain rate tensor  $\bar{S}_{ij}$  is determined over the resolved velocity field as  $\bar{S}_{ij} = 0.5 (\partial U_i / \partial x_j + \partial U_j / \partial x_i)$ .

#### 4.2.3.3. Solution control

An implicit finite-volume algorithm for LES is employed to numerically solve the Navier-Stokes equations using a commercial software package, Siemens Star-CCM+. The algorithm is second-order accurate both in time and space to achieve adequate accuracy and robustness. The convection terms are discretized with a bounded-central scheme with upwind blending factor 0.15. The discretized equations are solved using an Algebraic Multi-Grid (AMG) linear solver with the Gauss-Seidel relaxation scheme, which is an optimized algorithm for faster convergence with less computational cost. LES is an inherently transient technique in which the large-scale turbulences are resolved while the small-scale fluid motions are modeled. As mentioned earlier, the subgrid-scale viscosity of the small-scale turbulence is modelled using the dynamic Smagorinsky model. This distinction between large-scale and small-scale is created by filtering the Navier-Stokes equations, which is directly related to the mesh size of the simulation domain. A grid independence study is practically inefficient to generate an optimized mesh for LES, since the size of the mesh in most cases is taken as the filter cut-off. Therefore, we have followed the methods of Celik *et al.* (2005) and Virani *et al.* (2019), which provide an efficient and systematic way of generating the mesh for LES with the minimum number of iterations. Initially, a preliminary mesh is created with fairly coarse cell size and a simulation is carried out using the Reynolds stress transport model (RSM) in a RANS framework. The pressure strain term is determined by the elliptic blending model, proposed by Manceau and Hanjalic (2002). Finally, the important turbulent length scales such as Taylor micro-scale ( $\lambda = \sqrt{10\nu k/\varepsilon}$ , where  $k$  is the turbulent kinetic energy and  $\varepsilon$  is the turbulent dissipation rate) and Kolmogorov scale ( $\eta = [\nu^3/\varepsilon]^{1/4}$ ) are determined on the trial mesh. A mesh refinement which is capable of resolving the turbulent length scale of the order of  $\lambda$  is theoretically good enough for LES since it can ensure resolving 80% of the total turbulent kinetic energy (Pope, 2000; Celik *et al.*, 2009; Virani *et al.*, 2019). However, these length scales also depend on the grid size ( $\Delta$ ) and the magnitude of  $\lambda$  converges with refinement of the mesh. Therefore, the simulation is continued with refinement of the mesh and  $\lambda$  values are determined for each refinement. This process is repeated until a converged mesh size is achieved with cell size less than  $\lambda$ . The ratio of final mesh size to Taylor micro-scale ( $\Delta/\lambda$ ) at three different depths ( $y/h = 0.2, 0.5, 0.8$ ) on the mid-vertical plane is presented in figure 4.5(a) for the flow around the foam-covered cylinder. The magnitude of  $\Delta/\lambda$  in the wake of the cylinder is less than one throughout the streamwise length of the simulation domain, which indicates that the mesh size is capable of resolving the Taylor micro-scale. The results from the RSM simulation are used as an initial condition and the LES simulation is carried out on the final mesh. The resolution quality of the mesh, as suggested by Celik *et al.* (2005), is determined by three LES indices based on resolved turbulent kinetic energy ( $I_k$ ), Kolmogorov length scale ( $I_\eta$ ) and effective viscosity ( $I_\nu$ ):

$$I_k = k_{\text{res}} / (k_{\text{res}} + k_{\text{SGS}}) \quad (4.4)$$

$$I_\eta = 1 / [1 + \alpha_\eta (\Delta / \eta)^m] \quad (4.5)$$

$$I_\nu = 1 / [1 + \alpha_\nu (\bar{\nu}_{t,\text{eff}} / \nu)^n] \quad (4.6)$$

where  $k_{\text{res}}$  and  $k_{\text{SGS}}$  are the resolved and SGS kinetic energy,  $\Delta$  is the cell size,  $\eta$  is the Kolmogorov length scale,  $\bar{\nu}_{t,\text{eff}}$  and  $\nu$  are the effective (SGS + numerical viscosity) and molecular viscosity. The overbar denotes the time-averaged value and the magnitude of  $\alpha_\eta$ ,  $\alpha_\nu$ ,  $m$ ,  $n$  are 0.05, 0.05, 0.5, 0.53. According to the guidelines provided by Pope (2000) and Celik *et al.* (2005), the values of  $I_k$ ,  $I_\eta$  and  $I_\nu$  for a well-resolved LES simulation should be in a range of 80-95%. These quantities lie between 90-95% in the present study. The validity of the mesh resolution can also be demonstrated by Kolmogorov -5/3 power law (Kolmogorov 1991) in the inertial range. In the present study, turbulence in this length scale is well-resolved by the LES model and the slope of the energy spectra matches with -5/3 (figure 4.5b). Throughout this work, CFD-C, PIV-C, CFD-F and PIV-F refer to CFD and PIV results for the solid and foam-covered cylinders, respectively.

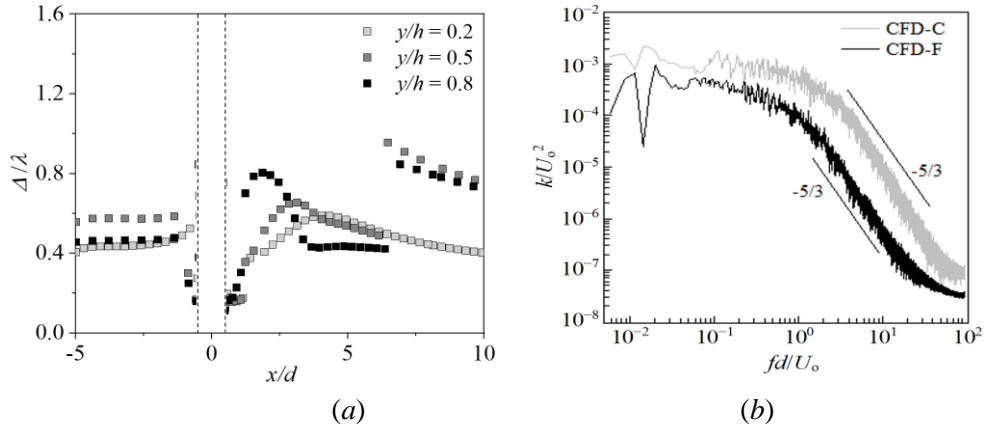


Figure 4.5. (a) The ratio of cell size and Taylor micro-scale ( $\Delta/\lambda$ ) at three different bed-normal positions ( $y/h = 0.2, 0.5, 0.8$ ) for flow around the foam-covered cylinder. The symbols are darker with the increment in the magnitude of  $y/h$ . The position of the cylinder is shown by the dashed lines. (b) Energy spectra of normalized turbulent kinetic energy ( $k/U_o^2$ ) for flow around the solid (denoted as CFD-C) and foam-covered (denoted as CFD-F) cylinder.

### 4.3. Validation

#### 4.3.1. Validation of the approach flow

A fully developed approach flow is achieved experimentally by tripping the near-wall inflow. The Reynolds numbers based on the flow depth ( $H$ ) and the displacement thickness ( $\theta$ ) are 35100 and 3791, respectively. The shape factor of the mean velocity profile ( $\delta^*/\theta$ ) is 1.31, where  $\delta^*$  is the displacement thickness. The Froude number ( $U_o/\sqrt{gh}$ , where  $g$  is the gravitational acceleration) of the flow is maintained as 0.20. Numerically, the fully developed state is achieved by recycling the flow variables from outlet to inlet at a certain interval. The depthwise distributions of the mean flow variables are obtained using a double-averaging technique (Nikora *et al.* 2007; Sarkar & Dey 2010) which involves time and space averaging of velocity data. The spatial averaging is used in order to achieve better statistics of the inflow turbulence parameters and this is valid since the fully developed flow is fairly uniform. It is worth mentioning here that double-averaging is only used in

the approach flow simulation whereas the mean variables for the flow past the cylinders are estimated based on time-averaging. In [figure 4.6\(a\)](#) the mean streamwise velocity distributions of the experimental and the numerical study are presented with inner scaling ( $U^+ = U/U_\tau$ ,  $y^+ = yU_\tau/\nu$ ) and compared with the theoretical log-law profile:  $U^+ = (1/\kappa) \ln(y^+) + B$  (Clauser [1956](#)), where  $U$  is the mean streamwise velocity,  $y$  is the bed-normal coordinate and the value of  $\kappa$  and  $B$  are taken as 0.41 and 5, respectively (Nezu & Rodi [1986](#)). The shear velocity ( $U_\tau$ ) for the experimental data is calculated by an optimization algorithm as presented in Chapter 2 and in Das *et al.* ([2021a](#)) since the velocity data in the viscous sublayer is not available in the experiments. The algorithm is based on linear least squares curve fitting of the experimental data to the log-law curve in the overlapping logarithmic layer:  $30 \leq y^+ \leq 0.2Re_\tau$  where  $Re_\tau = U_\tau H/\nu$  (Balachandar & Patel [2005](#)). In the computational simulation, the value of  $U_\tau$  is estimated using the time-averaged bed shear stress. In [Figure 4.6](#) it can be seen that the simulation agrees well with the experiments and shows good agreement with the theoretical log-law profile.

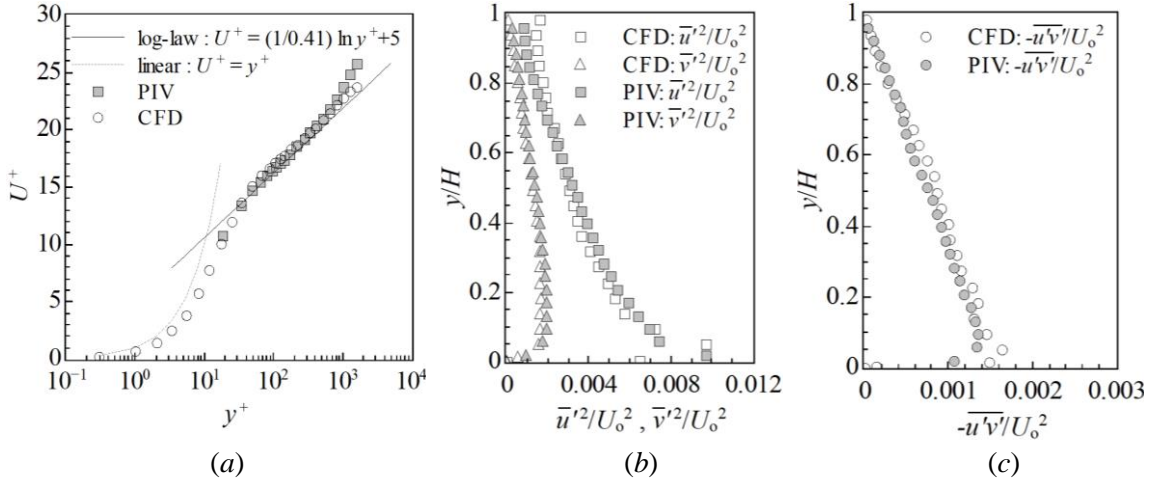


Figure 4.6. (a) Mean streamwise velocity profiles normalized by inner scaling ( $U^+ = U/U_\tau$ ,  $y^+ = yU_\tau/\nu$ ), compared with the theoretical log-law profile, (b,c) normalized Reynolds stresses ( $\overline{u'^2}/U_o^2$ ,  $\overline{v'^2}/U_o^2$ ,  $-\overline{u'v'}/U_o^2$ ).

The Reynolds stresses  $\overline{u'^2}$ ,  $\overline{v'^2}$  and  $-\overline{u'v'}$  are normalized with the depth-averaged streamwise velocity  $U_o$  and presented in [figures 4.6\(b,c\)](#). The CFD profiles of the Reynolds stresses collapse well onto the experimental results throughout the depth of the flow. However, a minor deviation is noticed near the free surface ( $y/H > 0.8$ ) for the distribution of  $\overline{u'^2}/U_o^2$  and close to the bed ( $y/H < 0.1$ ) in case of shear stress distribution  $-\overline{u'v'}/U_o^2$  which can be attributed by the higher uncertainty in PIV measurements in these regions.

#### 4.3.2. Flow around cylinders

Time averaging is used to calculate the mean flow variables which reveal important information regarding the wake characteristics behind the cylinder. [Figure 4.7](#) shows the streamwise variation of the time-averaged velocities  $U$  and  $V$ , and Reynolds stresses  $\overline{u'^2}$ ,  $\overline{v'^2}$  and  $-\overline{u'v'}$  normalized by  $U_o$ , at the mid-height of the cylinder ( $y/h = 0.5$ ) on the central vertical plane ( $z/d = 0$ ). The values of each flow variable are presented in a range of  $-4 \leq x/d \leq 4$  for the experiments and  $-5 \leq x/d \leq 10$

for simulation data. In each case, good agreement between simulation and experimental data is observed, demonstrating the validity and accuracy of the LES simulation. However, a small deviation between the experimental and computational results is noticed in the distributions of  $\overline{v'^2}/U_o^2$  and  $-\overline{u'v'}/U_o^2$  in the immediate downstream of the cylinder ( $-1.5 \leq x/d \leq 3$ ). In this region, the component of in-plane velocity is significantly high and a sharp change in the stress profiles occurs, which may not be effectively captured in experiments due to lower resolution of velocity data and window overlapping in data processing. Considering these uncertainties in the experiments, it can be said that the match between experimental and numerical results is reasonably good.

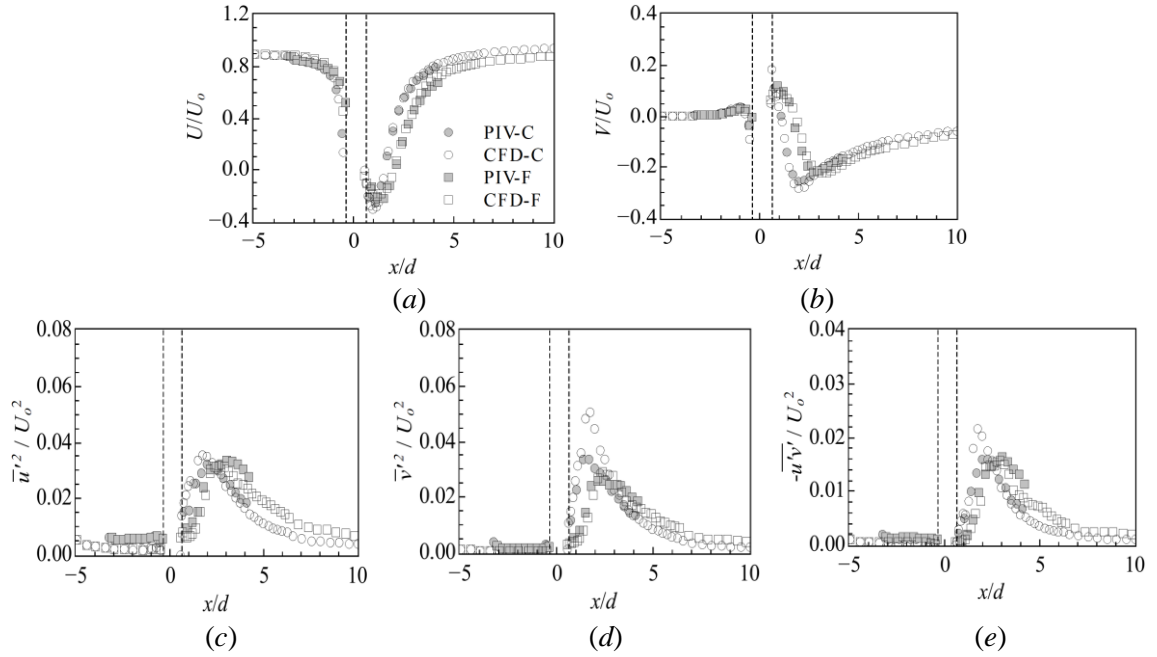


Figure 4.7. Comparison of the experimental and the numerical data: streamwise variation in (a,b) the normalized time-averaged velocities and (c,d,e) Reynolds stresses at mid-height of the cylinder ( $y/h = 0.5$ ).

The streamwise distributions of the time-averaged velocities (figures 4.7a,b) illustrate a good match in magnitude between the solid and foam-covered cylinders at upstream locations, whereas a clear deviation is noticed downstream of the cylinder. In figure 4.7(a), the streamwise component of mean velocity is negative in the range  $0.5 \leq x/d \leq 1.5$  in case of the solid cylinder, while the same is noticed in  $0.5 \leq x/d \leq 2.2$  for the foam-covered cylinder, which indicates the difference in length of the recirculation region between these two cases. The magnitude of  $U/U_o$  is slightly higher in the foam case in the immediate downstream of the cylinder but lower than that for the solid cylinder at  $x/d \geq 1$ . The fluid flows through the foam structure which causes higher magnitude of the streamwise velocity in the central wake region (i.e., near  $z/d = 0$ ) close to the cylinder ( $x/d \leq 1$ ). Moving further downstream ( $x/d \geq 1$ ), the streamwise velocity is higher in case of the solid cylinder because of the shorter length of the recirculation region. The flow in the downstream of the foam-covered cylinder takes a much longer distance to compensate for the velocity deficit. In figure 4.7(b), an opposite trend is noticed in the distribution of bed-normal velocity component which is higher in case of the foam-covered cylinder in the range  $1 \leq x/d \leq 2.7$  and lower than the solid



cylinder beyond this length ( $x/d \geq 2.7$ ). The distribution of  $V/U_o$  is highly influenced by the flow coming from the top of the cylinder, creating a downwash motion near the downstream edge of the top plate. In case of the foam-covered cylinder, this downwash motion is restricted to some extent due to the flow traversing through the foam and the effective cross-sectional area of obstruction of the foam-covered cylinder is much lower than that of the solid cylinder. Therefore, a lower negative value is noticed in the streamwise distribution of  $V/U_o$  in the adjacent wake region of the foam-covered cylinder. The magnitude of the Reynolds stresses is shown in [figures 4.7\(c-e\)](#), and a similar trend is found in each component of the Reynolds stress ( $\overline{u'^2}/U_o^2$ ,  $\overline{v'^2}/U_o^2$ ,  $-\overline{u'v'}/U_o^2$ ). The wake region Reynolds stresses for the solid cylinder are higher than the foam-cylinder wake between  $0.5 \leq x/d \leq 2.7$  and lower at further downstream ( $x/d \geq 2.7$ ). The vortical motion of the fluid coming from the sides and top of the solid cylinder has a higher length scale and creates larger velocity fluctuations in the immediate downstream of the cylinder. In case of the foam-covered cylinder, the length scale of turbulent fluctuations is smaller since the fluid coming through the foam structure affects the von Karman vortex street and also interacts with the flow coming from the top of the cylinder, causing a longer reattachment length. This causes lower Reynolds stresses in the near vicinity of the foam-covered cylinder but higher stresses in the further downstream due to the longer wake region.

[Figure 4.8](#) shows the wall-normal distributions of the time-averaged streamwise velocity and the Reynolds stresses on the central plane ( $z/d = 0$ ) at two representative streamwise positions ( $x/d = 0.75$  and  $2.5$ ) and on a plane at the edge of the cylinder ( $z/d = -0.5$ ) at  $x/d = 1.5$ . It can be seen from this figure that good agreement between the experimental and the numerical data is achieved in all the comparisons shown here. Some deviation between numerical and experimental data can be seen on the  $z/d = -0.5$  plane in [figures 4.8\(k,l\)](#). Considering the higher uncertainty in the data near the edge of the cylinder due to significant transverse oscillations it can be concluded that a reasonable match is achieved, and the resolution of the grid and the accuracy of the numerical algorithm are sufficient to reasonably predict the flow characteristics around the solid and foam-covered cylinders. Further, [figure 4.8](#) is used to have a preliminary idea on the wake characteristics of the solid and foam-coved cylinder. The streamwise velocity close to the cylinder ( $x/d = 0.75$ ) ([figure 4.8a](#)) is higher in the wake of foam-covered cylinder due to flow through the foam, but it gradually decreases and becomes less than that in solid cylinder in further downstream ( $x/d = 2.5$ ) ([figure 4.8e](#)). The Reynolds stresses at  $x/d = 0.75$  are higher for the solid cylinder than that in the foam-covered cylinder except for  $\overline{u'^2}/U_o^2$  very close to the bottom wall ( $y/h \leq 0.15$ ) and near the free-edge of the cylinder ( $y/h \approx 1$ ). Since the streamwise Reynolds stress of foam-covered cylinder is higher only at these two specific locations, it can be correlated to the effect of the top and the bottom plate of the foam-covered cylinder which can produce higher turbulence due to flow through the porous media but acts as a single unit in case of the solid cylinder. At  $x/d = 2.5$  on the central plane ([figures 4.8f-h](#)), the Reynolds stresses are found to be higher for the solid cylinder up to the mid-height of the cylinder ( $y/h \leq 0.5$ ), whereas it is higher for the foam-covered cylinder above this depth ( $y/h > 0.5$ ). This demonstrates the variation in the vertical thickness of the wake region of two cylinders. [Figures 4.8\(i-l\)](#) presents similar distributions on the  $z/d = 0.5$  plane at an intermediate streamwise position ( $x/d = 1.5$ ). The time-averaged velocity and the Reynolds normal stresses for the solid cylinder are higher throughout the height of the cylinder ( $y/h \leq 1$ ) when compared to that in case of the foam-covered cylinder. This shows a much lower stress generation along the edge of the foam-covered cylinder due to break up of the large vortical structures by the

interference of the foam structures. However, the Reynolds shear stress for the foam-covered cylinder is lower than that in the solid cylinder at  $y/h \leq 0.75$  and slightly higher at  $0.75 \leq y/h \leq 1$ .

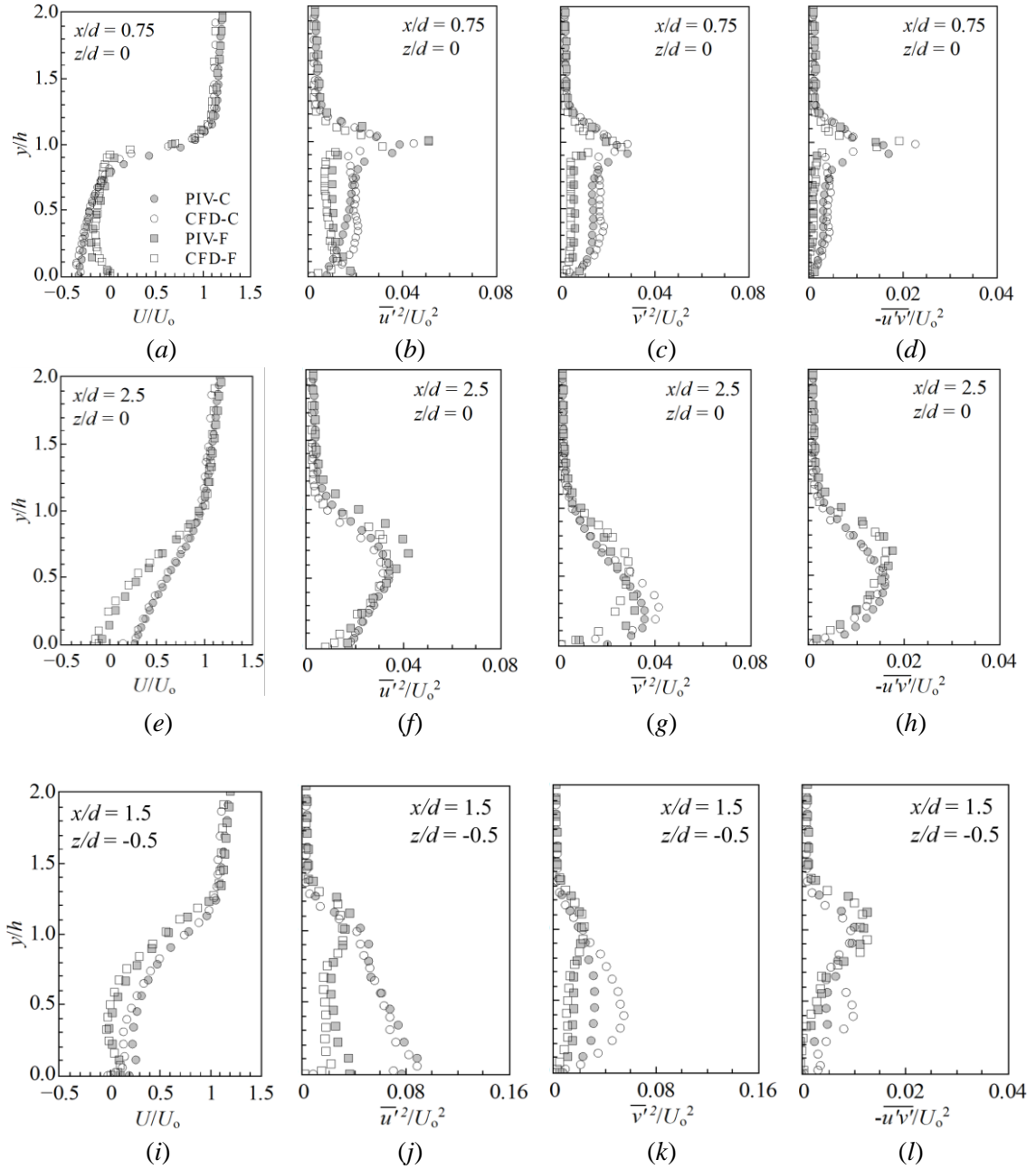


Figure 4.8. Comparison of experimental and numerical data for wall-normal distribution of dimensionless time-averaged streamwise velocity ( $U/U_0$ ) and Reynolds stresses ( $\overline{u'^2}/U_0^2$ ,  $\overline{v'^2}/U_0^2$ ,  $-\overline{u'v'}/U_0^2$ ) at (a-d)  $x/d = 0.75, z/d = 0$ ; (e-h)  $x/d = 2.5, z/d = 0$ ; and (i-l)  $x/d = 1.5, z/d = -0.5$ .

The current computational data are also validated against the previous literature (figure 4.9) in terms of coefficient of pressure ( $C_P$ ) and drag ( $C_D$ ).  $C_P$  and  $C_D$  are calculated as:  $C_P = (P$

$P_\infty)/(0.5\rho U_{0.5h}^2)$  and  $C_D = F_d/(0.5\rho U_{0.5h}^2 hd)$  where  $P$  is the static pressure at the point where pressure coefficient is calculated (i.e. at  $y/h = 0.5$  in this case),  $P_\infty$  is reference static pressure in the free stream,  $\rho$  is the density of the water and  $U_{0.5h}$  is the mean approach flow velocity at elevation  $y/h = 0.5$ . It is worth noting that the values of  $C_P$  in case of the foam-covered cylinder is estimated by using an imaginary cylinder of diameter  $d$  since no continuous surface is available. The magnitude of  $C_P$  corresponding to each azimuthal angle ( $\theta_s$ ) between  $0^\circ$  and  $360^\circ$  is presented in figure 4.9(a) for both cylinders and compared with the previous studies of Kawamura *et al.* (1984), Okamoto and Sunabashiri (1992), Pattenden *et al.* (2005), Iungo *et al.* (2012) and Zhang *et al.* (2021). These studies were carried out for Reynolds number ranging from 13 000 – 60 000 for a wide range of aspect ratios. Only the results corresponding to a similar aspect ratio as in the current study ( $h/d = 0.9$ ) are presented in figure 4.9. The magnitude of  $C_P$  in case of the foam-covered cylinder is found to be higher than that in the solid cylinder since the flow is allowed to pass through the foam structure. The distribution of  $C_P$  is not symmetric due to asymmetry in the foam structures. Figure 4.9(b) represents the average magnitude of the coefficient of drag which is found to be 0.57 and 0.72 for the solid and foam-covered cylinders, respectively. The value of  $C_D$  is much higher for the foam cylinder since the total surface area over which the drag force is calculated in this case is much higher than that in the solid cylinder, but the normalization is done by overall cross-sectional area ( $h \times d$ ) in both cases. The average values of  $C_D$  corresponding to a range of cylinder aspect ratio ( $1 \leq h/d \leq 10$ ) are presented in the figure 4.9(b) along with the data of Taniguchi *et al.* (1981), Kawamura *et al.* (1984), Okamoto and Sunabashiri (1992), Sumner *et al.* (2004), Cengel and Cimabala (2009) and Wang *et al.* (2011). A dashed line is provided to show the trend of the datasets found in the literature and an extrapolated value of  $C_D$  corresponding to  $h/d = 0.9$  provides a reasonable match with the present value of 0.57 in case of the solid cylinder. Comparison of the magnitudes of  $C_P$  and  $C_D$  for the solid cylinder and the previous literature shows good agreement which validates and reconfirms the accuracy of the current simulation.

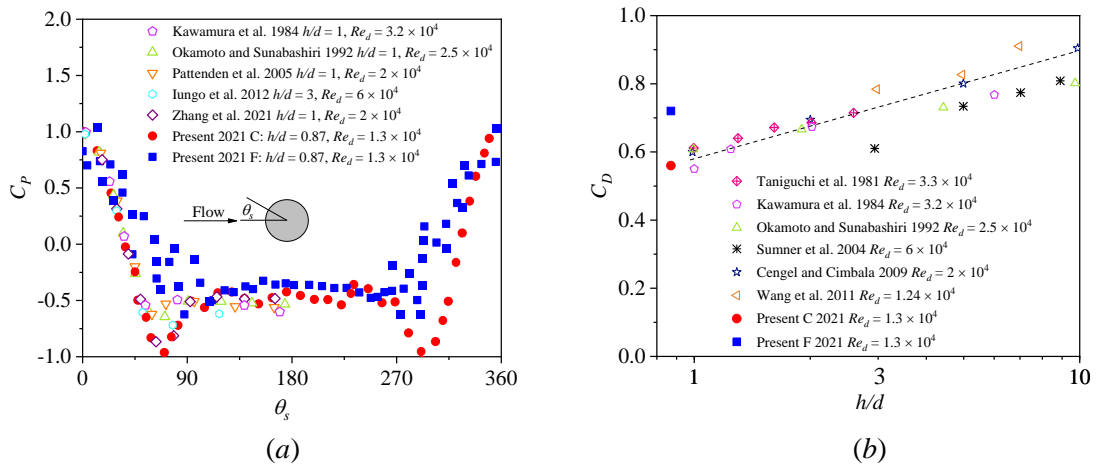


Figure 4.9. (a) The distribution of coefficient of pressure ( $C_P$ ) at the mid-height of the cylinder ( $y/h = 0.5$ ) plotted against the azimuthal angle, (b) mean value of coefficient of drag ( $C_D$ ) plotted against the cylinder aspect ratio.

#### 4.4. Flow structures around the cylinder

In figure 4.10, the coherent structures around the cylinders are depicted by the  $\lambda_2$  criteria (Jeong and Hussain 1995, Zhou *et al.* 1999) which extracts the vortical structures identifying the regions for which the largest eigenvalue of the tensor  $S_{ik}S_{kj} + \Omega_{ik}\Omega_{kj}$  is negative, where  $S_{ij} = 0.5(\partial U_i/\partial x_j + \partial U_j/\partial x_i)$  and  $\Omega_{ij} = 0.5(\partial U_i/\partial x_j - \partial U_j/\partial x_i)$  are the symmetric and anti-symmetric parts of the velocity gradient tensor. The iso-surface is generated based on a constant value of  $\lambda_2 h^2/U_o^2 = -20$  and coloured by the magnitude of the normalized velocity vector  $U_{mag}/U_o$ , where  $U_{mag} = (U^2 + V^2)^{1/2}$ . Based on the flow structures presented in Lee and Wang (1987), Krajnović (2011) and Essel *et al.* (2021), different vortical structures are identified in the figures. In case of flow around the solid cylinder, a strong horseshoe vortex (denoted by 1 in figure 4.10) can be seen

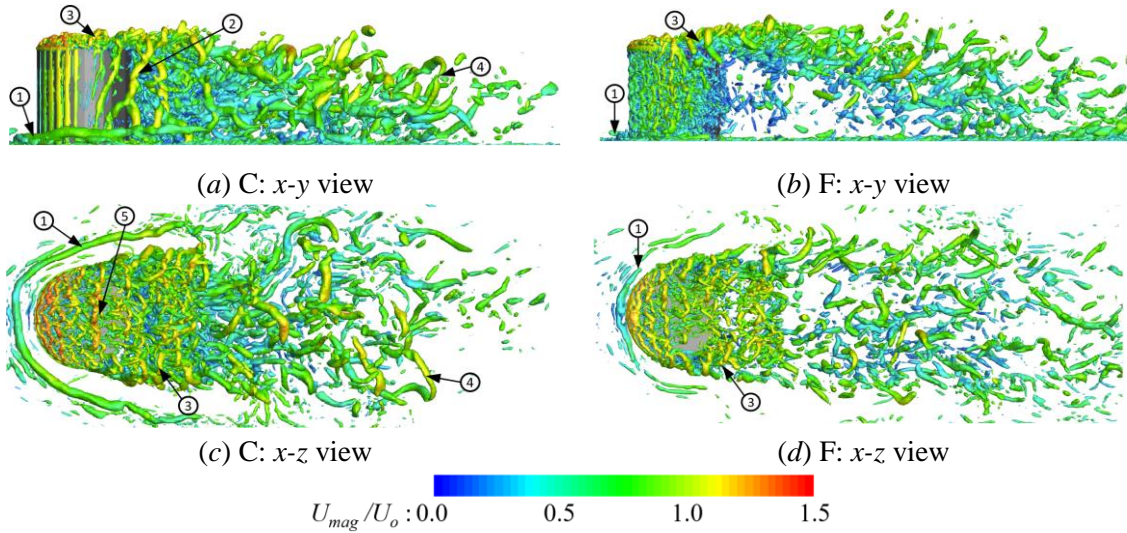


Figure 4.10. Visualization of coherent flow structures in an instantaneous flow field by using iso-surfaces of  $\lambda_2 h^2/U_o^2 = -20$  representing coherent structures around the (a,c) solid cylinder and (b,d) foam-covered cylinder, coloured by magnitude of instantaneous velocity. The vortical structures can be referred as, 1: horseshoe vortex, 2: arch vortex, 3: tip vortex, 4: trailing vortex, 5: free end arch vortex.

around the upstream edge of the cylinder and arch vortices (denoted by 2 in figure 4.10a) can be found immediate downstream of the cylinder. The tip vortices (denoted by 3 in figure 4.10) from the downstream edge of the top of the cylinder, trailing vortices (denoted by 4 in figures 4.10a,c) farther downstream and free-end arch vortex (denoted by 5 in figure 4.10c) on the top of the cylinder can also be seen. However, the presence of foam tends to disrupt the formation of these vortical structures and hence they are either broken or not very prominent in case of the foam cylinder, as seen in figures 4.10(b,d). Figure 4.10(b) shows the absence of any significant large-scale structure in the vicinity of the foam structure except close to the top plate. This variation in flow structures significantly alters the flow characteristics downstream of the cylinder which can be employed advantageously in many industrial applications related to insulating or transferring and dissipating thermal energy. These differences in flow characteristics between the two types of cylinder is discussed in the following sections.

## 4.5. Wake characteristics

The three-dimensional reverse flow region in the wake of the solid and foam-covered cylinders is presented in figure 4.11 to provide a comparative analysis of the length and width of the wake region. The reverse flow region is defined in previous literatures (Fang and Tachie 2019, Essel *et al.* 2020, Essel *et al.* 2021) as the region where the streamwise velocity component is negative and this region is depicted by the volume inside the  $U = 0$  iso-surface of the mean streamwise velocity. The downstream extent of the reverse flow region in the wake of the solid cylinder (figure 4.11a) is much smaller than that in the foam-covered cylinder (figure 4.11b) which illustrates that the wake of the solid cylinder is shorter than the foam-covered cylinder wake. The flow coming from the top of the foam-covered cylinder is carried farther downstream by the flow coming through the foam since the effective cross-sectional area of obstruction is less than that in the solid cylinder, thus creating a longer reattachment length in case of the foam-covered cylinder. It is also worth mentioning that the iso-surface in figure 4.11(b) shows a smooth transition from the top plate of the foam-covered cylinder towards the downstream flow, whereas in figure 4.11(a), it drops down immediately after the downstream-edge of the top face of the solid cylinder and then continue developing in the wake. This is because the inner solid cylinder of the foam-covered cylinder creates a wake region within the foam structures since its diameter is approximately half of the outer diameter and the top plate acts like a hanging free edge over the foam-covered cylinder. The width of the wake in the immediate downstream of the foam-covered cylinder is of the order of the inner cylinder diameter which is lesser in magnitude than the width of the solid cylinder near-wake region. The effect of these differences in the flow characteristics can also be seen in the reattachment line on the top of the cylinders, which is a straight line for the solid cylinder but curved in case of the foam-covered cylinder (shown by red line in figure 4.11). The details of the wake characteristics of the solid and foam-covered cylinders are discussed further in the following sections using the contours of mean streamwise velocity and Reynolds stresses and the distributions of velocity deficit presented at different vertical, horizontal and cross-stream planes.

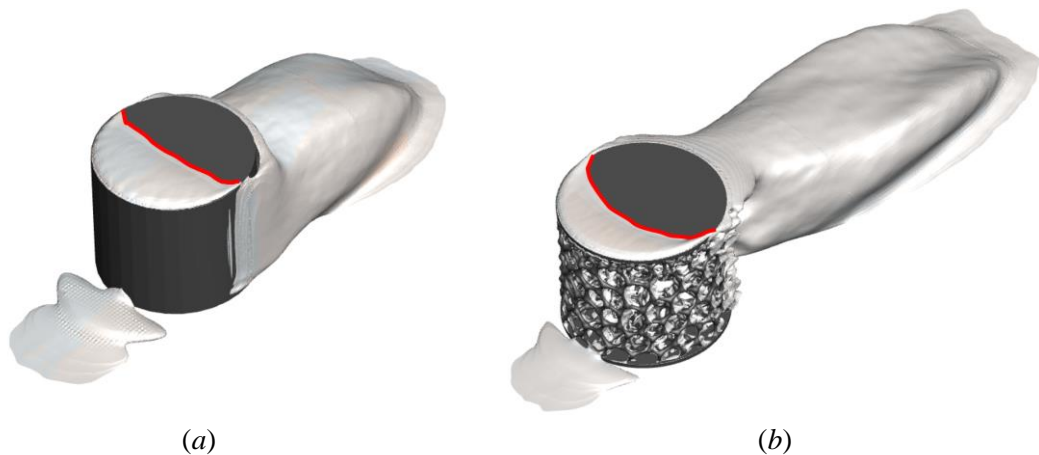


Figure 4.11.  $U/U_o = 0$  iso-surface of the time-averaged streamwise velocity, illustrating the reverse flow region in the wake of the (a) solid and (b) foam-covered cylinder.

#### 4.5.1. Vertical planes

Figure 4.12 presents the contours of the time-averaged streamwise velocity component ( $U/U_o$ ) superimposed by the streamtraces on the central vertical plane ( $z/d = 0$ ) and the vertical plane at the edge of the cylinder ( $z/d = -0.5$ ). The region of negative streamwise velocity is shown by the area within the  $U/U_o = 0$  contour line (blue line in figure 4.12) and this area of reverse flow region helps to visualize salient features of the wake characteristics of the two cylinders. On the central plane (figures 4.12a,b), the region of reverse flow is much larger in the foam-covered case and the length of reattachment on the back of the cylinder is approximately  $3d$  from the centre of the cylinder. For the solid cylinder, this reattachment length is  $2d$ , similar to that reported by Cunningham *et al.* (2013) and Essel *et al.* (2021). This indicates that the wake region for the foam-covered cylinder is much longer than that of the solid cylinder due to the flow coming through the foam structure. Similar to what is seen in figure 4.11, the zero mean streamwise velocity contour line (figure 4.12a) for the foam-covered cylinder is attached to the top plate due to the presence of the foam structure surrounding the inner solid cylinder. A difference in the reattachment length on top of the cylinder can also be seen in figures 4.12(a,b). This reattachment length is approximately  $0.5d$  and  $0.3d$  in case of the solid and foam-covered cylinders, respectively (see section 4.5.2 for further discussion). In the plane at the outer edge ( $z/d = -0.5$ ) of the cylinders (figures 4.12c,d), a reverse flow region is attached to the cylinder in the case of the solid cylinder. However, for the foam-covered cylinder, the contour line of  $U/U_o = 0$  is broken and restricted into some isolated areas due to discontinuity in the surface of the foam geometry. For flow around the foam-covered cylinder, a zone of negative streamwise velocity can be seen in this plane ( $z/d = -0.5$ ) in the downstream ( $1.4 \leq x/d \leq 2.3$ ) detached from the cylinder, showing that the reverse flow region of the foam-covered cylinder is wider in the downstream than near the cylinder.

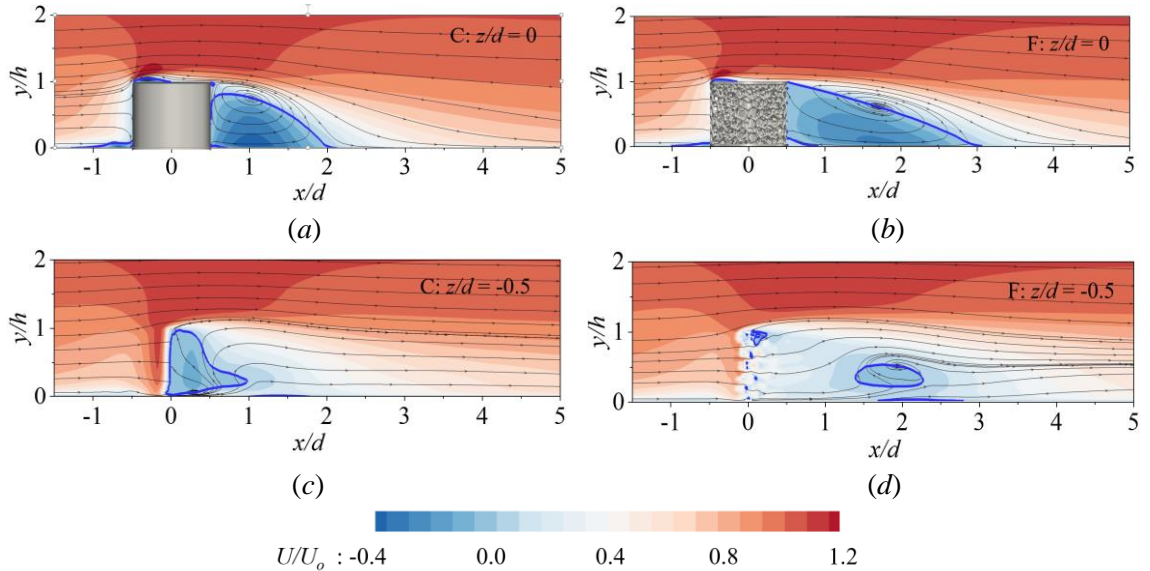


Figure 4.12. Contours of time-averaged streamwise velocity ( $U/U_o$ ) and streamlines on two representative  $x$ - $y$  planes ( $z/d = 0$  and  $-0.5$ ) for (a,c) solid cylinder, (b,d) foam-covered cylinder. The blue contour line represents the zero mean streamwise velocity ( $U/U_o = 0$ ).

The contours of the streamwise component of Reynolds normal stress are presented in figures 4.13(a,b) on the central vertical plane of the cylinder. The maximum normal stress can be found mostly along the edge of the reverse flow region (i.e.,  $U/U_o = 0$  contour line) in both cases. A comparison between the contours corresponding to the solid and foam-covered cylinders demonstrates that the streamwise normal stress is higher in magnitude in the near-wake region ( $x/d \leq 1.5$ ) of the solid cylinder and much lower for the foam-covered cylinder. This suggests that a foam covering can be used as a protective cover, shielding the cylinder from the oscillation of the vortex shedding by breaking up the large-scale flow structures. For similar reasons, a foam-covering can also be useful in reducing downstream scour around a bridge pier or other similar hydraulic structures. In this context, it is worth mentioning that the circular red patch (shown by 1 in figure 4.13(a) at the upstream of the solid cylinder indicates higher stress generation due to the horseshoe vortex, which is not prominent in case of the foam-covered cylinder (figure 4.13b). The horseshoe vortex is responsible for developing a scour hole at the upstream face of bridge piers (Roulund *et al.* 2005, Dey and Raikar 2007), which can be prevented by using a foam covering as well. Figures 4.13(c,d) presents the contours of  $\overline{u'^2}/U_o^2$  on the vertical plane at  $z/d = -0.5$  for both solid and foam-covered cylinders. Compared to the wake of the foam-covered cylinder, the streamwise normal stress in this plane is much higher in the near-wake region of the solid cylinder ( $0.5 \leq x/d \leq 3$ ). On this plane, the near-wake region of the solid cylinder undergoes high velocity gradients due to shear layers and flow oscillations caused by the vortex shedding. On the other hand, the formation of large vortical structures is disrupted in presence of the foam structures (figure 4.10) and the effect of the shear layers generated from each of the struts of the foam are not very significant in terms of overall stress generation. The other stress components on these vertical planes exhibit similar flow attributes around the solid and foam-covered cylinders and therefore are not presented here for brevity.

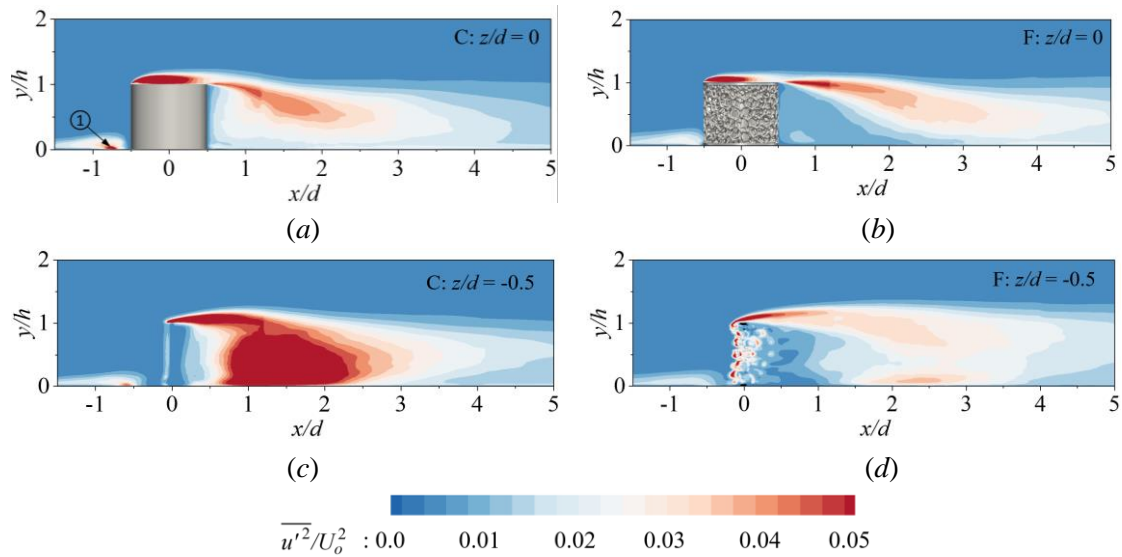


Figure 4.13. Contours of streamwise component of Reynolds normal stress ( $\overline{u'^2}/U_o^2$ ) at two representative  $x$ - $y$  planes ( $z/d = 0$  and  $-0.5$ ) for (a,c) solid cylinder, (b,d) foam-covered cylinder. The horseshoe vortex is shown by '1'.

In order to provide a quantitative comparison of the strength of the wake and variation in total stress generation between the solid and foam-covered cylinders, a volume integral of the turbulent kinetic energy is carried out over the three-dimensional reverse flow region (figure 4.11) using the formulation,

$$k_{\text{RF}} = \frac{\iiint (\overline{u'^2} + \overline{v'^2} + \overline{w'^2}) dx dy dz}{\iiint dx dy dz} \quad (4.7)$$

The total value of non-dimensional turbulent kinetic energy within the reverse flow region ( $k_{\text{RF}}/U_o^2$ ) is estimated as 0.049 and 0.029 for the solid and foam-covered cylinders, respectively, which reconfirms that the stress generation in the wake of the solid cylinder is much higher than that in the foam-covered cylinder.

#### 4.5.2. Horizontal planes

The contours of mean streamwise velocity are presented in figure 4.14 on two horizontal planes, one at the cylinder mid-height and one slightly above the top of the cylinder. Figure 4.14(a) shows that the time-averaged flow around the solid cylinder is symmetric on the mid-horizontal plane ( $y/h = 0.5$ ) and the angle of flow separation ( $\bar{\theta}_s$ ) occurs approximately at  $90^\circ$  on both sides of the cylinder. In the case of the foam-covered cylinder (figure 4.14b), the contours of mean velocity are not symmetric due to asymmetry in the foam structure. Defining an angle of separation is not straight-forward in this case due to discontinuity in the surface of the foam. If the intersection of the  $U/U_o = 0$  iso-line and the outer perimeter can be considered as an indicator of the point of separation, the separation appears to occur at a very high obtuse angle which is different on each side of the foam-covered cylinder. The width of the reverse flow region immediately downstream of the foam-covered cylinder is of the order of the inner cylinder diameter and, as seen in figure 4.14b, is narrower than that behind the solid cylinder. Similar wake characteristics can be seen in the flow visualizations from the experimental study of Yuan *et al.* (2016) on the flow around a finite cylinder with porous coating. Figure 4.14 also illustrates that the reverse flow region of the foam-covered cylinder grows larger in the downstream and becomes wider and longer than that of the solid cylinder. The contours of mean streamwise velocity immediately above the cylinder ( $y/h = 1.01$ ) are presented in figures 4.14(c,d). Interestingly, the mean flow on this plane is symmetric for both cylinders since the flow properties at this elevation are dominated by the presence of the top plate and not the foam structures. However, a variation between solid and foam-covered cylinders is noticed in the reattachment line on top of the cylinder which is a straight line (figure 4.14c) for the solid cylinder whereas it is a curved line (figure 4.14d) for the foam-covered cylinder. This curvature is caused by the flow around the inner solid cylinder which passes through the foam structure. The reattachment length for the solid cylinder is approximately  $0.5d$  which can be validated by extrapolating the experimental data of Tsutsui and Kawahara (2006) corresponding to a cylinder aspect ratio of 0.9. However, the reattachment length on the top face of the foam-covered cylinder is  $0.4d$  at the central plane ( $z/d = 0$ ) but approximately  $0.75d$  near the edges of the cylinder (at  $z/d = 0.5$  or  $-0.5$ ).



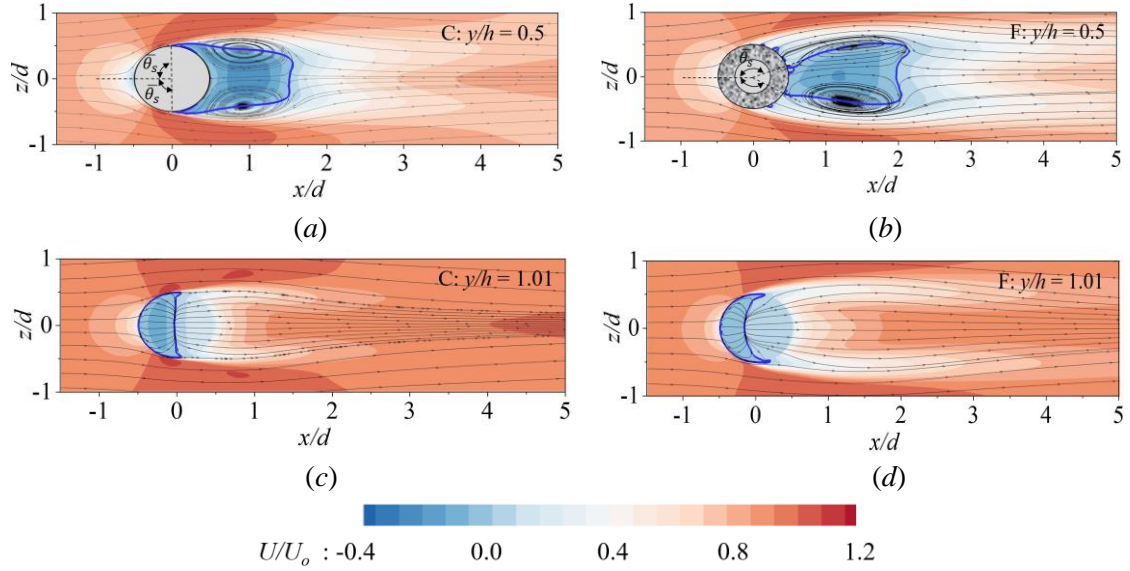


Figure 4.14. Contours of time-averaged streamwise velocity ( $U/U_o$ ) superimposed by the streamlines at two representative  $x$ - $z$  planes ( $y/h = 0.5$  and  $1.01$ ) for (a,c) solid cylinder, (b,d) foam-covered cylinder. The area inside the blue contour line ( $U/U_o = 0$ ) represents the reverse flow region.

#### 4.5.3. Cross-stream planes

A comparison of the flow features on three representative cross-stream planes ( $x/d = 0.75, 1.5$  and  $2.5$ ) are presented in figure 4.15 in order to demonstrate the flow development in the wake of

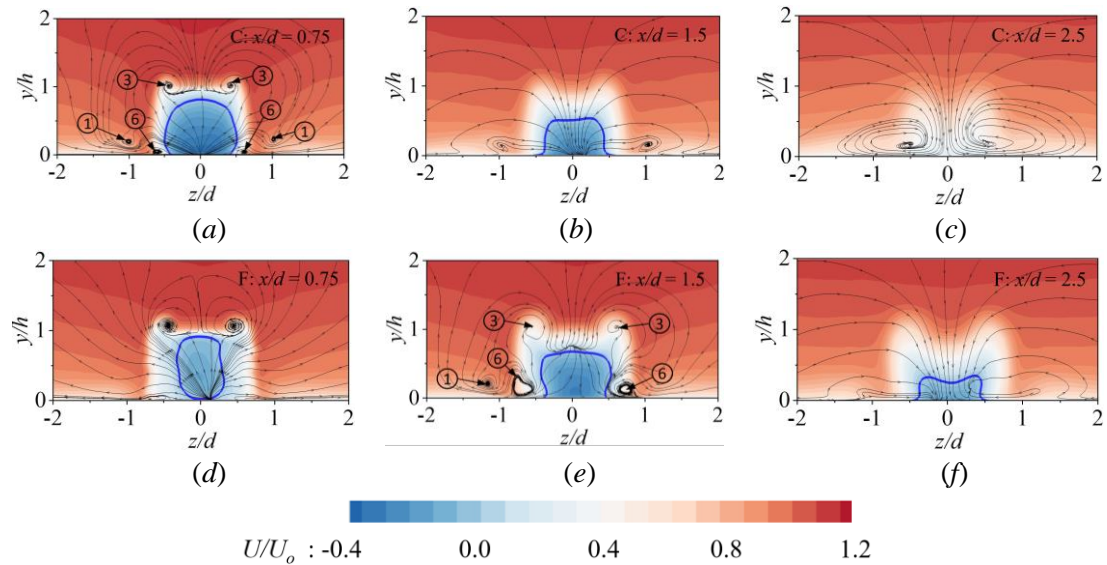


Figure 4.15. Contours of time-averaged streamwise velocity ( $U/U_o$ ) superimposed by the streamlines at three representative  $z$ - $y$  planes ( $x/d = 0.75, 1.5$  and  $2.5$ ) for (a,b,c) solid cylinder, (d,e,f) foam-covered cylinder. The area inside the blue contour line ( $U/U_o = 0$ ) represents the reverse flow region. The vortical structures are identified as; 1: horseshoe vortex, 3: tip vortex, 6: base vortex.

the solid and foam-covered cylinders. The streamtraces are plotted using the cross-stream and bed-normal component of the mean streamwise velocity which are useful in depicting the coherent flow structures around the cylinder, such as the horseshoe vortex, tip vortex and base vortex (shown by 1,3 and 6, respectively in figure 4.15). Close to the cylinder ( $x/d = 0.75$ ), the reverse flow region of the solid cylinder (figure 4.15a) is wide, whereas it is narrower and elongated in the bed-normal direction in case of the foam-covered cylinder (figure 4.15d). However, the shape of the reverse flow regions (figure 4.15b,e) on the cross-stream plane of both cylinders is nearly the same at  $x/d = 1.5$ . Farther downstream ( $x/d = 2.5$ ), the reverse flow region is still present for the foam-covered cylinder (figure 4.15f), but not in case of the solid cylinder (figure 4.15c). It is to be noticed here that the similarity between the streamline pattern and the presence of coherent flow structures can be seen between figures 4.15(a,e), and also between figures 4.15(b,f), which suggests that the addition of the foam covering elongates the downstream wake length but maintains the flow properties of a solid cylinder wake.

#### 4.5.4. Velocity deficit

The streamwise extent of the wake can be quantified using the distributions of streamwise velocity deficit which are presented on the central vertical plane ( $z/d = 0$ ) at different bed-normal locations  $0.05 \leq y/h \leq 1$  in figure 4.16(a,b). The velocity deficit ( $U_{def}$ ) is calculated as  $(U_{inlet} - U)/U_o$  where  $U_{inlet}$  is the time-averaged inflow velocity corresponding to the specific bed-normal position. At any given  $y/h$ , the magnitude of  $U_{def}$  first increases in the near-wake region and then gradually decreases to zero farther downstream. It can be seen from the distribution of  $U_{def}$  at each bed-normal position that the length of the wake or the flow recovery length (i.e., the length after which the approach flow velocity is recovered) is shorter for the solid cylinder (figure 4.16a) compared to that of the foam-covered cylinder (figure 4.16b). Zong and Nepf (2012) quantified the streamwise extent of the wake ( $L$ ) to be a combination of two length scales  $L_1$  and  $L_2$ . The magnitude of  $L_1$  can be estimated based on the streamwise position of the maximum velocity deficit and the wake region within  $L_1$  is referred to as the “steady-wake”. On the other hand, the flow recovery length  $L_2$  is calculated here as the length where 80% of velocity is recovered i.e., the streamwise velocity deficit  $U_{def} = 0.2$ . A similar value of velocity deficit was used by Nicolai *et al.* (2020) to determine total length of the wake region. Nicolai *et al.* (2020) showed that the magnitude of these length scales varies with the porosity of the cylinder. These parameters are used here to quantify and compare the length of the wake region of the solid and foam-covered cylinders. The longitudinal positions corresponding to the maximum deficits and  $U_{def} = 0.2$  are shown by ‘+’ and ‘+’, respectively in figure 4.16(a,b), and  $L_1$  and  $L_2$  are shown for one representative bed-normal position at  $y/h = 0.05$  (figure 4.16a). The wall-normal variation of these two length scales is presented in figure 4.16(c). The distribution of  $L_1/d$  is compared with the data of Nicolai *et al.* (2020) which was obtained for the wake of a solid cylinder of aspect ratio 1. These two distributions show a good match which further validates the present numerical simulation. The value of  $L_1/d$  decreases with the increase in  $y/h$  for both solid and foam-covered cylinders, whereas the value of  $L_2/d$  initially increases at  $y/h \leq 0.2$  and then decreases with an increase in  $y/h$ . Figure 4.16(a,b) demonstrates that both  $L_1$  and  $L_2$  are higher in magnitude for the foam-covered cylinder than for the solid cylinder.

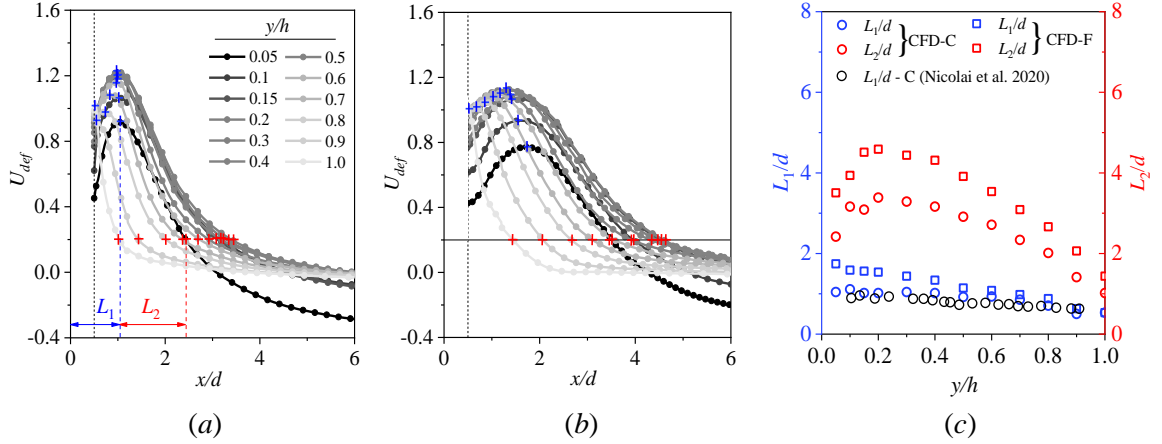


Figure 4.16. Streamwise velocity deficit ( $U_{def}$ ) on central vertical plane ( $z/d = 0$ ) at different bed-normal positions for (a) solid cylinder, and (b) foam-covered cylinder. The blue ‘+’ sign indicates the maximum velocity deficit and the red ‘+’ sign corresponds to  $U_{def} = 0.2$ . (c) comparison of dimensionless length scales of the wake ( $L_1/d$  and  $L_2/d$ ) for solid and foam-covered cylinder plotted against the data of Nicolai *et al.* (2020) for solid cylinder with aspect ratio 1.

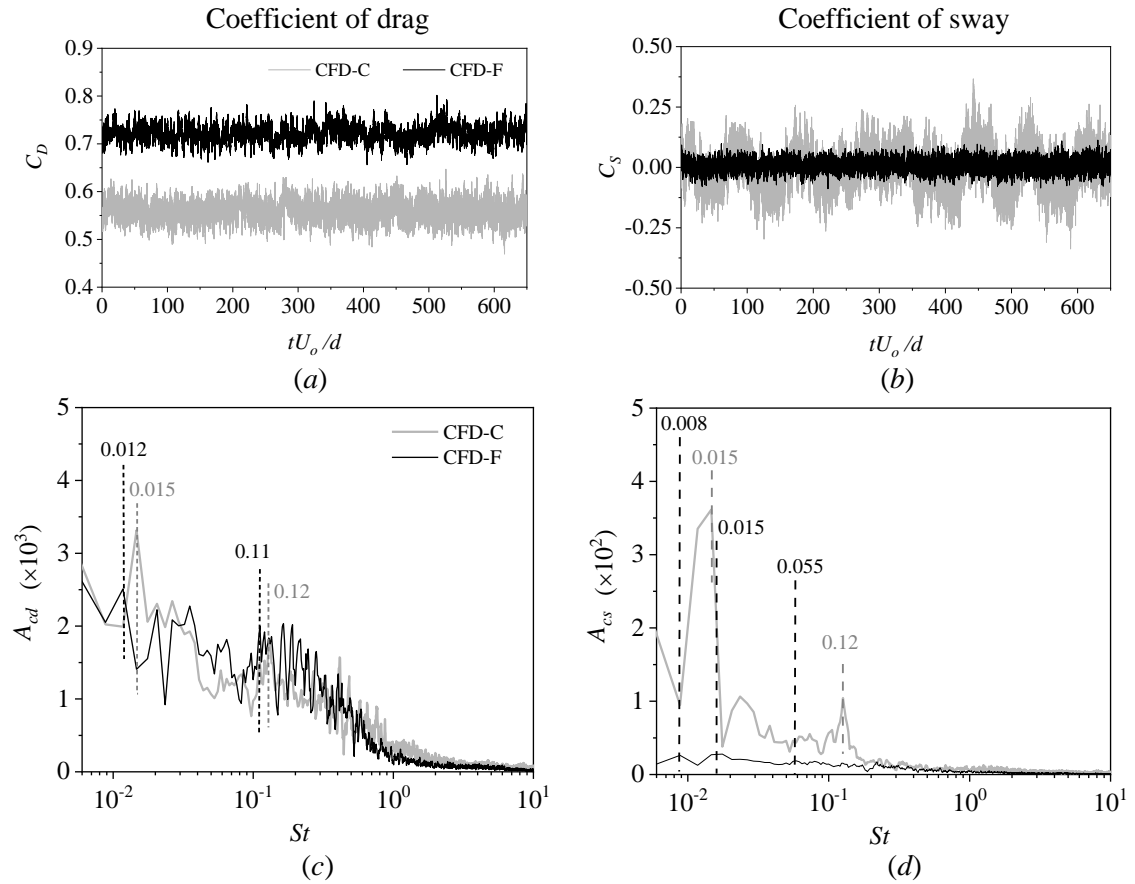


Figure 4.17. Temporal history of the coefficient and energy spectra of (a,c) drag ( $C_D$ ), and (b,d) sway ( $C_S$ ). The dominant frequencies are shown by the dashed lines.

## 4.6. Frequency analysis

The oscillating characteristic of the wake is captured by a frequency analysis of the time-series data of the average total force on the cylinder in the streamwise ( $x$ ) and transverse ( $z$ ) flow directions, respectively, expressed as the drag ( $C_D$ ) and sway ( $C_S$ ) coefficients. The distributions of  $C_D$  and  $C_S$  are plotted against the non-dimension time ( $tU_o/d$ ) in [figure 4.17\(a,b\)](#). As depicted in [figure 4.17\(a\)](#), the foam-covered cylinder has a higher time-averaged drag coefficient of 0.72 compared to a value of 0.57 for the solid cylinder. Interestingly, the form drag coefficients for the solid and foam-covered cylinder are estimated as 0.55 and 0.62, respectively. A similar result can be found in the study of Taddei *et al.* (2016) on an array of circular cylinders, where the value of  $C_D$  is found to be increasing with the decrease in cylinder porosity and then suddenly decreases for the solid cylinder. On the other hand, the skin-friction drag coefficient for the foam-covered cylinder is found to be 0.1, which is higher than the value of 0.02 for the solid cylinder. This is likely since the total frictional force is proportional to the effective surface area. The coefficient of sway plotted in [figure 4.17b](#) illustrates that the velocity oscillations have higher magnitude in case of the solid cylinder, which is due to the formation of large-scale vortical structures being interrupted by the foam covering.

The Fast Fourier Transformation (FFT) of the time-series data of  $C_D$  and  $C_S$  ([figure 4.17c,d](#)) reveals the dominant frequencies of the quasi-periodic fluctuations of the flow. In case of the solid cylinder, two distinct peaks can be identified at Strouhal numbers ( $St = fL/U_o$ ) of 0.015 and 0.12. Porteous *et al.* (2014) and Moreau and Doolan (2013) have mentioned the existence of more than one peak in their FFT analyses. In the study of Porteous *et al.* (2014) (cylinder aspect ratio,  $h/d = 22.7$ ), the Strouhal numbers corresponding to the dominant frequencies are reported as 0.07 and 0.17. However, researchers are yet to reach an agreement to identify one of them to be the dominant and the other one to be the subdominant frequency. For example, in the studies of Sakamoto and Arie (1983) ( $1.5 \leq h/d \leq 8$ ) and Sumner *et al.* (2004) ( $5 \leq h/d \leq 9$ ), the frequency corresponding to the higher magnitude of  $St$  is reported as the dominant frequency, which is 0.14 and 0.16, respectively. On the other hand, Hain *et al.* (2008) and Essel *et al.* (2021) have reported a dominant frequency corresponding to  $St = 0.014$  and 0.015 for aspect ratios 2.1 and 1.8, respectively. Therefore, these two frequencies are described in the present study as lower and higher dominant frequencies. However, it is difficult to point out any specific dominant frequency in case of the foam-covered cylinder since no significant peak with greater relative height with respect to the surrounding peaks can be found. Therefore, FFT is also carried out for the temporal data of different velocity components at multiple points in the flow field. The peaks corresponding to foam-covered cylinder data are determined by identifying the peaks which are found several times in the FFT diagrams of these points and presented in [figure 4.17\(c,d\)](#). The value of  $St$  corresponding to these peak frequencies vary between 0.008 to 0.11.

A further investigation on the dominant frequencies is carried out by conducting the FFT analysis of instantaneous streamwise velocity data at each point along representative horizontal and vertical lines located at  $x/d = 1.5$ , which lies near the foci of the recirculation region. The contour diagram in [figure 4.18\(a,b\)](#) shows the FFT along a transverse line ( $-1.5 \leq z/d \leq 1.5$ ) at mid-cylinder depth ( $y/h = 0.5$ ) whereas [figure 4.18\(c,d\)](#) represents the contour of FFTs along a vertical line ( $0 \leq y/h \leq 1.5$ ) at central horizontal plane ( $z/d = 0$ ). The contour plots are coloured by the amplitude of fluctuations normalized by the corresponding maximum values so that it can vary between 0 and 1

in each case. The black line corresponding to the red patches help to identify the peak frequencies corresponding to different spatial coordinates. Similar to the figure 4.17, the two peak frequencies (corresponding to  $St = 0.015$  and  $0.12$ ) can be distinctly identified for the solid cylinder in the contour diagram of figures 4.18(a,c). In case of foam-covered cylinder (figure 4.18b,d), multiple frequencies are identified as potential dominant or subdominant frequencies. However, these patches of peak frequencies correspond to the specific flow regions and not present consistently over the span of the width or height of the cylinder. For example, in figure 4.18(b), the value of  $St$  corresponding to lower dominant frequencies are identified as  $0.008$  at  $z/d = 0.48$ , whereas it is  $0.015$  at  $z/d = -0.45$  and the red patches with higher amplitude can be seen locally near the edges of the cylinder. Therefore, the dominant frequencies are not same for both side of the foam-covered cylinder and figure 4.18(b) shows this asymmetric distribution at lower frequencies due to the asymmetry in the foam structure. On the other hand, lower dominant frequencies for the vertical

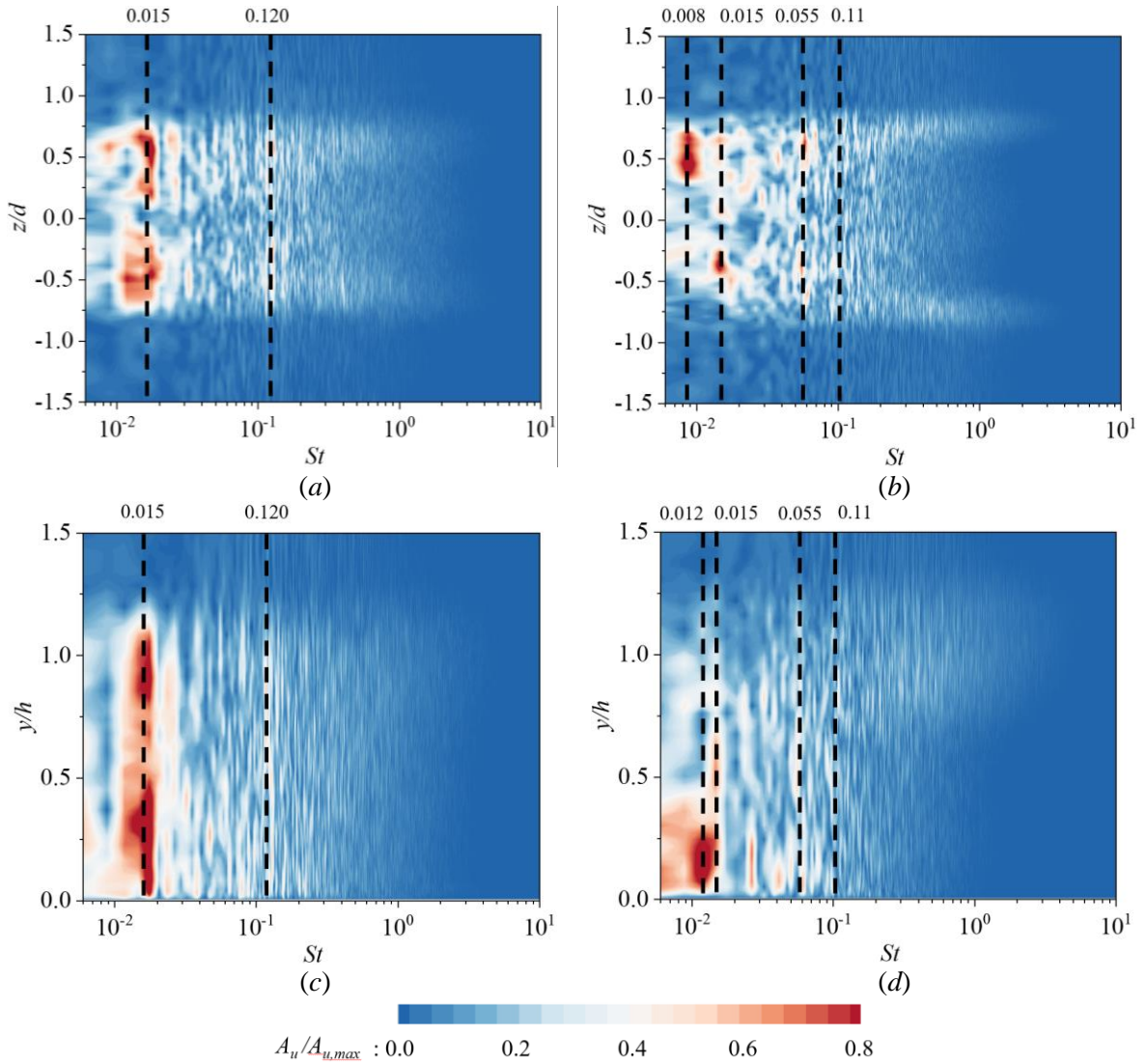


Figure 4.18. Contour of the energy spectra along a transverse line ( $-1.5 \leq z/d \leq 1.5$ ) at mid-cylinder depth ( $y/h = 0.5$ ) and a vertical line ( $0 \leq y/h \leq 1.5$ ) at central horizontal plane ( $z/d = 0$ ) for (a,c) solid cylinder, and (b,d) foam-covered cylinder. Both lines are located at  $x/d = 1.5$ .

line (figure 4.18d) can be correlated to the Strouhal number of 0.012 and 0.015. Apart from that, another two higher dominant frequencies can be identified at  $St = 0.055$  and  $0.11$  from the contour plots of the foam-covered cylinder (figure 4.18b,d). However, the relative magnitude corresponding to these two frequencies are not significantly higher than the surrounding points which demonstrates that the existence of von-Karman vortex shedding is not very prominent in case of foam-covered cylinder. The present analysis shows that multiple local periodic flow structures can be present in case of foam-covered cylinder which correspond to different dominant frequencies. The flow in the vicinity of the foam-covered cylinder can be very complex due to asymmetric geometry and can be guided by several factors such as the foam structures, inner solid cylinder and the top plate which can be responsible for these multiple dominating frequencies restricted to specific locations.

#### 4.7. Spectral proper orthogonal decomposition

Identification of energetic flow structures is an essential part of any fluid mechanics studies and it has been commonly done by using energy-ranked proper orthogonal decomposition (POD) or frequency-ranked dynamic mode decomposition (DMD). However, these methods are not ideal when the flow characteristics are induced to multiple dominant frequencies similar to the present study. Therefore, a spectral POD (SPOD) algorithm, as proposed by Towne *et al.* (2018) and Schmidt and Colonius (2020), is used to study the coherent structures at different frequencies. Similar to the standard POD method, the SPOD also finds an optimal orthogonal basis for which a set of eigenfunctions (modes) can capture higher energy than any other orthogonal basis. In the case of SPOD, these modes vary both in space and time to depict spatio-temporal coherence in the flow structures.

The SPOD algorithm is provided as a MATLAB code by Towne *et al.* (2018) and available at [https://github.com/SpectralPOD/spod\\_matlab](https://github.com/SpectralPOD/spod_matlab). This code is used here with finer adjustments of the spectral parameters. The LES data is stored at a frequency of 1000Hz for  $650U_o/d$  non-dimensional time which corresponds to nearly 120000 snapshots. Ideally, the best outcome can be obtained by keeping the value of both  $N_b$  and  $N_t$  as high as possible, where  $N_b$  is the number of blocks and  $N_t$  is the number of snapshots in each block. A higher value of  $N_b$  can provide a sufficient number of realizations for SPOD, whereas a lower resolvable frequency can be achieved with a higher value of  $N_t$ . A compromise between the two is necessary for a given data sampling rate and number of snapshots. Therefore, the whole data is optimally divided into sets  $2^{12}$  snapshots (i.e.,  $N_t = 2^{12}$ ) and the number of blocks  $N_b$  is 30. The resulting frequency resolution of the SPOD spectrum is 0.24Hz (corresponding  $St = 0.047$ ) considering the Nyquist sampling theory. However, SPOD is also carried out using other combinations of the values of  $N_b$  and  $N_t$ , and similar results are achieved corresponding to the specific frequencies and modes. While conducting the SPOD analysis, a 50% overlapping of the window is also considered since it yields the best results by reducing the variance of the spectral densities (Welch 1967). The spectral leakage is reduced by using a Hamming window function:

$$w_j = 0.54 - 0.46 \cos\left[\frac{2j\pi}{N_t}\right] \text{ for } j = 1 \text{ to } N_t. \quad (4.8)$$

#### 4.7.1. SPOD on vertical plane

The significant energy containing flow structures are depicted on central vertical plane ( $z/d = 0$ ) using SPOD. Figure 4.19 shows SPOD energy spectra of the first 10 modes for both solid (figure 4.19a) and foam-covered cylinders (figure 4.19b). The first two modes carry 24% and 13.5% of total energy in case of solid cylinder and 22.5% and 13.2% for the foam-covered cylinder, which are significantly higher than the other modes. Compared to the solid cylinder, the order of magnitude of the energy containment corresponding to each mode is found to be lower for the foam-covered cylinder. For brevity, the flow structures are presented for three frequencies ( $St = 0.14, 0.33, 0.56$ ) (shown by dashed line in figure 4.19) which are optimally chosen based on the

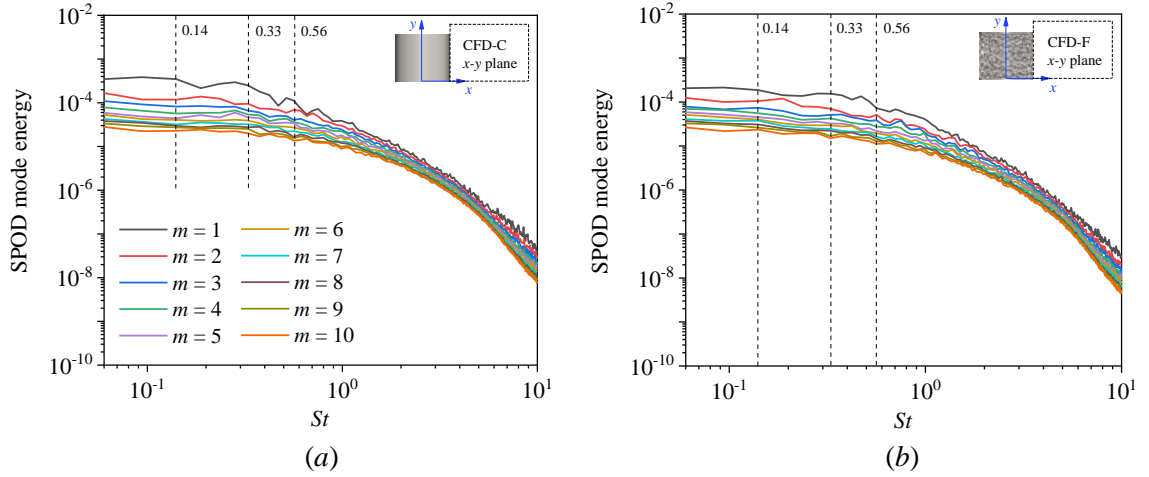


Figure 4.19. SPOD mode energy spectra on central vertical plane ( $z/d = 0$ ) for (a) solid cylinder and (b) foam-covered cylinder.

peaks in the energy spectra. It is worth noting here that a small variation in the frequency does not significantly alter the characteristics of the SPOD modes. Therefore, these three frequencies can be used to depict the flow characteristics although they may not correspond to the actual peak amplitude in each case.

The first two SPOD modes ( $m = 1, 2$ ) on the central vertical plane are presented at  $St = 0.14, 0.33, 0.56$  for the solid (figures 4.20a-f) and foam-covered cylinders (figures 4.20g-l). Large-scale vortical structures can be identified at  $St = 0.14$  downstream of the cylinders, which can be correlated with the von Karman type primary vortex formation. In case of the solid cylinder (figures 4.20a,d), these flow structures are nearly attached to the cylinder, whereas no large-scale flow structure can be found in the near-wake region of the foam-covered cylinder in the first mode (figure 4.20g). At  $St = 0.33$  and  $0.56$ , the flow structures in the wake of the solid cylinders gradually get elongated and slightly rotated in the clockwise direction (figures 4.20b,c,e,f) which may be due to the Kelvin-Helmholtz type instability resulting from the interaction between the flow within the recirculation region and the outer flow. The upper and lower portions of the vortices experience a lag in the velocity due to the relative velocity of the corresponding flow region. The vortical structures generated from the downstream edge of the top face of the cylinder can be found at higher  $St$ . For the solid cylinder (figures 4.20c,e), these vortical structures are pressed downward by the flow on the top of the cylinder and get attached to the bed at a streamwise position of  $x/d = 2$ . On the contrary, these vortices of the foam-covered cylinder (figures 4.20h,i,k,l) are lifted upward due

to the flow coming through the foam structures and reattaches to the bed at much farther downstream position compared to the solid cylinder, which is consistent with the longer wake region of the foam-covered cylinder. A comparison between the flow structures of the second mode in figures 4.20(k,l) demonstrates the instability of the tip vortices and a transition to the formation of larger downstream vortical structures.

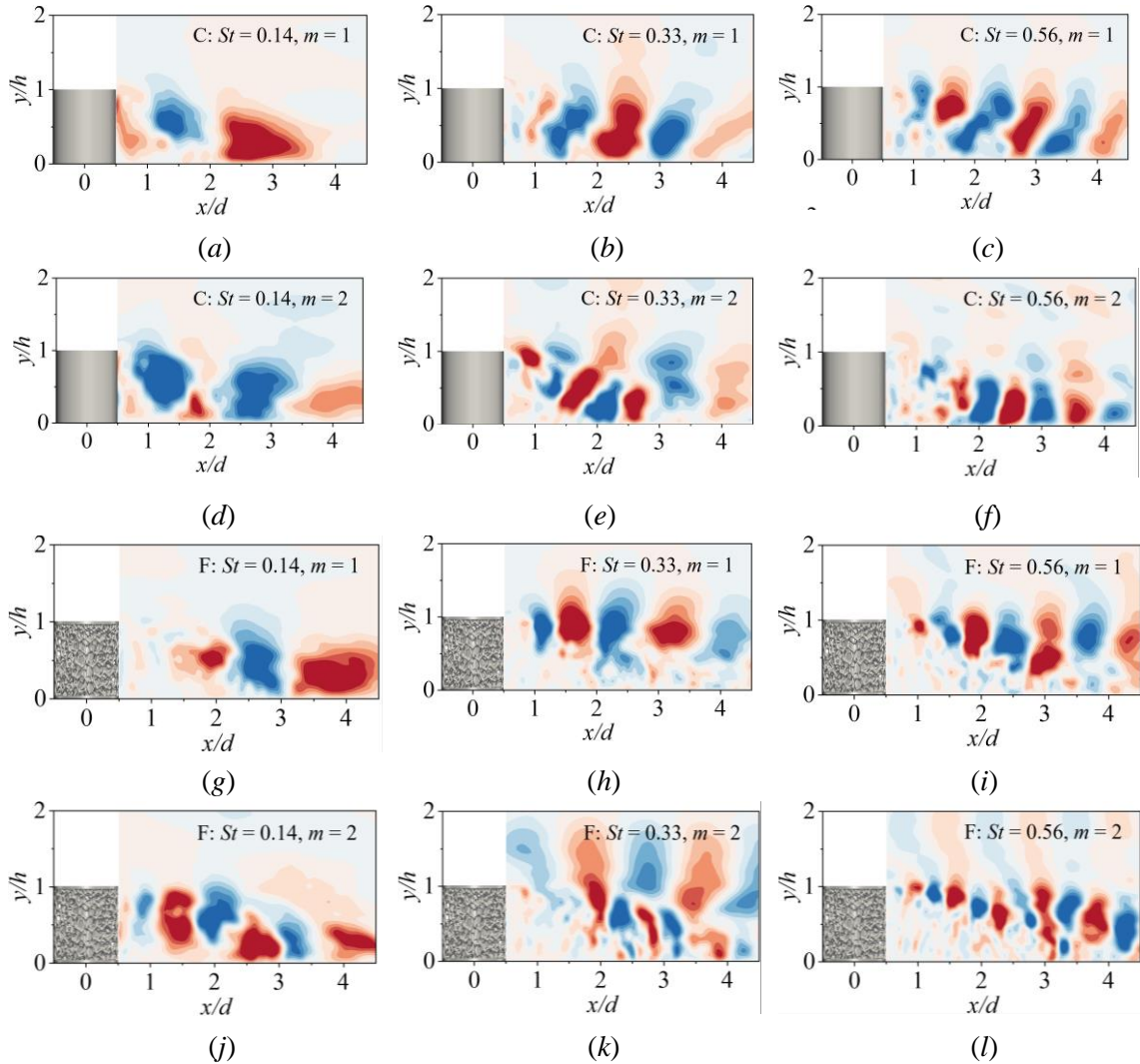


Figure 4.20. First two SPOD modes at  $St = 0.14, 0.33, 0.56$  for (a-f) solid cylinder, (g-l) foam-covered cylinder.

#### 4.7.2. SPOD on horizontal plane

Figure 4.21 presents the SPOD mode energy spectra on the mid-horizontal plane ( $y/h = 0$ ). A larger difference in energy retainment can be found between the solid (figure 4.21a) and foam-covered cylinder (figure 4.21b) on this plane. The first two modes for the solid cylinder contain 24.3% and 11.8% of total energy, whereas the first two modes of the foam-covered cylinder contain 20% and 12.5% of energy, respectively. It is worth noticing that the difference between percentage energy consumption of the first two modes (on this plane) is much less in case of the foam-covered cylinder which illustrates a higher relative energy contribution from the small-scale structures



compared to the solid cylinder. Similar to the vertical plane, the SPOD modes are presented for  $St = 0.14, 0.33, 0.56$  and shown by vertical dashed lines in [Figure 4.21](#).

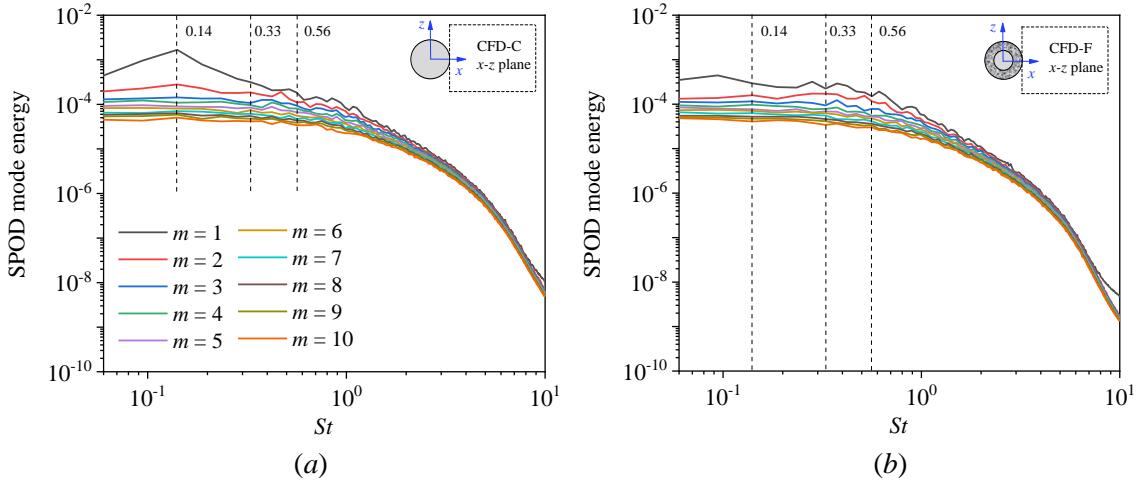
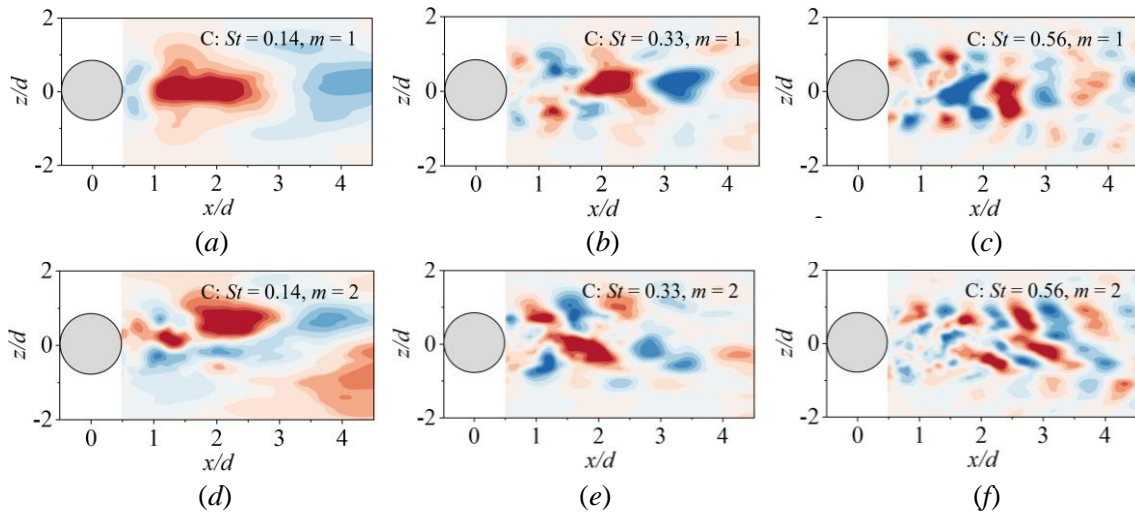


Figure 4.21. SPOD mode energy spectra on mid-horizontal plane ( $y/h = 0$ ) for (a) solid cylinder, and (b) foam-covered cylinder.

The SPOD modes on the mid-horizontal plane ( $y/h = 0$ ) are presented in [figure 4.22](#) for the first two highest energy containing modes corresponding to  $St = 0.14, 0.33, 0.56$ . The first mode of the solid cylinder at  $St = 0.14$  ([figure 4.22a](#)) shows the formation of the von Karman type vortical structures, whereas the large-scale structures can only be seen ([figure 4.22g](#)) far downstream ( $x/d > 2$ ) of the foam-covered cylinder. However, the vortex formations at this frequency are symmetric in both cases. The structures in the second mode ([figures 4.22d,j](#)) are not well-structured compared to the first mode due to significant difference in energy consumption. At higher Strouhal numbers ( $St = 0.33$  and  $0.56$ ), the wake of the solid cylinder ([figures 4.22b,c,e,f](#)) shows a transition from the von Karman vortex street to the formation of side vortices, mostly retaining the symmetry in vortex generation. Interestingly, the SPOD modes of the foam-covered cylinder ([figures 4.22h,k](#)) at  $St = 0.33$  reveals asymmetry between the modes. A relatively large one-sided vortical formation can be found at the alternating position in either mode. A similar asymmetry can be seen in the formation of side vortices at  $St = 0.56$  ([figures 4.22i,l](#)).



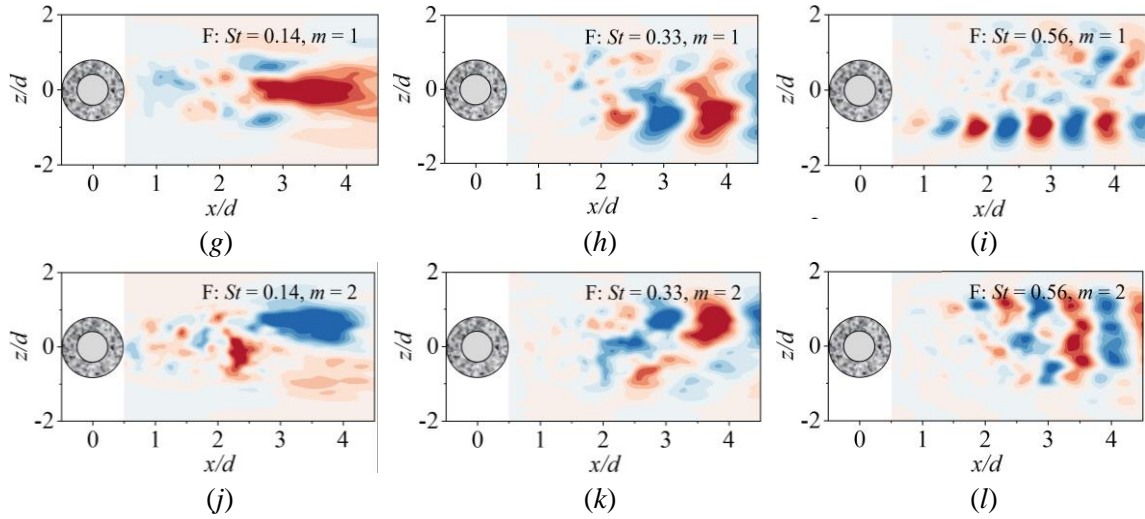


Figure 4.22. First two SPOD modes at  $St = 0.14, 0.33, 0.56$  for (a-f) solid cylinders, and (g-l) foam-covered cylinder.

#### 4.8. Summary and conclusions

The present experimental and computational study provides a comparison of wake characteristics between surface mounted, fully submerged solid and foam-covered cylinders. The foam-covered cylinder consists of an inner solid cylinder and a foam wrapping enclosed by a top and a base plate, with the whole structure dimensionally identical with the solid cylinder. The wake behind both cylinders is developed under a fully developed approach flow, which is experimentally achieved by adequate tripping and computationally accomplished by recycling of the flow variables from outlet to inlet. For initial understanding of the wake characteristics, instantaneous coherent flow structures are depicted using  $\lambda_2$  criteria. A strong horseshoe vortex, arch vortex and tip vortices can be found in the vicinity of the solid cylinder. However, formation of these large-scale flow structures is interrupted by the foam geometry and broken coherent structures are identified in the case of the foam-covered cylinder. A three-dimensional iso-surface of zero streamwise velocity demonstrates that the reverse flow region of the foam-covered cylinder is narrow in the immediate downstream and its width is of the order of the inner cylinder diameter. This reverse flow region grows in the downstream and becomes wider than the solid cylinder wake. The length of the reverse flow region is also found to be greater in case of the foam-covered cylinder. The contours of Reynolds stress on two vertical planes, one at the centre and the other at the edge of the cylinder demonstrate a lower stress generation in the near-wake region of the foam-covered cylinder compared to the solid cylinder. A difference in the flow characteristics of these two types of cylinders can also be seen in the flow reattachment on top of the cylinder. The reattachment occurs along a straight line for the solid cylinder, whereas it is a curved line for the foam-covered cylinder. The temporal variation of drag and sway coefficients are also recorded for both the solid and foam-covered cylinders. Interestingly, a higher coefficient of drag is observed in case of the foam-covered cylinder. The fluctuation of sway coefficient for the foam-cylinder is found to be significantly smaller than that of the solid cylinder which reveals the damping of the primary vortex shedding in presence of the foam. The FFT analyses of these two coefficients show two significant peak amplitude for the solid cylinder, whereas no dominant frequency can be prominently

identified for the foam-covered cylinder. Finally, SPOD is carried out on the mid-vertical and horizontal planes of the cylinders. No large-scale vortical structures are found in the vicinity of the foam-covered cylinder wake, whereas existence of large vortices can be noticed farther downstream. The tip vortices of the foam-covered cylinder are lifted upward by the flow coming through the foam which indirectly helps in generating the longer wake region compared to the solid cylinder. An asymmetry in vortex generation is also noticed in the wake of the foam-covered cylinder. The flow around the foam-covered cylinder creates many interesting alterations of the flow characteristics compared to the solid cylinder wake. The complex wake characteristics of the foam-covered cylinder are largely guided by the porosity of the foam, presence of the inner cylinder and the effect of the top plate. These guiding factors can be manipulated efficiently to create improved passive wake control and enhance its potential in environmental and industrial implications.

## References

- Abishek, S., King, A. J. C., Mead-Hunter, R., Golkarfard, V., Heikamp, W. & Mullins, B. J. 2017 Generation and validation of virtual nonwoven, foam and knitted filter (separator/coalescer) geometries for CFD simulations. *Sep. Purif.* **188**, 493-507.
- Abishek, S., King, A. J. C., Schuler, J., Kasper, G., Schmid, H. J. & Mullins, B. J. 2018 Representative domain size for the simulation of coalescence filtration in nonwoven and foam media. *Sep. Purif.* **207**, 344-352.
- Abdi, I. A., Khashehchi, M. & Modirshanechi, M. 2014 A Comparative analysis on the velocity profile and vortex shedding of heated foamed cylinders. *19<sup>th</sup> Australasian Fluid Mechanics Conference*, December 8-11, Australasian Fluid Mechanics Society, Australia.
- Abdi, I. A., Khashehchi, M. & Hooman, K. 2017. Investigation of coherence behind a single foamed tube. *Fluid Mech. Res. Int. J.*, **1** (2), 45-54.
- Balachandar, R. & Patel, V. C. 2005 Velocity measurements in a developed open channel flow in the presence of an upstream perturbation. *J. Hydraul. Eng.* **43** (3), 258–266.
- Bhattacharyya, S. & Singh, A. K. 2011 Reduction in drag and vortex shedding frequency through porous sheath around a circular cylinder. *Int. J. Numer. Methods Fluids*, **65** (6), 683-698.
- Bhattacharyya, S., Dhinakaran, S. & Khalili, A. 2006. Fluid motion around and through a porous cylinder. *Chem. Eng. Sci.* **61** (13), 4451-4461.
- Bruneau, C. H. & Mortazavi, I. 2006 Control of vortex shedding around a pipe section using a porous sheath. *Int. J. Offshore Polar.* **16** (02).
- Celik, I. B., Cehreli, Z. N. & Yavuz, I. 2005 Index of resolution quality for large eddy simulations. *J. Fluids Eng.* **127** (5), 949–958.
- Celik, I., Klein, M. & Janicka, J. 2009 Assessment measures for engineering LES applications. *J. Fluids Eng.* **131** (3), 031102.
- Cengel, Y. & Cimbala, J. 2009 *Fluid Mechanics: Fundamentals and Applications* (2nd edition). McGraw-Hill Higher Education, Boston.
- Chang, W.Y., Constantinescu, G. & Tsai, W. F. 2017 On the flow and coherent structures generated by a circular array of rigid emerged cylinders placed in an open channel with flat and deformed bed. *J. Fluid Mech.* **831**, 1–40.
- Clauser, F. H. 1956 The turbulent boundary layer. *Adv. Appl. Mech.* (Eds., H.L. Dryden and T. von Karman) **4**, 1-51.

- Clift, R., Grace, J. R. & Weber, M. E. 1978 *Bubbles, Drops, and Particles*. Academic Press, New York, US.
- Cunningham, P., Linn, R. R., Koo, E. & Wilson, C. J. 2013 Large-eddy simulations of air flow and turbulence within and around low-aspect-ratio cylindrical open-top chambers. *J. Appl. Meteorol. Clim.* **52** (8), 1716-1737.
- Das, S., Balachandar, R. & Barron, R. M. 2021 Analysis of fully developed state in open channel flow using uniform momentum zones. *J. Fluid Mech.* (under review).
- Das, S., Balachandar, R. & Barron, R. M. 2021 Effect of free surface perturbation on the characteristics of fully developed smooth open channel flow. *J. Hydraul. Res.* (under review).
- Dey, S. & Raikar, R. V. 2007. Characteristics of horseshoe vortex in developing scour holes at piers. *J. Hydraul Eng.* **133** (4), 399-413.
- Essel, E. E., Tachie, M. F. & Balachandar, R. 2021 Time-resolved wake dynamics of finite wall-mounted circular cylinders submerged in a turbulent boundary layer. *J. Fluid Mech.* **917**, A8.
- Essel, E., Das, S. & Balachandar, R. 2020 Effects of rear angle on the turbulent wake flow between two in-line Ahmed bodies. *Atmosphere*, **11** (4), 328.
- Fang, X. & Tachie, M. F. 2019 On the unsteady characteristics of turbulent separations over a forward-backward-facing step. *J. Fluid Mech.*, **863**, 994-1030.
- Ghisalberti, M. & Nepf, H. 2009 Shallow flows over a permeable medium: the hydrodynamics of submerged aquatic canopies. *Transport Porous Med.* **78** (2), 309-326.
- Hain, R., Kahler, C. J. & Michaelis, D. 2008 Tomographic and time resolved PIV measurements on a finite cylinder mounted on a flat plate. *Exp. Fluids.* **45** (4), 715-724.
- Hasegawa, M. & Sakaue, H. 2020 Investigation of drag reduction on a circular cylinder using microfiber coating by changing its permeability. *AIAA Scitech. 2020 Forum* (p. 0044).
- Heidari, M. 2016. Wake characteristics of single and tandem emergent cylinders in shallow open channel flow. PhD thesis, University of Windsor, Canada.
- Iungo, G. V., Pii, L. M. & Buresti, G. 2012 Experimental investigation on the aerodynamic loads and wake flow features of a low aspect-ratio circular cylinder. *J. Fluids Struct.* **28**, 279-291.
- Jeong, J. & Hussain, F. 1995. On the Identification of a Vortex. *J. Fluid Mech.* **285**, 69-94.
- Kawamura, T., Hiwada, M., Hibino, T., Mabuchi, I. & Kumada, M. 1984 Flow around a finite circular cylinder on a flat plate: Cylinder height greater than turbulent boundary layer thickness. *Bulletin of JSME*, **27** (232), 2142-2151.
- Kemp, J. L., Harper, D. M. & Crosa, G. A. 2000 The habitat-scale ecohydraulics of rivers. *Ecol. Engng.* **16** (1), 17-29.
- Kolmogorov, A. N. 1991 Dissipation of energy in the locally isotropic turbulence. *Proc. R. Soc. Lond. A* **434**, 15-17.
- Krajnović, S. 2011 Flow around a tall finite cylinder explored by large eddy simulation. *J. Fluid Mech.* **676**, 294-317.
- Kraynik, A.M., Reinelt, D.A. & van Swol, F. 2004 Structure of random foam, *Phys. Rev. Lett.* **93** (20), 208301-1-208301-4.
- Lee, L. & Wang, Y. 1987. Aerodynamics of a circular cylinder of finite length in cross flow. *Forum on Turbulent Flows*, June 14-17, Cincinnati, OH (p.61-65).

- Lilly, D.K. 1992 A proposed modification of the Germano subgrid-scale closure method. *Phys. Fluids*. **4** (3), 633-635.
- Liu, H., Wei, J. & Qu, Z. 2014. The interaction of porous material coating with the near wake of bluff body. *J. Fluids Eng.* **136** (2), 021302.
- Longmire, E. K. & Eaton, J. K. 1992 Structure of a particle-laden round jet. *J. Fluid Mech.* **236**, 217–257.
- Manceau, R. & Hanjalić, K. 2002 Elliptic blending model: A new near-wall Reynolds-stress turbulence closure. *Phys. Fluids*. **14** (2), 744–754.
- Montminy, M. D., Tannenbaum, A. R. & Macosko, C. W. 2004 The 3D structure of real polymer foams, *J. Colloid Interf. Sci.* **280**, 202–211.
- Moreau, D. & Doolan, C. J. 2013 Flow-induced sound of wall-mounted finite length cylinders. *AIAA J.* **51** (10), 2493–2502.
- Nakagawa, H. & Nezu, I. 1977 Prediction of the contributions to the Reynolds stress from bursting events in open-channel flows. *J. Fluid Mech.* **80** (1), 99–128.
- Nasif, G., Balachandar, R. & Barron, R. M. 2020 Supercritical flow characteristics in smooth open channels with different aspect ratios. *Phys. Fluids*. **32** (10), 105102.
- Nezu, I. & Rodi, W. 1986 Open channel flow measurements with a laser doppler anemometer. *J. Hydraul. Eng.* **112** (5), 335-355.
- Nicolai, C., Taddei, S., Manes, C. & Ganapathisubramani, B. 2020 Wakes of wall-bounded turbulent flows past patches of circular cylinders. *J. Fluid Mech.*, **892**, A37.
- Nikora, V., Ian, M., Stephen, M., Stephen, C., Dubravka, P. & Roy, W. 2007 Double-averaging concept for rough-bed open-channel and overland flows: Theoretical background. *J. Hydraul. Eng.* **133** (8), 873–883.
- Odabae, M., Hooman, K. & Gurgenci, H. 2011 Metal foam heat exchangers for heat transfer augmentation from a cylinder in cross-flow. *Transport Porous Med.* **86** (3), 911-923.
- Okamoto, S. & Sunabashiri, Y. 1992 Vortex shedding from a circular cylinder of finite length placed on a ground plane. *J Fluids Eng.* **114** (4), 512-521.
- Pattenden, R. J., Turnock, S. R. & Zhang, X. 2005. Measurements of the flow over a low-aspect-ratio cylinder mounted on a ground plane. *Exp. Fluids*. **39** (1), 10-21.
- Pizer, S. M., Amburn, E. P., Austin, J. D., Cromartie, R., Geselowitz, A., Greer, T., Ter Haar Romeny, B., Zimmerman, J. B. & Zuiderveld, K. 1987 Adaptive histogram equalization and its variations. *Comput. Gr. Image Process.* **39** (3), 355–368.
- Pope, S. B. 2000 *Turbulent Flows*, Cambridge University Press, Cambridge, UK.
- Porteous, R., Moreau, D. J. & Doolan, C. J. 2014 A review of flow-induced noise from finite wall-mounted cylinders. *J. Fluids Struct.* **51**, 240–254.
- Roulund, A., Sumer, B. M., Fredsøe, J. & Michelsen, J. 2005 Numerical and experimental investigation of flow and scour around a circular pile. *J. Fluid Mech.* **534**, 351-401.
- Sakamoto H & Arie M 1983. Vortex shedding from a rectangular prism and circular cylinder placed vertically in a turbulent boundary layer. *J. Fluid Mech.* **126**, 147–165.
- Sarkar, S. & Dey, S. 2010 Double-averaging turbulence characteristics in flows over a gravel bed. *J. Hydraul. Res.* **48** (6), 801–809.
- Schmidt, O. T. & Colonius, T. 2020 Guide to spectral proper orthogonal decomposition. *AIAA J.* **58** (3), 1023-1033.

- Shavit, U., Lowe, R. J. & Steinbuck, J. V. 2007 Intensity capping: a simple method to improve cross-correlation PIV results. *Exp. Fluids*. **42** (2), 225–240.
- Sueki, T., Takaishi, T., Ikeda, M. & Arai, N. 2010 Application of porous material to reduce aerodynamic sound from bluff bodies. *Fluid Dyn. Res.* **42** (1), 015004.
- Sumner, D. 2013 Flow above the free end of a surface-mounted finite-height circular cylinder: a review. *J. Fluids Struct.* **43**, 41–63.
- Sumner, D., Heseltine, J. L. & Dansereau, O. J. P. 2004 Wake structure of a finite circular cylinder of small aspect ratio. *Exp. Fluids*. **37** (5), 720–730.
- Taddei, S., Manes, C. & Ganapathisubramani, B. 2016. Characterisation of drag and wake properties of canopy patches immersed in turbulent boundary layers. *J. Fluid Mech.* **798**, 27–49.
- Taniguchi, S., Sakamoto, H. & Arie, M. 1981 Flow around a circular cylinder vertically mounted in a turbulent boundary layer. *Bulletin of JSME*, **24** (193), 1130–1136.
- Thielicke, W. & Stamhuis, E. 2014 PIVlab - towards user-friendly, affordable and accurate digital particle image velocimetry in MATLAB. *J. Open Res. Softw.* **2** (1), e30.
- Towne, A., Schmidt, O. T. & Colonius, T. 2018 Spectral proper orthogonal decomposition and its relationship to dynamic mode decomposition and resolvent analysis. *J. Fluid Mech.* **847**, 821–867.
- Tsutsui, T. & Kawahara, M. 2005 Heat transfer around a cylindrical protuberance mounted in a plane turbulent boundary layer. *J. Heat Transfer*. **128** (2): 153–161.
- Virani, N., Roussinova, V. and Balachandar, R. 2019 Resolution quality indices for Large Eddy Simulation in modelling a turbulent free jet. *4th Thermal and Fluids Engineering Conference*, April 14–17, Las Vegas, NV, USA.
- Wang, H. F., Zhou, Y. & Mi, J. 2012 Effects of aspect ratio on the drag of a wall-mounted finite-length cylinder in subcritical and critical regimes. *Exp. Fluids*. **53** (2), 423–436.
- Welch, P. 1967 The use of fast Fourier transform for the estimation of power spectra: a method based on time averaging over short, modified periodograms. *IEEE Trans. Audio Electroacoust.* **15** (2), 70–73.
- White, P. L. & van Vlack, L. H. 1970 A comparison of two- and three-dimensional size distributions in a cellular material. *Metallography*. **3** 241–258.
- Yuan, H., Xia, C., Chen, Y. & Yang, Z. 2016 Flow around a finite circular cylinder coated with porous media. *In Proceedings of the 8th International Colloquium on Bluff Body Aerodynamics and Applications*, June 7–11, Boston, Massachusetts, USA.
- Zhou, J., Adrian, R. J., Balachandar, S. & Kendall, T. M. 1999 Mechanisms for generating coherent packets of hairpin vortices in channel flow. *J. Fluid Mech.* **387**, 353–396.
- Zong, L. & Nepf, H. 2012. Vortex development behind a finite porous obstruction in a channel. *J. Fluid Mech.* **691**, 368–391.

## CHAPTER 5 CONCLUSIONS AND RECOMMENDATIONS

The present study compares the wake characteristics of a wall-mounted submerged solid cylinder and a foam-covered circular cylinder at an aspect ratio of 0.9. The wake behind the cylinder is developed under a fully developed approach flow condition which is mandatory in order to maintain consistency between the studies conducted in different laboratories and research groups. The computational method for generating fully developed flow is well-established but this is not straightforward in open channel flow experiments. Therefore, the effect of the trips and the free surface perturbations are explored using planar PIV measurements in [Chapters 2](#) and [3](#), prior to the study of the wakes. Finally, a comparison of the wake characteristics of the solid and the foam-covered cylinders are presented in [Chapter 4](#). Findings of each of these chapters is summarized here, along with the scope for future work.

In [Chapter 2](#), the effects of tripping on the downstream flow characteristics are investigated for a given inflow length. By trial-and-error, different near-bed trip arrangements were tested to arrive at a proper trip arrangement in order to achieve a fully developed flow. The test cases are named as under- or over-tripped if the corresponding tripping intensity is lower or higher than that of the fully developed state, respectively. The trip intensity in the under-tripped case is not adequate to reach a fully developed state in the test section. On the other hand, if trip intensity is very high, a longer streamwise distance is required to dissipate the additional turbulence. The fully developed profiles are consistent with the wall-normal distributions of Reynolds stress and higher-order moments, and validated against results available in literature.

On establishing a fully developed flow in the open channel, a comparison of the flow characteristics is made with that of a developing flow using uniform momentum zone (UMZ) analysis. The number of UMZs ( $N_{UMZ}$ ) at each instant is identified based on the number of peaks in the probability density function of streamwise velocity component. The conditional averaging of the velocity deficits corresponding to a given  $N_{UMZ}$  reveals the existence of large-scale Q2 events in the logarithmic layer for higher number of UMZs and large-scale Q4 events for lower number of UMZs which is similar for both fully developed and developing flow. The fully developed flow in the outer layer shows an opposite trend, i.e., large-scale Q2 events are found for lower number of UMZs, whereas large-scale Q4 events are identified for higher number of UMZs. This vertical variability in the fully developed open channel flow is reconfirmed by the conditional averaging of  $R_{Q2/Q4}$  (i.e., the ratio of shear contribution from the Q2 and Q4 events) based on the  $N_{UMZ}$ . In the outer layer, a higher shear generation from the sweeping events is noticed for the fully developed flow. Since the boundary layer thickness is close to the flow depth in the fully developed flow, no significant free stream region is present and a momentum exchange between the boundary layer and the outer flow is not possible. This causes the vertical variability and higher shear contribution from the sweeping events. These variations in the flow characteristics between a developing and a fully developed open channel flow cannot be detected in the time-averaged quantities but may affect the results of a fluid-structure interaction study since the inner flow properties of the approach flow will be different.

[Chapter 3](#) presents the effects of free surface perturbation on the flow variables at a far downstream test section. The perturbation is generated using smooth or rough light Styrofoam floater boards which are commonly used in open channel flow experiments to suppress the free

surface waves. The downstream flow characteristics with the floaters are compared to the fully developed flow experiment which is conducted without any floater. A dip in the mean streamwise velocity is observed adjacent to the free surface with the introduction of the floaters. This dip increases with the increment of level of perturbation and the Reynolds shear stress gradually becomes negative close to the free surface. A deviation from the fully developed profiles is also noticed in the distributions of skewness and flatness. The joint probability distribution of velocity fluctuations and the distribution of  $R_{Q2+Q4/Q1+Q3}$  (where  $R_{Q2+Q4/Q1+Q3}$  is the ratio of shear contribution from the combined effect of Q2+Q4 and Q1+Q3) reveal that the dominance of Q2 and Q4 events shifts to Q1 and Q3 events near the free surface, which is caused by the sweeps and ejections of the inverted shear layer generated from the bottom surface of the floaters. Although the floaters are intended to use for a reduction of the free surface perturbations, they have an adverse effect on the downstream flow characteristics. Therefore, the floaters are not used in the study of the wake.

In Chapter 4, the wake characteristics of a solid cylinder and a foam-covered cylinder are explored experimentally using planar particle image velocimetry and computationally by large eddy simulation. A fully developed approach flow is stimulated in the experimental study using the knowledge generated in Chapters 2 and 3. The foam-covered cylinder consists of an inner solid cylinder, covered by a highly porous foam structure and enclosed by a top and base plate. The outer diameter ( $d$ ) and the height of the two cylinders are identical. The length of the wake of the foam-covered cylinder is found to be higher than that of the solid cylinder which is depicted by the extent of reverse flow region and the length of flow recovery. Compared to the solid cylinder wake, the reverse flow region of the foam-covered cylinder is narrower in the near-wake region but wider in the downstream region. Another distinction between the flow around two cylinders is found in the reattachment line on the top surface of the cylinder, which is a curved line for the foam-covered cylinder but a straight line for the solid cylinder. The flow through the foam structures generates a higher drag and interrupts the formation of any large-scale periodic flow structures. The iso-surface of  $\lambda_2$  shows prominent vortical structures such as a horseshoe vortex, arch vortex, tip vortex in case of the solid cylinder, which are broken and discontinuous for the foam-covered cylinder. The sway coefficient for the solid cylinder shows a clear periodic nature which cannot be seen for the foam-covered cylinder. No significant dominant frequency is identified in the wake of the foam-covered cylinder. Also, the Reynolds stresses in the near-wake region of the foam-covered cylinder are found to be much lower than that of the solid cylinder for a similar reason. Finally, SPOD modes are used to reveal the coherent flow structures. The tip vortices for the solid cylinder move downward and become attached to the bottom wall within a length of  $2d$  whereas they are lifted upward by the flow coming through the foam structure and therefore, the reattachment length is longer for the foam-covered cylinder. In the horizontal plane, no significant vortical structures can be found in the near-wake region of the foam-covered cylinder and an asymmetric generation of side vortices is noticed.

The findings of the Chapter 4 provide an overview of the flow characteristics around foam-covered cylinders, which is mostly guided by the porosity of the foam structure, diameter of the inner cylinder and the top plate. It is possible to develop a highly effective passive flow control by varying these parameters. For example, a potential future study can be carried out by visualizing the flow fields obtained by varying the porosity and thickness of the foam-coating. This study can be useful to determine the optimum porosity and thickness for different practical applications such as in heat exchanger, scour prevention, controlling flow induced vibrations. etc. Another interesting future study would be a comparison of the wake of the foam-covered cylinder with and without the



top plate. If the top plate is removed, flow will be able to move upward through the foam structure causing vertical bleeding. Further, the wake characteristics of the foam-covered cylinder can also be investigated by varying the cylinder aspect ratio or the annular radius of the foam covering.

## APPENDICES

### Appendix A. Dependence of UMZ analysis on threshold kinetic energy deficit and streamwise extent of FOV

In this Appendix, we have explored the sensitivity and dependency of UMZ analysis on the assigned value of  $K_{th}$  and  $\mathcal{L}^+$ . With a variation in the magnitude of  $K_{th}$ , the position of the TNTI varies and a region of flow may get included or excluded in the analysis. Similarly, the number of velocity vectors in each instance varies when a different extent of FOV is chosen in the UMZ analysis. If there is a significant streamwise variation in the flow properties, the number of momentum zones corresponding to each instance may vary significantly with the change in  $\mathcal{L}^+$ . The average number of peaks ( $\bar{N}_{peaks}$ ) was estimated for a range of values of  $K_{th}$  ( $0.7 \leq K_{th} \leq 0.9$ ) and  $\mathcal{L}^+$  ( $1250 \leq \mathcal{L}^+ \leq 2250$ ) for test cases T0 and T1&T3 at  $H = 0.170$  m and no significant deviation is noticed (figure 2.18) for the current experimental data. Therefore, our current choice of  $K_{th}$  and  $\mathcal{L}^+$  can be safely used without losing generality and changing these choices will not alter the current findings.

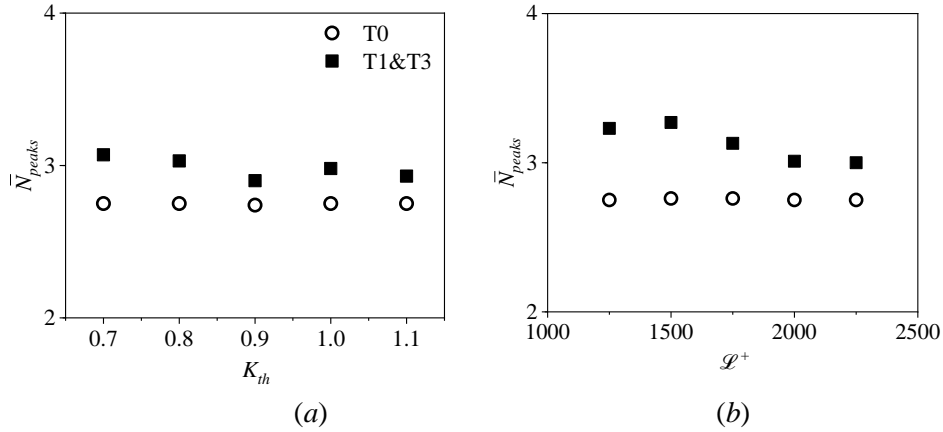


Figure A.1. Variation of  $\bar{N}_{peaks}$  with the change in (a) threshold kinetic energy deficit ( $K_{th}$ ) and (b) length of FOV ( $\mathcal{L}^+$ ).

### Appendix B. Dependence of UMZ analysis on the bin size

One of the crucial parameters in the momentum zone analysis is the bin size used to generate the PDFs of streamwise velocities. The number of modal velocities (i.e., the number of momentum zones) for a specific instance will largely depend on the bin size. Since the flow properties are analysed based on the conditional averaging of the instances corresponding to a specific value of  $N_{UMZ}$ , it is necessary to ensure that our concluding remarks do not depend on the selection of the bin size ( $0.5U_\tau$ ). Therefore, the momentum zone analysis was carried out with two alternative bin sizes: (1)  $0.25U_\tau$  and (2)  $0.75U_\tau$  to check the dependence of UMZ analysis on the bin size. The corresponding PDFs for the bin sizes of  $0.25U_\tau$  and  $0.75U_\tau$  are presented for the fully developed state and the developing flow (figure 2.19a,d) and a similar distribution is noticed in both test cases. As a representative flow variable, the bed-normal distributions of  $R_{Q2/Q4}$  is shown, which is evaluated by conditional averaging of the instances in a range of  $3 \leq N_{UMZ} \leq 7$  (figure 2.19b,c) and

$2 \leq N_{UMZ} \leq 3$  (figure 2.19e,f) for the bin sizes of  $0.25U_\tau$  and  $0.75U_\tau$ , respectively. In case of fully developed flow, the peak magnitude of  $R_{Q2/Q4}$  moves from  $y/\delta' \approx 0.6$  to  $y/\delta' \approx 0.15$  with an increment of  $N_{UMZ}$  (figure 2.19b,e). On the other hand, the peak magnitude of  $R_{Q2/Q4}$  is located near  $y/\delta' \approx 0.7$  (figure 2.19c,f) in the developing flow and does not vary with a change in the number of momentum zones. This follows a similar trend with what was seen earlier with the bin size of  $0.5U_\tau$  in section 2.6.4, proving our findings to be independent of the bin size. A variation in bin size can change the range of  $N_{UMZ}$  (or  $\bar{N}_{peaks}$ ) but the comparison between overall flow properties corresponding to higher and lower number of momentum zones will be still the same. There may be a possibility of inconsistency in some specific instances, but the impact of it can be nullified when averaging over a large number of data sets.

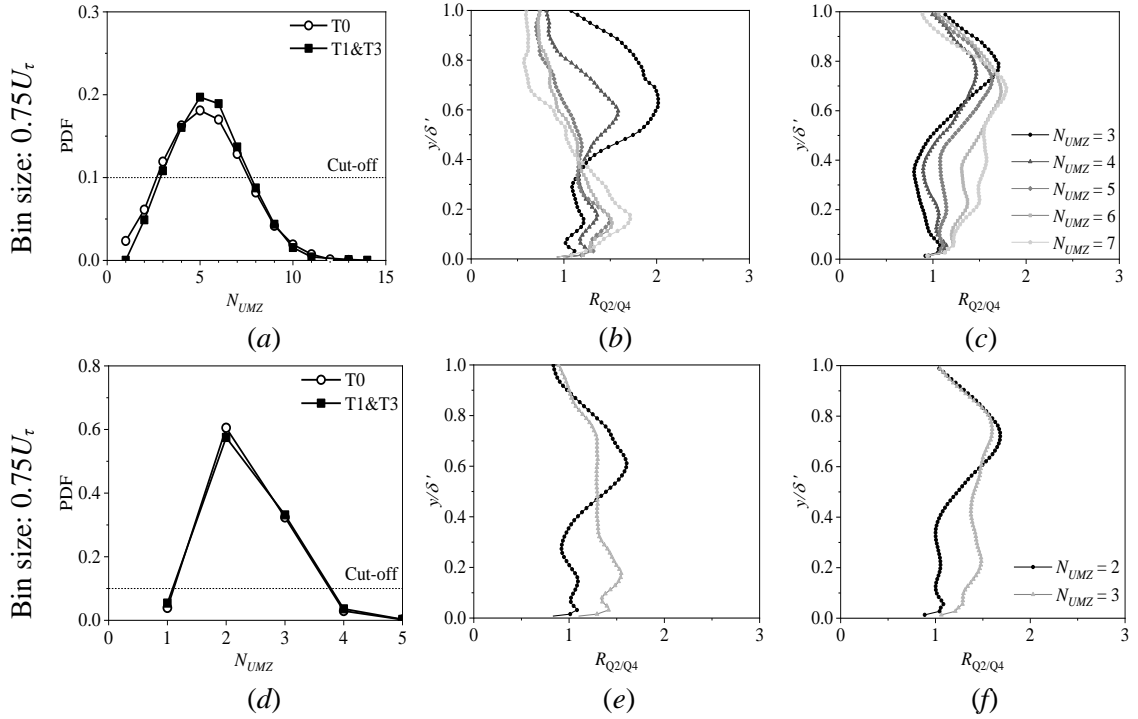


Figure A.2. PDF of  $N_{UMZ}$  corresponding to bin size (a)  $0.25U_\tau$  and (d)  $0.75U_\tau$  for the fully developed flow (T1&T3 at  $H = 0.170$  m) and the developing (T0 at  $H = 0.170$  m). Corresponding bed-normal distribution of  $R_{Q2/Q4}$  for bin size  $0.25U_\tau$  and  $0.75U_\tau$  for (b,e) the fully developed flow (T1&T3 at  $H = 0.170$  m) and (c,f) the developing (T0 at  $H = 0.170$  m).

## VITA AUCTORIS

NAME: Subhadip Das

PLACE OF BIRTH: Howrah, WB, India

YEAR OF BIRTH: 1992

EDUCATION: Jadavpur University, B.E., WB, India, 2013

IIT Kanpur, M.Tech., UP, India, 2015

ProQuest Number: 28548342

INFORMATION TO ALL USERS

The quality and completeness of this reproduction is dependent on the quality and completeness of the copy made available to ProQuest.



Distributed by ProQuest LLC (2021).

Copyright of the Dissertation is held by the Author unless otherwise noted.

This work may be used in accordance with the terms of the Creative Commons license or other rights statement, as indicated in the copyright statement or in the metadata associated with this work. Unless otherwise specified in the copyright statement or the metadata, all rights are reserved by the copyright holder.

This work is protected against unauthorized copying under Title 17, United States Code and other applicable copyright laws.

Microform Edition where available © ProQuest LLC. No reproduction or digitization of the Microform Edition is authorized without permission of ProQuest LLC.

ProQuest LLC  
789 East Eisenhower Parkway  
P.O. Box 1346  
Ann Arbor, MI 48106 - 1346 USA